Reports on Progress in Physics

PURPOSE-LED PUBLISHING™

PAPER • **OPEN ACCESS**

Exact results of the one-dimensional repulsive Hubbard model

To cite this article: Jia-Jia Luo *et al* 2024 *Rep. Prog. Phys.* **87** 117601

View the article online for updates and enhancements.

You may also like

- Emergent phases in graphene flat bands
  Saisab Bhowmik, Arindam Ghosh and U Chandni
- Molecular nanomagnets: a viable path toward quantum information processing?
  A Chiesa, P Santini, E Garlatti et al.
- Mechanical, electronic, optical, piezoelectric and ferroic properties of strained graphene and other strained monolayers and multilayers: an update
  Gerardo G Naumis, Saúl A Herrera, Shiva P Poudel et al.

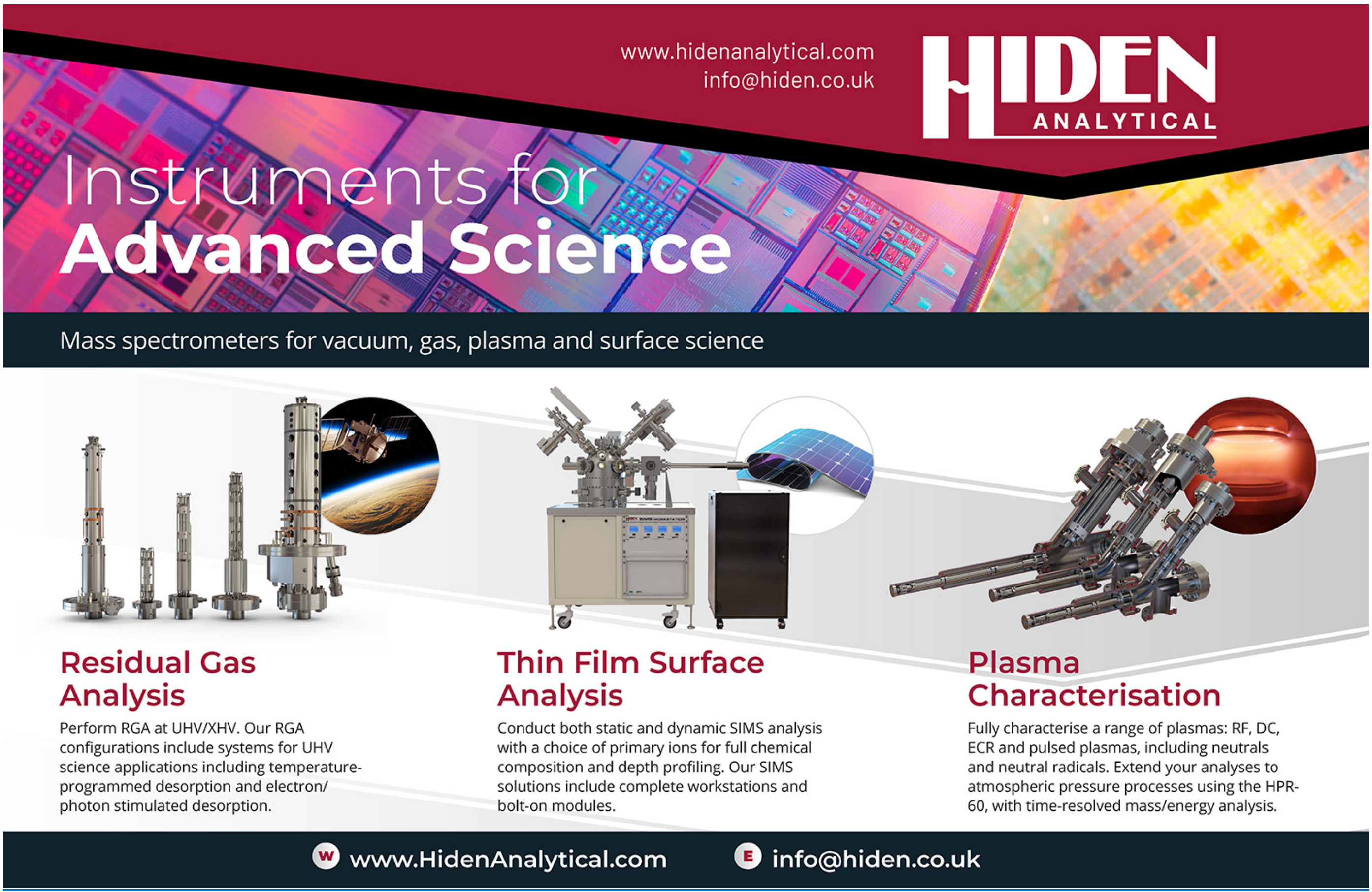

www.hidenanalytical.com
info@hiden.co.uk

HIDEN ANALYTICAL

Instruments for
Advanced Science

Mass spectrometers for vacuum, gas, plasma and surface science

Residual Gas Analysis
Perform RGA at UHV/XHV. Our RGA configurations include systems for UHV science applications including temperature-programmed desorption and electron/photon stimulated desorption.

Thin Film Surface Analysis
Conduct both static and dynamic SIMS analysis with a choice of primary ions for full chemical composition and depth profiling. Our SIMS solutions include complete workstations and bolt-on modules.

Plasma Characterisation
Fully characterise a range of plasmas: RF, DC, ECR and pulsed plasmas, including neutrals and neutral radicals. Extend your analyses to atmospheric pressure processes using the HPR-60, with time-resolved mass/energy analysis.

www.HidenAnalytical.com   info@hiden.co.uk

This content was downloaded from IP address 168.7.241.204 on 06/01/2025 at 20:14

OPEN ACCESS
IOP Publishing
Reports on Progress in Physics
Rep. Prog. Phys. 87 (2024) 117601 (33pp)
https://doi.org/10.1088/1361-6633/ad7b70

Exact results of the one-dimensional repulsive Hubbard model

Jia-Jia Luo[1,2], **Han Pu**[3] and **Xi-Wen Guan**[1,4,5,6,*]

[1] Innovation Academy for Precision Measurement Science and Technology, Chinese Academy of Sciences, Wuhan 430071, People's Republic of China
[2] University of Chinese Academy of Sciences, Beijing 100049, People's Republic of China
[3] Department of Physics and Astronomy, Rice University, Houston, TX 77251-1892, United States of America
[4] Hefei National Laboratory, Hefei 230088, People's Republic of China
[5] NSFC-SPTP Peng Huanwu Center for Fundamental Theory, Xi'an 710127, People's Republic of China
[6] Department of Fundamental and Theoretical Physics, Research School of Physics, Australian National University, Canberra ACT 0200, Australia

E-mail: xwe105@wipm.ac.cn and xiwen.guan@anu.edu.au

Received 29 July 2023, revised 11 August 2024
Accepted for publication 16 September 2024
Published 3 October 2024

Corresponding editor: Mrs Natasha Leeper

Abstract

We present analytical results of the fundamental properties of the one-dimensional (1D) Hubbard model with a repulsive interaction. The new model results with arbitrary external fields include: (I) using the exact solutions of the Bethe ansatz equations of the Hubbard model, we first rigorously calculate the gapless spin and charge excitations, exhibiting exotic features of fractionalized spinons and holons. We then investigate the gapped excitations in terms of the spin string and the $k-\Lambda$ string bound states at arbitrary driving fields, showing subtle differences in spin magnons and charge η-pair excitations. (II) For a high-density and high spin magnetization region, i.e. near the quadruple critical point, we further analytically obtain the thermodynamic properties, dimensionless ratios and scaling functions near quantum phase transitions. (III) Importantly, we give the general scaling functions at quantum criticality for arbitrary filling and interaction strength. These can directly apply to other integrable models. (IV) Based on the fractional excitations and the scaling laws, the spin-incoherent Luttinger liquid (SILL) with only the charge propagation mode is elucidated by the asymptotic of the two-point correlation functions with the help of conformal field theory. We also, for the first time, obtain the analytical results of the thermodynamics for the SILL. (V) Finally, to capture deeper insights into the Mott insulator and interaction-driven criticality, we further study the double occupancy and propose its associated contact and contact susceptibilities, through which an adiabatic cooling scheme based upon quantum criticality is proposed. In this scenario, we build up general relations among arbitrary external- and internal-potential-driven quantum phase transitions, providing a comprehensive understanding of quantum criticality. Our methods offer rich perspectives of quantum integrability and offer promising guidance for future experiments with interacting electrons and ultracold atoms, both with and without a lattice.

---

[*] Author to whom any correspondence should be addressed.

Supplementary material for this article is available online

Keywords: repulsive Hubbard model, fractional excitations, thermodynamics, spin-incoherent Luttinger liquid, quantum cooling, interaction-driven criticality

1. Introduction

The strongly correlated electronic systems provide us with a powerful platform to investigate novel and intriguing many-body phenomena, such as high-T_c superconductors [1–4], Mott metal–insulator transition [5–9], colossal magnetoresistance [2, 10] and antiferromagnetic correlations [11–19], which cannot be merely explained by compounding of single particle motions. Among the continuum and lattice models of interacting electrons and ultracold atoms, one of the prototypical integrable models is the one-band Hubbard model [20–22]. Recently, particular attention has been paid to this model because of its operability and accessibility in trapping ultracold atoms on lattices [8, 23–26]. There have been numerous publications focusing on the 1D Hubbard model with on-site interaction as well as its variants in one or higher dimensions [27–33], involving the studies of spectral weights and critical exponents for correlation functions [6, 7, 34–37], dynamical transport [36, 38–41], interaction quench [42–44], etc. In this scenario, the well-celebrated Landau theory of Fermi liquid [45, 46] remarkably captures essential universal low-energy physics of interacting fermions and leads to a wide range of applications in higher-dimensional quantum many-body systems.

On the other hand, the low-energy excitations of 1D many-body systems usually lack individual motions of quasiparticles. Instead, they form collective motions of bosons, i.e. Tomonaga–Luttinger liquid (TLL) [47–49]. A hallmark of interacting electrons in one dimension is the splitting of low-lying spin and charge excitations into two separate collective motions [26, 50–58], i.e. one solely carrying spin and the other carrying charge. This is one of the most significant features predicted by both the integrable theory and the TLL theory, namely, the propagators generated by excitations separate into two massless wave packets with distinctive velocities, v_c, v_s, in charge and spin degrees of freedom, respectively [51, 53, 59, 60]. The experimental evidence spin–charge separation phenomenon was reported in [54, 58, 61–63]. This phenomenon was further evidenced by detecting spin and charge propagating velocities [26, 54] by quenching an initial Mott state into few-hole doped states in the 1D Hubbard model. Meanwhile, some high-energy or gapped excitations may contribute to the optical conductivity [64]. The spin–charge separation has recently been verified and confirmed by virtue of spin and charge dynamical structure factors in 1D Fermi gas of ultracold atoms [58]. In this research, the team used Bragg beams to excite spin and charge density waves separately and measured the corresponding spin and charge Bragg spectra at different interacting strengths.

By taking into account the curvature correction to the linear charge excitation spectrum and the nonlinear effect of the spin backward scattering in the spin sector, the theoretical and experimental results are in good agreement. Nevertheless, when the temperature T exceeds a characteristic energy scale of spin, but is still less than the typical energy of charge of Fermi energy, i.e. $E_s \ll T \ll E_c$, the spin degrees of freedom are fully disordered, while the charge degrees of freedom remain in propagating mode. Such a state is referred to as spin-incoherent Luttinger liquid (SILL) [65–70]. The correlation function of the SILL shows an exponential decay of distance in the spin sector, while it remains a power-law decay in the charge sector, giving a characteristic of the emergent SILL [65–68], in contrast to the usual TLL where the correlation functions in both spin and charge sectors exhibit power-law decay in distance [6, 34, 71–73]. Evidence for the SILL was recently reported by Hulet's group at Rice University [74]. Although there have been extensive studies on this model, a comprehensive study of the spin-coherent and incoherent Luttinger liquids, the universal thermodynamics, fractional quasiparticles and Mott phase in the 1D Hubbard model remain elusive.

Moreover, compared with continuum gas systems, one has a consensus that the Mott insulator phase dominated by antiferromagnetic ordering is of great importance due to its uniqueness stemming from the Umklapp scattering in terms of bosonization [75]. There have been ample thoughts and debates on the mechanism for the onset of the Mott insulator for a long time [7, 76–78]. However, it remains a serious theoretical challenge to capture the essential nature of the insulating phase. This massive charge sector with a massless spin degree belongs to the category of the Luther–Emery model [79–81], whose dynamical spectral function for the Mott phase displays one or two singularities without anomalous dimension [80, 81]. A quantity which is experimentally accessible is the double occupancy, embodying charge fluctuations. It gives insights into the emergence of the Mott phase [30, 31, 82] and conveys plentiful information apart from the Mott phenomenon: for instance, the Pomeranchuk effect [30, 31, 33], antiferromagnetic correlations [33, 83, 84], and adiabatic cooling [31, 85, 86] over wide energy scales and temperature regimes. One of the key aims in this paper is to define the contact and contact susceptibilities, through which we further study the adiabatic cooling scheme at quantum criticality.

The Bethe ansatz provides us with a powerful method to study the 1D Hubbard Hamiltonian [20, 87]. The framework of building up the finite-temperature thermodynamics of 1D integrable systems can be traced to Yang and Yang's

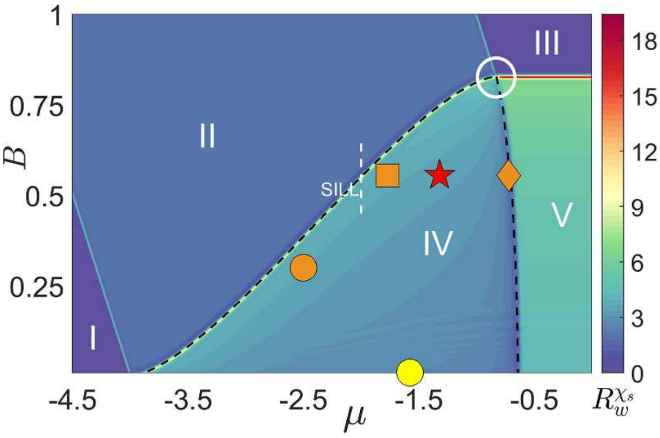

Figure 1. The phase diagram of the 1D repulsive Hubbard model at fixed interaction $u = 1$, of which the details are given in section 3.1. The orange, yellow and red symbols indicate the locations of excitations plotted in the figures in section 2. The white empty circle in the upper right area containing the quadruple critical point denotes the regions studied in section 3.1. The white dashed line denoted by SILL depicts the quantum phase transition from phase IV to II, which will be investigated in detail in section 3.2.

seminal paper [88]. Later, Takahashi took an important step forward by treating the thermodynamics of some more complicated integrable systems, and coined the name thermodynamic Bethe ansatz (TBA) [21]. In this scenario, a quantum transfer matrix was successfully developed for the study of the thermodynamics of integrable models in terms of the path integral [89, 90]. These two approaches endow us with the possibility to acquire the excitation spectra [91, 92], universal free Luttinger liquids information [57] and correlation functions [34, 36] for both the repulsive and the attractive Hubbard model [92–103], despite significant challenges in the actual calculations of physical properties due to the complexity of the TBA equations at arbitrary temperature. For higher dimensionality and various lattice symmetries [27–29, 32], there does not seem to be any completely applicable theoretical schemes, and commonly exploited numerical simulation methods include quantum Monte Carlo methods [28, 33, 37, 86], matrix-decomposition algorithms [104], dynamical mean-field theory [27, 32, 33], exact diagonalization [105, 106], perturbation theory [107, 108], density-Matrix renormalization groups [44, 53] and other generalizations [29, 108].

Using the TBA approach, the 1D repulsive Hubbard model is shown to contain five phases in the parameter space spanned by the chemical potential and the magnetic field, see figure 1: (I) vacuum; (II) partially filled and spin fully polarized state; (III) half-filled and spin fully polarized state; (IV) partially filled and magnetized band; (V) half-filled magnetized band, also referred to as the Mott insulator. In this paper we aim to present general analytical results of the thermodynamics, independent of microscopic details, of the model. To smoothly carry out the subsequent discussions on the fundamental properties of different states, we mark the locations and the regions in the phase diagram in figure 1, which we will study in this paper.

The elementary excitations in spin and charge sectors and the universal thermodynamics of the 1D repulsive Hubbard model are briefly discussed in [109]. In this paper, we develop analytical methods to obtain fundamental properties of the 1D Hubbard model with repulsive interaction and in the presence of external fields. In particular, using the exact solutions of the Bethe ansatz equations of the Hubbard model, we rigorously calculate fractional excitation spectra, universal thermodynamics, scaling functions, incoherent correlation functions, contact, contact susceptibilities, quantum cooling and interaction-driven quantum phase transitions in a pedagogical way. The exact results of various excitation spectra reveal exotic features of fractionalized spinons and holons, and show subtle differences in spin magnons and charge η-pair excitations. Universal thermodynamic properties of spin and charge Luttinger liquids, and dimensionless ratios and scaling functions near quantum phase transitions in terms of the chemical potential, magnetic field and interaction are obtained explicitly near the quadruple critical point. The asymptotic two-point correlation functions for the SILL are derived with the help of the conformal field theory. Finally, we study the double occupancy, the contact, contact susceptibilities, interaction-driven adiabatic cooling scheme, and the criticality and Mott insulator behaviour of the model as well.

The outline of this paper is as follows. In section 2, we introduce the basic knowledge of the exact Bethe ansatz solution of the repulsive Hubbard model and calculate the excitation spectra of fractional holons and spinons as well as the gapped excitations above the ground state. In section 3.1, using our newly developed methods, we initiate our study on the thermal and magnetic properties of TLL, quantum criticality, non-Fermi liquid behaviour and the universal laws in the 1D Hubbard model. In section 3.2, we study the SILL from the Bethe ansatz and quantum phase transition perspective. The asymptotic single-particle Green's function and pairing correlation function are presented. A depiction of double occupancy and analytical calculation of contact and its susceptibilities with respect to the chemical potential, magnetic field and interaction near the Mott phase are given in section 3.3. In this section, we also carry out a detailed analysis on quantum cooling and interaction-driven phase transitions. Section 4 presents a summary and outlooks.

2. Fractional holons and spinons

Fundamental low-energy physics is intimately related to the elementary excitations in 1D many-body systems. In particular, the low-lying excited states involve many-body correlations and determine the unique dynamics of the 1D Hubbard model, showing novel features of fractional holons and spinons. In the Mott phase, the excitations show a charge gapped phase with antiferromagnetic correlations in the spin sector. Spin and charge particle–hole excitations reveal the origins of the spin-coherent TLL and spin-incoherent liquid in a crossover temperature regime. The purpose of this section is to calculate typical excitation spectra of the repulsive Hubbard model, which complements the study in the literature: see a review [22].

2.1. Bethe ansatz equations and root patterns

For self-containment, here we first introduce relevant notations and recall some fundamental equations with respect to the Bethe ansatz solutions used in this paper. In the presence of external potentials, the 1D Hamiltonian of the Hubbard model is given by

$$\begin{aligned} H = &-\sum_{j=1}^{L}\sum_{a=\uparrow\downarrow}\left(c^{+}_{j,a}c_{j+1,a}+c^{+}_{j+1,a}c_{j,a}\right) \\ &+u\sum_{j=1}^{L}\left(1-2n_{j\uparrow}\right)\left(1-2n_{j\downarrow}\right)-\mu\hat{N}-2B\hat{S}_z, \end{aligned} \tag{1}$$

where $c^{\dagger}_{j,a}$ and $c_{j,a}$ are the creation and annihilation operators of fermions with spin $a(a=\uparrow,\downarrow)$ at site j in a periodic lattice of length L, $n_{j\sigma}$ is the particle density operator of spin σ at site j, $\hat{N}=\sum_{j=1}^{L}(n_{j\uparrow}+n_{j\downarrow})$ is the total number particle operator, and $\hat{S}_z=\frac{1}{2}\sum_{j=1}^{L}(n_{j\uparrow}-n_{j\downarrow})$ is the magnetization operator. The hopping amplitude is set to unity, which also sets the units for energy. The chemical potential μ and magnetic field B are rescaled with respect to the hopping term. Here, u represents the on-site interaction between particles of opposite spins: $u>0$ for repulsion, and $u<0$ for attraction. The repulsive and the attractive Hubbard model can be converted into each other via the Shiba transformation. In addition to the hopping amplitude, we choose a unit system by setting k_B, $\hbar$ to 1 throughout the paper.

In the absence of the external potential $(\mu=0, B=0)$ and even lattice sites, the Hamiltonian (1) possesses $\mathrm{SO}(4)\cong\mathrm{SU}(2)\times\mathrm{SU}(2)/\mathbb{Z}_2$ full symmetry composed of spin rotation and η-pairing invariance [92]:

$$[H,S^{\alpha}]=0, \qquad [H,\eta^{\alpha}]=0, \tag{2}$$

where the spin and η-pair operators are given by

$$\begin{aligned} S^{\alpha}=&\frac{1}{2}\sum_{j=1}^{L}\sum_{a,b=\uparrow,\downarrow}c^{+}_{j,a}\left(\sigma^{\alpha}\right)^{a}_{b}c_{j,b}, \\ \eta^{x}=&-\frac{1}{2}\sum_{j=1}^{L}(-1)^{j}\left(c^{+}_{j,\uparrow}c^{+}_{j,\downarrow}+c_{j,\uparrow}c_{j,\downarrow}\right), \\ \eta^{y}=&\frac{i}{2}\sum_{j=1}^{L}(-1)^{j}\left(c^{+}_{j,\uparrow}c^{+}_{j,\downarrow}-c_{j,\uparrow}c_{j,\downarrow}\right), \\ \eta^{z}=&\frac{1}{2}\left(N-L\right), \end{aligned} \tag{3}$$

which are useful for the analysis of elementary excitations at a zero magnetic field and half-filled band [92]. In the above equation, σ^{α} with $\alpha=x,y,z$ denote the Pauli matrices.

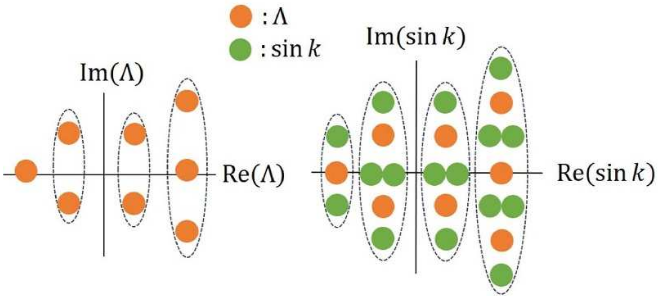

Figure 2. The string patterns of Λ strings (left configurations) and $k-\Lambda$ strings (right configurations). The left Λ strings show one length-1, two length-2 and one length-3 Λ strings. The right $k-\Lambda$ strings involve one length-1 $k-\Lambda$ string, two length-2 $k-\Lambda$ strings and one length-3 $k-\Lambda$ string.

On a lattice model, the average particle number per site denoted by n_c can vary from 0 to 2. In this paper, we will consider the case where the particle number per site is no larger than one with the magnetization denoted by m less than $n_c/2$ for repulsive interaction, i.e. it corresponds to a negative chemical potential and positive magnetic field. The regions for $n_c>1, m>n_c/2$ are related to that studied here in terms of discrete symmetries [22].

The eigenvalues of $\{k\}$, $\{\Lambda\}$, which are, respectively, the solutions of charge quasi-momentum and spin rapidity of this model, can be obtained by solving the Lieb–Wu equations [20]. Meanwhile, Takahashi [21] assumed that the quasi-momenta $\{k\}$, $\{\Lambda\}$ exhibit different patterns, which determine the full states of the model. The root patterns of the repulsive Hubbard model can be categorized into three types: single real k, length-n Λ strings composed of n spin-down electrons, and length-m $k-\Lambda$ string containing m spin-down and m spin-up particles, see figure 2 and also [92]. Let M_e, M_n, M'_n denote the number of k, Λ strings and $k-\Lambda$ strings of length n, respectively. Therefore, the total particle number N and spin-down electron number M read:

$$\begin{aligned} M=&\sum_{n=1}^{\infty}n\left(M_n+M'_n\right), \\ N=&\mathcal{M}_e+\sum_{n=1}^{\infty}2nM'_n. \end{aligned} \tag{4}$$

For the ease of discussion, we choose to present the following Bethe ansatz equations and the TBA equations of the 1D repulsive Hubbard model, based on which, we will analytically derive the physical properties of the model. In terms of the string solutions, the real centres of these roots satisfy the so-called Takahashi's forms of Bethe ansatz equations [21]:

$$
\begin{aligned}
k_jL &= 2\pi I_j - \sum_{n=1}^{\infty}\sum_{\alpha=1}^{M_n}\theta\left(\frac{\sin k_j-\Lambda_\alpha^n}{nu}\right)\\
&\quad -\sum_{n=1}^{\infty}\sum_{\alpha=1}^{M'_n}\theta\left(\frac{\sin k_j-\Lambda_\alpha^{\prime n}}{nu}\right),\\
\sum_{j=1}^{N-2M'}\theta\left(\frac{\Lambda_\alpha^n-\sin k_j}{nu}\right) &= 2\pi J_\alpha^n+\sum_{m=1}^{\infty}\sum_{\beta=1}^{M_m}\Theta_{nm}\left(\frac{\Lambda_\alpha^n-\Lambda_\beta^m}{u}\right),\\
2L\,\mathrm{Re}\left[\arcsin\left(\Lambda_\alpha^{\prime n}+n\mathrm{i}u\right)\right] &= 2\pi J_\alpha^{\prime n}+\sum_{j=1}^{N-2M'}\theta\left(\frac{\Lambda_\alpha^{\prime n}-\sin k_j}{nu}\right)\\
&\quad +\sum_{m=1}^{\infty}\sum_{\beta=1}^{M'_m}\Theta_{nm}\left(\frac{\Lambda_\alpha^n-\Lambda_\beta^{\prime m}}{u}\right),
\end{aligned}
\tag{5}
$$

where $\theta(x)=2\arctan(x)$ and Θ_{nm} is defined as

$$
\Theta_{nm}(x)=\begin{cases}\theta\left(\frac{x}{|n-m|}\right)+2\theta\left(\frac{x}{|n-m|+2}\right)+\cdots+2\theta\left(\frac{x}{n+m-2}\right)+\theta\left(\frac{x}{n+m}\right),\ \text{if}\ n\neq m\\ 2\theta\left(\frac{x}{2}\right)+2\theta\left(\frac{x}{4}\right)+\cdots+2\theta\left(\frac{x}{2n-2}\right)+\theta\left(\frac{x}{2n}\right),\text{if}\ n=m\end{cases}.
\tag{6}
$$

The counting numbers $I_j, J_\alpha^n, J_\alpha^{\prime n}$ are integer or half-odd integers, which rely on the odevity of the string number,

$$
I_j\ \text{is}\ \begin{cases}\text{integer} & \text{if}\ \sum_m\left(M_m+M'_m\right)\ \text{is even}\\ \text{half-odd integer} & \text{if}\ \sum_m\left(M_m+M'_m\right)\ \text{is odd}\end{cases},
\tag{7}
$$

$$
J_\alpha^n\ \text{is}\ \begin{cases}\text{integer} & \text{if}\ N-M_n\ \text{is odd}\\ \text{half-odd integer} & \text{if}\ N-M_n\ \text{is even,}\end{cases},
\tag{8}
$$

$$
J_\alpha^{\prime n}\ \text{is}\ \begin{cases}\text{integer} & \text{if}\ L-N+M'_n\ \text{is odd}\\ \text{half-odd integer} & \text{if}\ L-N+M'_n\ \text{is even}\end{cases}.
\tag{9}
$$

The classification of these quantum numbers will be needed to characterize the excitations, which will be presented later.

Every selected set of quantum numbers $I_j, J_\alpha^n, J_\alpha^{\prime n}$ uniquely determine the value of quasi-momenta k_j, Λ_α^n, $\Lambda_\alpha^{\prime n}$, and thus yield a specific eigenstate of the model. These numbers are in the ranges of

$$
\begin{aligned}
&-\frac{L}{2}<I_j\leqslant\frac{L}{2},\\
&|J_\alpha^n|\leqslant\frac{1}{2}\left(N-2M'-\sum_{m=1}^{\infty}t_{nm}M_m-1\right),\\
&|J_\alpha^{\prime n}|\leqslant\frac{1}{2}\left(L-N+2M'-\sum_{m=1}^{\infty}t_{nm}M'_m-1\right),
\end{aligned}
\tag{10}
$$

where $M'=\sum_{n=1}^{\infty}nM'_n$ is the entire number of spin-down particles included in $k-\Lambda$ strings, and $t_{mn}=2\min(m,n)-\delta_{mn}$.

Denoting $\rho^p, \sigma_n^p, \sigma_n^{\prime p}$ ($\rho^h, \sigma_n^h, \sigma_n^{\prime h}$) as the densities of real quasi-momenta k, the real part of the length-n spin strings and the real part of length-n $k-\Lambda$ strings for particles (holes), the root distributions of these types of root patterns are given by [21]

$$
\begin{aligned}
\rho^p(k)+\rho^h(k) &= \frac{1}{2\pi}+\cos k\sum_{n=1}^{\infty}\int_{-\infty}^{\infty}\mathrm{d}\Lambda a_n(\Lambda-\sin k)\\
&\quad\times\left(\sigma_n^{\prime p}(\Lambda)+\sigma_n^p(\Lambda)\right),\\
\sigma_n^p(\Lambda)+\sigma_n^h(\Lambda) &= -\sum_{m=1}^{\infty}A_{nm}*\sigma_m^p(\Lambda)\\
&\quad+\int_{-\pi}^{\pi}\mathrm{d}ka_n(\sin k-\Lambda)\rho^p(k),\\
\sigma_n^{\prime p}(\Lambda)+\sigma_n^{\prime h}(\Lambda) &= \frac{1}{\pi}\mathrm{Re}\frac{1}{\sqrt{1-(\Lambda-\mathrm{i}nu)^2}}\\
&\quad-\sum_{m=1}^{\infty}A_{nm}*\sigma_m^{\prime p}(\Lambda)\\
&\quad-\int_{-\pi}^{\pi}\mathrm{d}ka_n(\sin k-\Lambda)\rho^p(k),
\end{aligned}
\tag{11}
$$

respectively. In the above equations $a_n(x)=\frac{1}{2\pi}\frac{2nu}{(nu)^2+x^2}$, and the convolution term denoted by $*$ denotes a convolution

$$
A_{nm}*f(x)=\int_{-\infty}^{\infty}\frac{\mathrm{d}y}{2\pi}\frac{\mathrm{d}}{\mathrm{d}x}\Theta_{nm}\left(\frac{x-y}{u}\right)f(y).
\tag{12}
$$

The function A_{nm} denotes a derivative of the function Θ_{nm}, namely,

$$A_{nm}\left(\frac{x-y}{u}\right)=\frac{1}{2\pi}\frac{\mathrm{d}}{\mathrm{d}x}\Theta_{nm}\left(\frac{x-y}{u}\right)$$
$$=\begin{cases} a_{|n-m|}\left(x-y\right)+2a_{|n-m|+2}\left(x-y\right)+\cdots+2a_{n+m-2}\left(x-y\right)+a_{n+m}\left(x-y\right), \text{ if } n\neq m \\ 2a_2\left(x-y\right)+2a_4\left(x-y\right)+\cdots+2a_{2n-2}\left(x-y\right)+a_{2n}\left(x-y\right), \text{if } n=m \end{cases}. \tag{13}$$

Following the Yang–Yang method [88], the true physical equilibrium states at finite temperature can be determined by the minimization of the free energy with respect to the densities. The TBA equations for dressed energies $\kappa(k),\varepsilon_n(\Lambda),\varepsilon'_n(\Lambda)$, associated with the product of the logarithm of the ratio of the hole density to the particle density and temperature $\kappa=T\ln\left(\frac{\rho^h}{\rho^p}\right),\varepsilon_n=T\ln\left(\frac{\sigma_n^h}{\sigma_n^p}\right),\varepsilon'_n=T\ln\left(\frac{\sigma_n'^h}{\sigma_n'^p}\right)$, are given by the following form [21]

$$\begin{aligned}\kappa\left(k\right)=&-2\cos k-\mu-2u-B\\&+\sum_{n=1}^{\infty}\int_{-\infty}^{\infty}\mathrm{d}\Lambda a_n\left(\sin k-\Lambda\right)T\ln\left(1+\mathrm{e}^{-\frac{\varepsilon'_n(\Lambda)}{T}}\right)\\&-\sum_{n=1}^{\infty}\int_{-\infty}^{\infty}\mathrm{d}\Lambda a_n\left(\sin k-\Lambda\right)T\ln\left(1+\mathrm{e}^{-\frac{\varepsilon_n(\Lambda)}{T}}\right),\end{aligned}\tag{14}$$

$$\begin{aligned}\varepsilon_n\left(\Lambda\right)=&\,2nB-\int_{-\pi}^{\pi}\mathrm{d}k\cos k a_n\left(\sin k-\Lambda\right)T\ln\left(1+\mathrm{e}^{-\frac{\kappa(k)}{T}}\right)\\&+\sum_{m=1}^{\infty}A_{nm}*T\ln\left(1+\mathrm{e}^{-\frac{\varepsilon_m(\Lambda)}{T}}\right),\end{aligned}\tag{15}$$

$$\begin{aligned}\varepsilon'_n\left(\Lambda\right)=&\,4\mathrm{Re}\sqrt{1-\left(\Lambda-\mathrm{i}nu\right)^2}-2n\mu-4nu\\&-\int_{-\pi}^{\pi}\mathrm{d}k\cos k a_n\left(\sin k-\Lambda\right)T\ln\left(1+\mathrm{e}^{-\frac{\kappa(k)}{T}}\right)\\&+\sum_{m=1}^{\infty}A_{nm}*T\ln\left(1+\mathrm{e}^{-\frac{\varepsilon'_m(\Lambda)}{T}}\right).\end{aligned}\tag{16}$$

It is observed that the above dressed energies are even functions with respect to their variables and exhibit monotonically increasing behaviour in the positive argument space. The Gibbs free energy per site is given by

$$\begin{aligned}f=&-T\int_{-\pi}^{\pi}\frac{\mathrm{d}k}{2\pi}\ln\left(1+\mathrm{e}^{-\frac{\kappa(k)}{T}}\right)+u\\&-T\sum_{n=1}^{\infty}\int_{-\infty}^{\infty}\frac{\mathrm{d}\Lambda}{\pi}\mathrm{Re}\frac{1}{\sqrt{1-\left(\Lambda-\mathrm{i}nu\right)^2}}\ln\left(1+\mathrm{e}^{-\frac{\varepsilon'_n(\Lambda)}{T}}\right),\end{aligned}\tag{17}$$

which serves as the equation of state, from which one can directly obtain the profiles of the ground state and thermodynamic properties of the Hubbard model at zero and finite temperatures by solving equations (14)–(16). However, finding the solution to the TBA equations (14)–(16) imposes a significant theoretical challenge. As a result, a comprehensive study of universal thermodynamics, Luttinger liquid properties, magnetic properties and scaling functions in the vicinities of the critical points, as well as the behaviour of the Mott phase and quantum cooling in the 1D Hubbard model is still incomplete in the literature.

2.2. Ground state

In the limit of zero temperature, one can see that the dressed energies of the length-n Λ strings with $n>1$ and all $k-\Lambda$ are always positive in the parameter space. Consequently, they do not contribute to zero-temperature thermal and magnetic properties. The real k and length-1 Λ string should be cut off at the points where the dressed energies change sign. Thereby, in the ground state, the coupled equations for the dressed energies, densities and hole distribution functions [20] are greatly simplified

$$\begin{aligned}\kappa\left(k\right)=&-2\cos k-\mu-2u-B\\&+\int_{-A}^{A}\mathrm{d}\Lambda a_1\left(\sin k-\Lambda\right)\varepsilon_1\left(\Lambda\right),\end{aligned}\tag{18}$$

$$\begin{aligned}\varepsilon_1\left(\Lambda\right)=&\,2B+\int_{-Q}^{Q}\mathrm{d}k\cos k a_1\left(\sin k-\Lambda\right)\kappa\left(k\right)\\&-\int_{-A}^{A}\mathrm{d}\Lambda' a_2\left(\Lambda-\Lambda'\right)\varepsilon_1\left(\Lambda'\right),\end{aligned}\tag{19}$$

$$\begin{aligned}\rho^p\left(k\right)=&\,\theta_{\mathrm{H}}\left(Q-|k|\right)\left[\frac{1}{2\pi}+\cos k\int_{-A}^{A}\mathrm{d}\Lambda a_1\right.\\&\left.\times\left(\sin k-\Lambda\right)\sigma_1^p\left(\Lambda\right)\right],\end{aligned}$$

$$\begin{aligned}\sigma_1^p\left(\Lambda\right)=&\,\theta_{\mathrm{H}}\left(A-|\Lambda|\right)\left[-\int_{-A}^{A}\mathrm{d}\Lambda' a_2\left(\Lambda-\Lambda'\right)\sigma_1^p\left(\Lambda'\right)\right.\\&\left.+\int_{-Q}^{Q}\mathrm{d}k a_1\left(\sin k-\Lambda\right)\rho^p\left(k\right)\right],\end{aligned}$$

$$\begin{aligned}\rho^h\left(k\right)=&\,\theta_{\mathrm{H}}\left(|k|-Q\right)\left[\frac{1}{2\pi}+\cos k\int_{-A}^{A}\mathrm{d}\Lambda a_1\right.\\&\left.\times\left(\sin k-\Lambda\right)\sigma_1^p\left(\Lambda\right)\right],\end{aligned}$$

$$\begin{aligned}\sigma_1^h\left(\Lambda\right)=&\,\theta_{\mathrm{H}}\left(|\Lambda|-A\right)\left[-\int_{-A}^{A}\mathrm{d}\Lambda' a_2\left(\Lambda-\Lambda'\right)\sigma_1^p\left(\Lambda'\right)\right.\\&\left.+\int_{-Q}^{Q}\mathrm{d}k a_1\left(\sin k-\Lambda\right)\rho^p\left(k\right)\right],\end{aligned}$$

$$\sigma_n^h(\Lambda) = -A_{n1} * \sigma_1^p(\Lambda) + \int_{-Q}^{Q} \mathrm{d}k a_n(\sin k - \Lambda)\rho^p(k), \text{ for, } n \geqslant 2,$$

$$\sigma_n'^h(\Lambda) = \frac{1}{\pi}\mathrm{Re}\frac{1}{\sqrt{1-(\Lambda - \mathrm{i}nu)^2}} - \int_{-Q}^{Q} \mathrm{d}k a_n(\sin k - \Lambda)\rho^p(k),$$

where Q, A are the Fermi points of charge and spin, respectively, determined by $\kappa(Q) = 0, \varepsilon_1(A) = 0$, and θ_H is the Heaviside step function. We observe that particles only exist within Fermi points, while holons locate outside in the ground state. In the above equations, we also present the hole density distribution functions for Λ strings and $k-\Lambda$ strings for our later calculation. By defining the total quantities $\rho = \rho^p + \rho^k, \sigma_1 = \sigma_1^p + \sigma_1^h$, the density Bethe ansatz equations can thus be recast in a more succinct form

$$\rho(k) = \frac{1}{2\pi} + \cos k \int_{-A}^{A} \mathrm{d}\Lambda a_1(\Lambda - \sin k)\sigma_1(\Lambda), \tag{20}$$

$$\sigma_1(\Lambda) = -\int_{-A}^{A} \mathrm{d}\Lambda' a_2(\Lambda - \Lambda')\sigma_1(\Lambda') + \int_{-Q}^{Q} \mathrm{d}k a_1(\sin k - \Lambda)\rho(k). \tag{21}$$

Thus, the average total particle number per size and the average spin-down particle number per size can be expressed in terms of equations (20) and (21) as

$$n_c = \int_{-Q}^{Q} \mathrm{d}k\rho(k), \tag{22}$$

$$n_\downarrow = \int_{-A}^{A} \mathrm{d}\Lambda\sigma_1(\Lambda). \tag{23}$$

The momenta of the charge and spin quasiparticles for $|k| \leqslant Q$, $|\Lambda| \leqslant A$, and holons for $|k| > Q, |\Lambda| > A$ in terms of the quasi-momentum parameters $k_j, \Lambda_\alpha^n, \Lambda_\alpha'^n$ can be calculated via the following expressions

$$p(k) = \frac{2\pi I_k}{L} = 2\pi\int_0^k \mathrm{d}k'\rho(k'), \tag{24}$$

$$p_1(\Lambda) = \frac{2\pi J_1}{L} = 2\pi\int_0^\Lambda \mathrm{d}\Lambda'\sigma_1(\Lambda'), \tag{25}$$

$$p_n(\Lambda) = \frac{2\pi J_n}{L} = 2\pi\int_0^\Lambda \mathrm{d}\Lambda'\sigma_n^h(\Lambda'), \ n \geqslant 2, \tag{26}$$

$$p_n'(\Lambda) = \frac{2\pi J_n'}{L} = -2\pi\int_0^\Lambda \mathrm{d}\Lambda'\sigma_n'^h(\Lambda') + \pi(n+1), \ n \geqslant 1. \tag{27}$$

Let us denote N_GS as the total particle number, and M_GS as the spin-down number in the ground state. Consider the ground-state structure in the presence of a magnetic field and $0 < n_c < 1$ as follows (assume the lattice length L is even): $M_e = N_\mathrm{GS} = 2 * M_\mathrm{GS} < L$, $M_1 = M_\mathrm{GS}$ is an odd number and less than $N_\mathrm{GS}/2$, $M_n = 0$ for $n \geqslant 2, M_n' = 0$ for $n \geqslant 1$; that is, both charge and spin sectors are partially filled, and all particles form charge and spin Fermi seas, the inside of which are referred to as antiholon states for charge and spinon states for spin degrees of freedom. At zero temperature, the system lies in its lowest energy state and particles are symmetrically distributed around zero momentum. Using equations (7), (8) and (24)–(27), we can evaluate that $\{I_j\}$ are half-odd integers and fill in the interval $\left[-\frac{N_\mathrm{GS}-1}{2}, \frac{N_\mathrm{GS}-1}{2}\right]$, whereas $\left\{J_\alpha^1\right\}$ are integers within $\left[-\frac{M_\mathrm{GS}-1}{2}, \frac{M_\mathrm{GS}-1}{2}\right]$. The momentum distribution $p(k), p_1(\Lambda)$ respectively covers the intervals of $[-\pi n_c, \pi n_c]$ and $[-\pi n_\downarrow, \pi n_\downarrow]$. It is inferred from equation (10) that the values for the quantum numbers $\left\{J_\alpha^1\right\}$ satisfy $\left|J_\alpha^1\right| \leqslant \frac{1}{2}(N_\mathrm{GS} - M_\mathrm{GS} - 1)$. This implies that there are $N_\mathrm{GS} - M_\mathrm{GS}$ vacancies for J_α^1 and thus $N_\mathrm{GS} - 2M_\mathrm{GS}$ holes are left. Building on the quantum numbers of the ground state, elementary excitations can be classified into two types: gapless and gapped excitations. Particle–hole excitations, as well as their combinations, belong to the gapless ones, which always occur in sufficient low-energy sectors. Whereas the length-n $k-\Lambda$ and Λ strings with $n > 1$ require additional energy to be excited. The key points for the excitation spectrum calculation are stated below:

- The dressed energy is an exact excitation energy of the particle with the corresponding momentum, and holon energy corresponds to the negative dressed energy. Basically, the energies of particle excitations for different types of quasiparticles are $\kappa(k)$, $\varepsilon_n(\Lambda)$ and $\varepsilon_n'(\Lambda)$, while their corresponding holon excitations are $-\kappa(k)$, $-\varepsilon_n(\Lambda)$ and $-\varepsilon_n'(\Lambda)$, respectively.
- By changing the quantum numbers M_e, M_n and M_n', one can analyze the excited structure with respect to the ground state to capture the holon or particle excitations of each type of string.
- If there is no extra hole or particle appearing over the ground state, the particle–hole excitation can exist. This type of excitation does not alter the total particle number or parity. The particle–hole excitations not only result in universal TLL in spin and charge sectors, but also essentially determine the dynamical correlation functions at low energy.
- Individual particle and holon excitations can be transformed into each other, e.g. in figure 3, a holon excitation can be created by conducting two particle–hole excitations over a particle excitation.
- When I_j changes from a half-odd (integer) to an integer (half-odd), extra constant momentum $\pm\pi n_c$ needs to be added to the total momentum with a change in parity. (In the later study, we only consider the case of πn_c, which is also relevant in the continuum model. The case for $-\pi n_c$ is symmetric with the former.). See, for example, figure 4.
- A multi-parametric excitation can be decomposed into few-parametric elementary excitations. Once a few particle excitations are determined, analytical expressions of multiple particle excitations are created by a few elementary

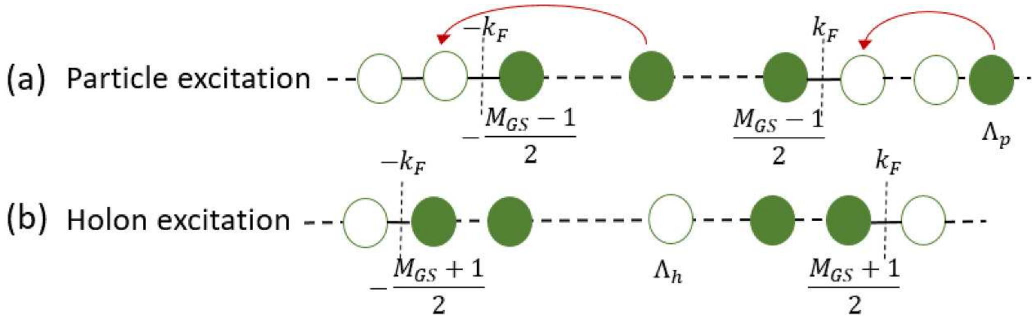

Figure 3. Illustration of two equivalent excitations: a transformation between particle excitation and holon excitation.

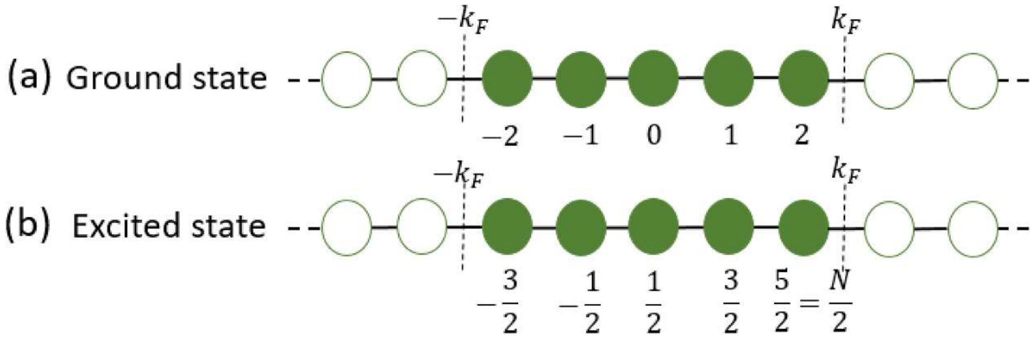

Figure 4. Illustration of the variation of parity in excitation.

excitations. We elucidate this approach in the supplementary material[7], e.g. $M_e = N_{\mathrm{GS}} + 2$ is composed of double excitations with $M_e = N_{\mathrm{GS}} + 1$.

The techniques outlined above enable us to classify the processes of complicated excitations, based on which we can conceive the unique collective nature of fractional excitations. Next, we will present various spectrum patterns of elementary excitations at different points of the phase diagram, as indicated in figure 1, which are helpful for later analysis.

2.3. Fractional charge and spin excitations

Elementary excitations of the Hubbard model were studied in the literature: see [22]. Here we present a comprehensive understanding of fractional excitations and various gapped excitations, which provide deep insights into Luttinger liquid, spin-incoherent liquid and low-energy physics.

2.3.1. Particle–hole and two-spinon excitations. We first study the elementary excitation of one spin flip, i.e. one spin-down particle in the ground state flips its spin, for which we have a change $M_e = L, M_1 = M_{\mathrm{GS}} - 1$. Here, we take M_{GS} to be an odd number. From equations (7) and (8), we can determine that the quantum numbers $\{I_j\}$ are integers and J^1_α are half-odd integers within the ranges $-\frac{L}{2} < I_j \leqslant \frac{L}{2}$ and $\left|J^1_\alpha\right| \leqslant \frac{1}{2}\left(N_{\mathrm{GS}} - M_{\mathrm{GS}}\right)$, respectively. Therefore the vacancies for spin are $N_{\mathrm{GS}} - M_{\mathrm{GS}} + 1$. In contrast to the ground state, one more vacancy arises with a diminished particle in the spin sector, and thus two holes, $\Lambda_{h1}, \Lambda_{h2}$, carrying separate spin $\frac{1}{2}$ are created in the spinon band for Λ. For this spin flipping excitation, η pairing and spin magnetization $(\Delta\eta^z, \Delta S^z)$ are determined through $\Delta\eta^z = \frac{\Delta N}{2}$, $\Delta S^z = \frac{\Delta N - 2\Delta M}{2}$ with N, M being the total particle number and spin-down number in the excited state, i.e. $(\Delta\eta^z, \Delta S^z) = (0, 1)$ in this sample. This excitation configuration is shown in figure 5.

On the other hand, the particle–hole excitation can be constructed in the charge sector with a particle taken out from $|k| < Q$ to $|k| > Q$, leaving a holon k_h inside the antiholon band and a particle k_p in the holon states. The energies and momenta of the particle–hole excitation in the charge sector and the two-spinon excitation in the spin sector are given by

$$E_{ph} = \kappa\left(k_p\right) - \kappa\left(k_h\right), \ P_{ph} = p\left(k_p\right) - p\left(k_h\right), \tag{28}$$

$$\begin{aligned} E_{ss} &= -\varepsilon_1\left(\Lambda_{h1}\right) - \varepsilon_1\left(\Lambda_{h2}\right), \\ P_{ss} &= -p_1\left(\Lambda_{h1}\right) - p_1\left(\Lambda_{h2}\right) + \pi n_c. \end{aligned} \tag{29}$$

In figure 6, we demonstrate the results of the particle–hole and the two-spinon excitations for various parameters. Obviously, one universal nature of low-energy excitation spectra is the existence of spin–charge separation behaviour [51, 53, 60], visualizing the theory of the spin–charge-separated TLL. In the absence of the magnetic field, the system has spin rotation symmetry. Figure 6(a) shows the particle–hole excitation in the charge sector away from the half-filled lattice

---

[7] See supplementary material in which we present some key derivations of the results on the gapped excitations, universal thermodynamics, free energy of phase III, magnetic properties, quantum criticality and general universal scaling functions for the 1D repulsive Hubbard model.

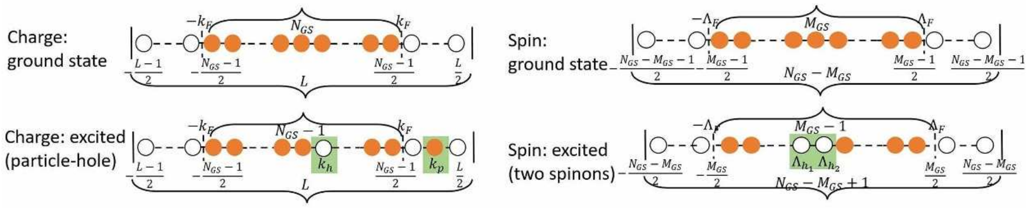

Figure 5. Illustration of the particle–hole excitation in the charge sector and two-spinon excitation in the spin sector.

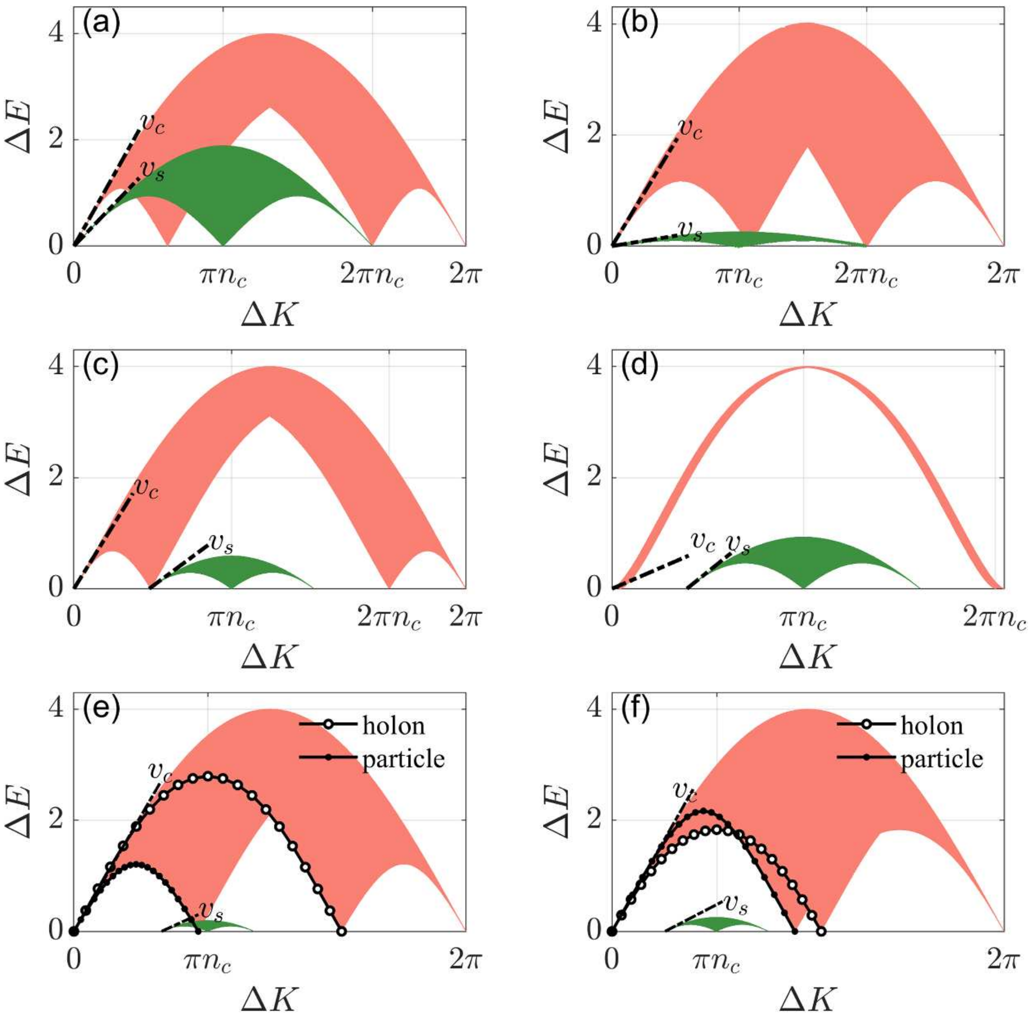

Figure 6. Elementary excitations in spin and charge sectors. The shaded area in orange represents a particle–hole excitation of charge, where one particle inside the Fermi sea is excited to outside at different fillings. Meanwhile, the shaded area in green presents a two-holon excitation in the spin sector. All the figures are drawn in the first Brillouin zone. The interaction u is fixed to unity for all the figures except (b). (a) For the case away from the half-filled band at zero magnetic field with $B=0, \mu=-1.5765$ corresponding to the yellow circle in figure 1, we have charge and spin sound velocities $v_c=2.0907$, $v_s=1.2259$ in the long wave length limit, respectively; (b) for strong coupling at zero magnetic field with $n_c=0.6496, u=10$, we have charge and spin sound velocities $v_c=1.8533, v_s=0.1824$ for the zero momentum limit, respectively. (c) We present a general case with the presence of magnetization, $B=0.555, \mu=-1.32$, corresponding to the red star in figure 1; (d) we present charge and spin excitations near the half-filled phase with a finite magnetization, $B=0.555, \mu=-0.722$, corresponding to the orange diamond in figure 1; (e) we demonstrate excitations near a spin-polarized band, $B=0.555, \mu=-1.77$, corresponding to the orange square in figure 1. At a low-energy scale, the holon excitation energy (empty-circles) is higher than the particle excitation energy (filled-circles); (f) we show excitations at $B=0.3, \mu=-2.5$ for a comparison with figure (e), corresponding to the orange circle in figure 1.

and the two-spinon excitation in the spin sector, which fully accounts for the first Brillouin zone.

In contrast, figure 6(b) shows the particle–hole excitation and the two-spinon excitation in the strong coupling limit, reminiscent of the spin–charge-separated spectra in the 1D Yang-Gaudin model [57]. The slopes of the dispersion are characterized by the velocities v_c, v_s, displaying $v_s \ll v_c$, which were recently measured experimentally in a quasi-1D trapped repulsive Fermi gas [58]. This regime offers a remarkable possibility to study the SILL, which occurs when the temperature exceeds the spin characteristic energy, but is still less than the charge energy. In the SILL, the spin degrees of freedom is frozen. However, the charge degrees of freedom propagates as a sound mode, behaving like spinless fermions [65–67].

Figures 6(c) and (d) present the particle–hole excitation and the two-spinon excitation for an arbitrary magnetic field, away from the half-filled and near half-filled regions, respectively. In these two cases, the spin degree is highly suppressed in the presence of the magnetic field. The spin and charge velocities are significantly different, and the spectra of spin and charge display a large separation. In particular, in figure 6(d), the charge band is very narrow, behaving like a single particle, which was experimentally studied in [26]. The spin velocity exceeds the sound velocity of charge. Figures 6(e) and (f) show that in the charge sector, the energy of holon excitation at small momentum can exceed that of particle excitation in the Hubbard model due to the cosine term presented in the charge dispersion, which is prohibited in the continuum model [57, 72]. Nevertheless, when the system approaches the Mott phase, the charge excitation gradually shrinks to the cases observed in figure 6(d), indicating an emergence of single-particle excitation in the charge sector [26]. In general, the spin sector exhibits similar behaviour to that of the Heisenberg chain [110, 111]. When a magnetic field is applied, the two-spinon excitation is no longer the low-energy one in the sense that it does not fill the entire Brillouin area. The role played by the low-energy excitation in the spin degrees of freedom is the spin particle–hole spectrum, as depicted in figure 7.

2.3.2. *Antiholon– and holon–spinon excitations.*

Let us further consider fractional holon and spinon excitations, induced by adding or removing a particle with spin up or down over the ground state in the Hubbard model. There are four configurations with the following quantum numbers: $(a) M_e = N_{\rm GS}+1, M_1 = M_{\rm GS}+1$, involving excitations of one antiholon particle in the charge and one spinon particle in the spin sector; (b) $M_e = N_{\rm GS}-1, M_1 = M_{\rm GS}$, involving excitations of one holon in the charge and one spinon particle in the spin sector; (c) $M_e = N_{\rm GS}+1, M_1 = M_{\rm GS}$, involving excitations of an antiholon particle in the charge and one spinon hole in the spin sector. This configuration is shown in figure 8; (d) $M_e = N_{\rm GS}-1, M_1 = M_{\rm GS}-1$, involving excitations of one holon in the charge and one spinon hole in the spin sector. These four excitations can be classified by the charge and spin magnetization values $(\Delta\eta^z, \Delta S^z)$: correspondingly, (a) the antiholon–spinon particle $(\frac{1}{2}, -\frac{1}{2})$, (b) the holon–spinon particle $(-\frac{1}{2}, -\frac{1}{2})$, (c) the antiholon–spinon hole $(\frac{1}{2}, \frac{1}{2})$ and (d) the holon–spinon hole $(-\frac{1}{2}, \frac{1}{2})$. Analogous to previous discussion, we obtain the following results of the excitation spectra

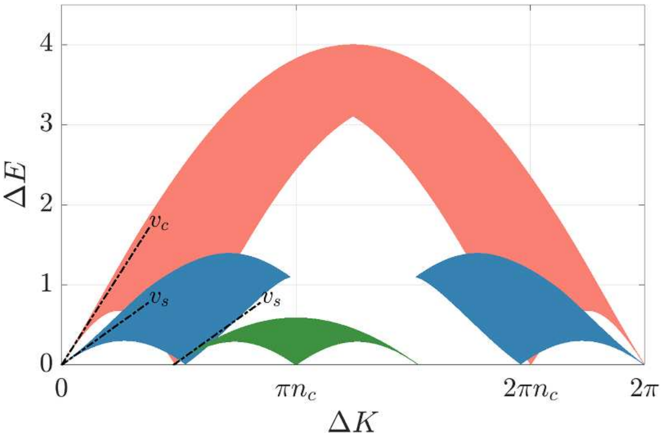

Figure 7. The shaded area in orange represents a particle–hole excitation of charge. The blue shaded area denotes spin particle–hole excitation. The green colour denotes the two-spinon excitation, the same as figure 6. This reveals subtle separation of spin and charge excitations in the presence of a magnetic field. The parameter corresponds to the red star in figure 1.

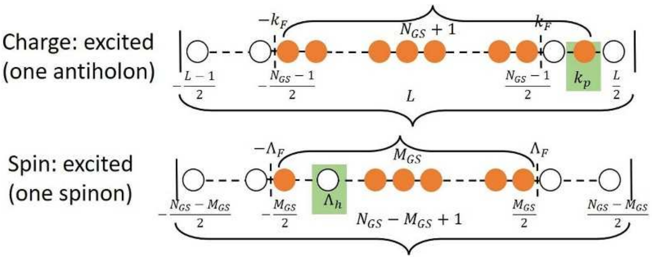

Figure 8. The antiholon–spinon hole excitations.

$$
\begin{aligned}
&(a)\begin{cases} E_{\bar{h}\bar{s}} = \kappa\left(k_p\right) + \varepsilon_1\left(\Lambda_p\right) \\ P_{\bar{h}\bar{s}} = p\left(k_p\right) + p_1\left(\Lambda_p\right) + \pi n_c \end{cases} \\
&(b)\begin{cases} E_{h\bar{s}} = -\kappa\left(k_h\right) + \varepsilon_1\left(\Lambda_p\right) \\ P_{h\bar{s}} = -p\left(k_h\right) + p_1\left(\Lambda_p\right) \end{cases}, \\
&(c)\begin{cases} E_{\bar{h}s} = \kappa\left(k_p\right) - \varepsilon_1\left(\Lambda_h\right) \\ P_{\bar{h}s} = p\left(k_p\right) - p_1\left(\Lambda_h\right) \end{cases}, \\
&(d)\begin{cases} E_{hs} = -\kappa\left(k_h\right) - \varepsilon_1\left(\Lambda_h\right) \\ P_{hs} = -p\left(k_h\right) - p_1\left(\Lambda_h\right) + \pi n_c \end{cases}.
\end{aligned} \tag{30}
$$

As a result of the above discussion, these four excitation patterns can be converted to each other through certain numbers of particle–hole excitations. Their continuum spectra are depicted in figure 9. Comparing the upper (low spin-down density) and lower (near half-filled) panels of the figure 9, we observe that the cases in (a), (c) and (d), which are related to the antiholon excitations in the charge sector or spinon hole

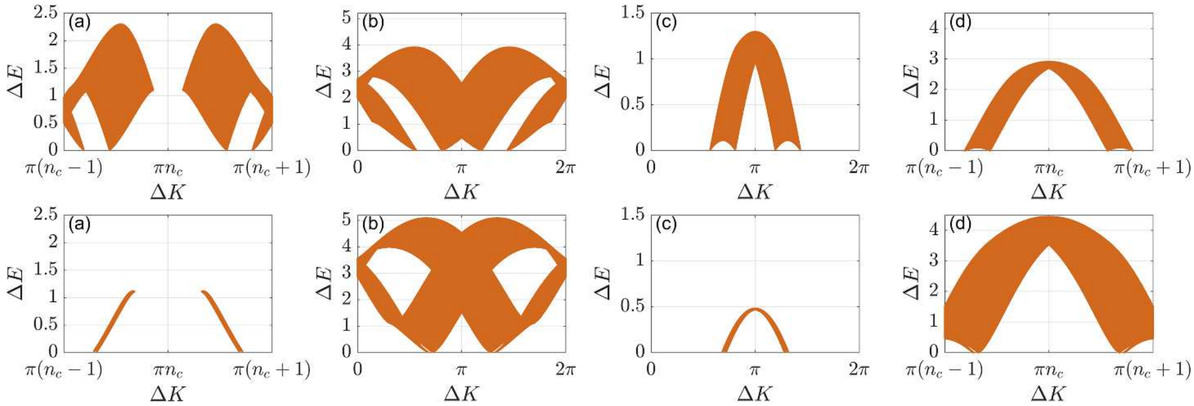

Figure 9. Fractional holon and spinon excitations: from left to right (a) antiholon–spinon particle excitation $(\frac{1}{2},-\frac{1}{2})$, (b) holon–spinon particle excitation $(-\frac{1}{2},-\frac{1}{2})$, (c) antiholon–spinon hole excitation $(\frac{1}{2},\frac{1}{2})$ and (d) holon–spinon hole excitation $(-\frac{1}{2},\frac{1}{2})$. Upper panel: excitation spectra in the low spin-down density area with $n_c=0.6859, n_\downarrow=0.1207$, corresponding to the orange square in figure 1; lower panel: excitation spectra near half-filled states with density $n_c=0.9775, n_\downarrow=0.298$, corresponding to the orange diamond in figure 1. In each panel, the excitation bands in (a) and (d) are centred around the πn_c, whereas the excitation bands in (b) and (c) are centred around π.

excitations in the spin part, are significantly affected by the filling and magnetization. When the charge sector approaches a gapped phase, see figures 9(a) and (c), the energy range of the antiholon becomes narrow, causing the excitations to display single-particle behaviour. This excitation mode is studied in terms of a spin–charge scattering state, rather than a spin–charge separation state in collective excitations in figure 6.

In general, we observe that the gapless excitations occur only at a sufficiently small energy scale. The charge and spin excitations are well decoupled only in certain configurations, as demonstrated in figures 6 and 7. This spin–charge separation phenomenon is unique in 1D strongly correlated electron systems and can be described by the spin-coherent and spin-incoherent TLL theory. Based on the above illustrations of excitations of spin and charge, we will further study the spin-coherent and spin-incoherent TLLs in the 1D Hubbard model below. In the supplementary material[7], some gapped excitations such as $k-\Lambda$ strings and Λ strings, are presented for completeness.

3. Universal thermodynamics and quantum criticality

The 1D Hubbard model yields profound many-body physics at zero and finite temperatures. It exhibits rich quantum phases and universal thermodynamics when the temperature is much lower than the Fermi energy. A comprehensive understanding of the universal low-temperature behaviour, however, remains challenging due to the complexity of the Bethe ansatz equations and its $N!$-many terms of the wave function. Because of the complexity and intricacy of spin and charge root string patterns in the Bethe ansatz equations and the TBA equations [22], most studies on the thermal and magnetic properties of the 1D Hubbard model have been carried out only at zero temperature with half-filled states [20, 22] or at a zero magnetic field [112, 113]. Even in the low-temperature regime, there is no well-established understanding of universal behaviour, such as TLL, SILL and quantum scaling functions. Likely, this can be resorted to numerical simulation by iterative means [5, 36, 38, 114, 115]. However, the analytical results of the TLL and quantum criticality are still elusive. In this section, firstly, we will present our analytical and numerical studies of universal thermodynamics and quantum criticality of the 1D Hubbard model using the TBA equations near the quadruple critical point, the region marked by the white empty circle in figure 1. In this regime, the model is rarely studied due to the coupling of the two degrees of freedom. And this regime involves four phases of states that manifest the transitions of three important states: only spin degrees of freedom in phase V, only charge degrees of freedom in phase III and spin–charge coexisting in phase IV. More importantly, we will give general scaling laws at an arbitrary magnetic field and chemical potential. Then, from the perspective of quantum phase transitions, we recognize the emergence of SILL, which is less understood from the perspective of Bethe ansatz. Finally, we will study interaction-driven quantum phase transition. This is an aspect with little-known analytical results. We will establish relationships between the two phase transitions driven by external potentials and internal degrees of freedom like interaction. Our work completes the analytical study of universality of phase transitions with a generality.

Here, for clarity, we summarize our main results of section 3 in table 1, and the calculation details are presented in sections 3.1, 3.2 and 3.3 as well as the supplementary material[7].

3.1. Thermodynamic quantities in the ground state and low-temperature regime

3.1.1. Dimensionless ratios and phase diagram. In this part, we study the dimensionless ratios and their application in the 1D Hubbard model. Before doing so, let us first give

Table 1. Universal properties of the 1D Hubbard model.

Properties Phases	II	IV	V	III
Wilson ratios $R_w^{\chi_s}$ equation (32)	2	$4(v_cK_s+v_sK_{sc})/(v_s+v_c)$	$8K_s$	0
Free energies f	$f_0-(\pi T^2)/(6v_c)$ equation (34)	$f_0-(\pi T^2)\left(1/v_c+1/v_s\right)/6$ equations (33) and (40)	$f_0-(\pi T^2)/(6v_s)$ equation (35)	$-\mu-u-B+g_{\frac{3}{2}}T^{\frac{3}{2}}+g_2T^2+g_{\frac{5}{2}}T^{\frac{5}{2}}$ equation (36)
Magnetic properties	χ_c,χ_s: equation (43)	χ_c: equations (52) and (57) χ_s: equations (53) and (58)	χ_c: equation (46) χ_s: equation (47)	χ_c,χ_s: 0 χ_c,χ_s: 0
External-potential-driven scaling laws	near quadruple point: equations (82), (86), (90)–(95) and (103)–(108) general: equations (114)–(118)			
SILL	thermodynamics: equation (129) correlation functions: equations (133)–(137)		\	\
Contact and contact susceptibilities	\	IV-V: equations (144)–(147)		\
Interaction-driven scaling laws	IV–V: equations (168)–(170) and (179); II–IV: equations (174) and (178) general: equations (175)–(177)			

a brief view of the ground-state phase diagram determined by equations (18) and (19). In the limit of zero temperature, the dressed energies $\kappa(k)$ and $\varepsilon_1(\Lambda)$ can be used to analyze the phase transitions and thermodynamic quantities. In the grand canonical ensemble, the magnetic field and chemical potential determine the integration boundaries Q, A through the conditions $\kappa(Q)=0, \varepsilon_1(A)=0$. The particle density $n_c=\int_{-Q}^{Q}\mathrm{d}k\rho(k)$ is also called the filling factor. Meanwhile, the spin-down electrons per site $n_\downarrow=\int_{-A}^{A}\mathrm{d}\Lambda\sigma_1(\Lambda)$ and the magnetization $m=n_c/2-n_\downarrow$ can be obtained from the root densities equations (20) and (21). The magnetic field and chemical potential drive the system from one phase to another at zero temperature.

Phase transitions usually occur under the following scenarios: a) vanishing dressed energy, i.e. $\kappa(0)=0$ or $\varepsilon_1(0)=0$, with one dressed energy to be zero at each transition; b) opening an energy gap. In the Hubbard model, the phase transition occurs if one degree of freedom starts to make a difference or disappears with another degree of freedom unchanged, leading to coupling or decoupling in these degrees. In the presence of an energy gap, i.e. the charge dressed energy $\kappa(\pi)\leqslant 0$ in part, the charge sector thus displays insulation behaviour, leading to the phase transition from metal to insulator. Both these cases induce significant quantum fluctuation in the system.

Using these conditions [22, 116], we may give five phases of states displayed in figure 1: (I) vacuum with $Q=0, A=0$ or $n_c=m=0$; (II) partially filled and spin fully polarized state with $0<Q<\pi, A=0$ or $0<n_c<1, m=n_c/2$ with the boundary conditions given by $Q=0$ and $Q=\pi$; (III) half-filled and spin fully polarized state with $Q=\pi, A=0$ or $n_c=1, m=1/2$; (IV) partially filled and magnetized band with $0<Q<\pi, 0<A\leqslant\infty$ or $0<n_c<1, 0\leqslant m<n_c/2$; the phase boundary between phase (II) and (IV) is given by $\kappa(0)<0<\kappa(\pi)$, $\varepsilon_1(0)=0$; (V) half-filled, magnetized band, also referred to as the Mott insulator with $Q=\pi, 0<A\leqslant\infty$ or $n_c=1, 0\leqslant m<n_c/2$, and the phase boundary between (V) and (IV) is given by $\kappa(\pi)=0, \varepsilon_1(0)<0$. By substituting each of the phase boundary conditions into the dressed energy equations (18) and (19), we can analytically determine all the critical fields in the $B-\mu$ plane: also, see [22]. In fact, thermal properties feature dramatic quantum fluctuations around a quantum critical point (QCP), whereas the dimensionless ratios, the ratios between the fluctuations of two types of sources, can become comparable to temperature: for instance, the susceptibility Wilson ratio $R_{\mathrm{W}}^{\chi_s}$ [117] and the compressibility Wilson ratio $R_{\mathrm{W}}^{\chi_c}$ [118, 119]

$$R_{\mathrm{W}}^{\chi_s}=\frac{4}{3}\left(\frac{\pi k_B}{\mu_B g}\right)^2\frac{\chi_s}{C_v/T},\qquad R_{\mathrm{W}}^{\chi_c}=\frac{\pi^2k_B^2}{3}\frac{\chi_c}{C_v/T},\tag{31}$$

describing the competition between magnetic fluctuation or particle number fluctuation and thermal fluctuations, respectively. In the above expressions, χ_s (χ_c) are the magnetic susceptibility (compressibility), respectively. In the TLL phase, these ratios become constants, independently of temperature. Therefore the ground state phase diagram can be characterized by the dimensionless ratios.

A significant aspect of these ratios is their characterization of the TLL and their scaling behaviour near critical points [101, 118–120]. In figure 10(a), we present the 3D plot of the magnetic Wilson ratio in the $B-\mu-R_{\mathrm{W}}^{\chi_s}$ parameter space, while in figure 10(b), we show the Wilson ratio as a function of μ for a fixed B. It is remarkable that the magnetic

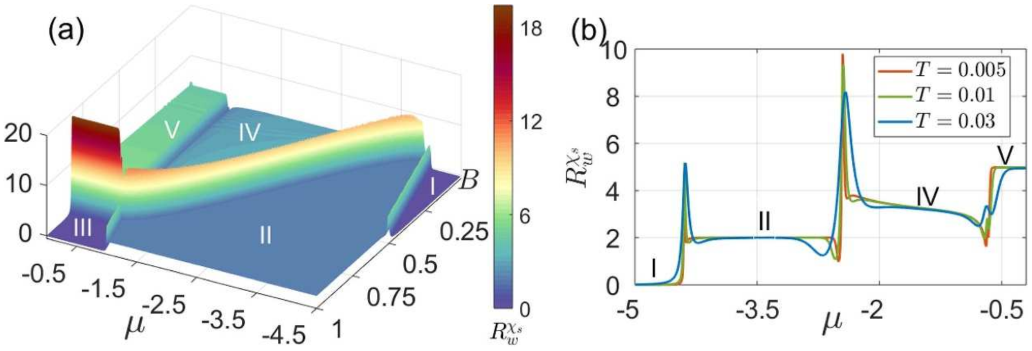

Figure 10. (a) The 3D plot of the Wilson ratio $R_{\mathrm{w}}^{\chi_s}$ maps out the phase diagram of the 1D Hubbard model at low temperatures, which significantly marks different phases of states. The parameter setting reads: $T = 0.005$ and $u = 1$. (b) A plot of the Wilson ratio $R_{\mathrm{w}}^{\chi_s}$ at fixed $B = 0.4, u = 1$. As the chemical potential changes, four phases (I, II, IV and V) can be reached, indicated by sudden enhancements of the Wilson ratio.

Wilson ratio is suddenly enhanced near the QCP, elegantly distinguishing different phases. Moreover, in terms of the transport and thermodynamic results of the magnetic susceptibility, specific heat, Luttinger parameters and velocities, the Wilson ratios are given by (detailed analysis will be given in our prepared article [121])

$$\begin{aligned} \text{II:}\quad & R_{\mathrm{w}}^{\chi_s} \approx 2, \\ \text{IV:}\quad & R_{\mathrm{w}}^{\chi_s} \approx 4\left(v_c K_s + v_s K_{sc}\right)/\left(v_s + v_c\right), \\ \text{V:}\quad & R_{\mathrm{w}}^{\chi_s} \approx 8K_s, \\ \text{I and III:}\quad & R_{\mathrm{w}}^{\chi_s} = 0, \end{aligned} \tag{32}$$

where K_s is the Luttinger parameter for spin, K_{sc} is the cross Luttinger parameter [121] and $v_{c,s}$ are sound velocities for charge and spin, respectively. These relations, equation (32), are in excellent agreement with the numerical results shown in figure 10. Such dimensionless ratios also display universal scaling behaviour near phase transitions.

From the above analysis, one can easily determine the five quantum phases of the ground state of the 1D repulsive Hubbard model. Among these, phase IV shows the richest physics, i.e. the charge and spin degrees of freedom coexist and dramatically make up the phase of spin–charge-separated TLLs [47–49], showing non-Fermi liquid behaviour in one dimension. In the TLL phase, all quasiparticles form collective motions and thus decouple into two propagating modes with different velocities, v_c, v_s [51, 53, 60], which rely on the value of the coupling and can be effectively estimated from TBA equations. The spin–charge separation phenomenon can also be observed from their excitation spectra, see the discussion in section 2. In the supplementary material[7], we show that phase IV can be seen as two-component free fluids characterized by the additivity rule of free energy at the low-energy level, while phases II and V are representatives of the single TLL, namely,

$$f = f_0 - \frac{\pi T^2}{6}\left(\frac{1}{v_c} + \frac{1}{v_s}\right), \quad \text{for phase IV}, \tag{33}$$

$$f = f_0 - \frac{\pi T^2}{6}\frac{1}{v_c}, \quad \text{for phase II}, \tag{34}$$

$$f = f_0 - \frac{\pi T^2}{6}\frac{1}{v_s}, \quad \text{for phase V}, \tag{35}$$

where v_c and v_s are defined through $v_c = \kappa'(Q)/(2\pi\rho(Q))$ and $v_s = \varepsilon_1{}'(A)/(2\pi\sigma_1(A))$ with cut-off points Q, A, respectively. The relation between the free energy and velocity gives a universal nature shared by a large family of systems [57, 101, 122]. Taking the second derivative of the free energy with respect to temperature, specific heat is directly derived $C_v = \pi T/3\left(1/v_c + 1/v_s\right), C_v = \pi T/(3v_c), C_v = \pi T/(3v_s)$ for IV, II and V, respectively. The above results in equations (33)–(35) provide the universal leading order correction of the temperature at low energy of interacting many-body systems, i.e. characteristic of thermodynamics in the TLLs.

3.1.2. Contributions from $k - \Lambda$ string in phase III. In the low-temperature limit $\mu, B > T$, the low-energy behaviour of the system is immune to the gapped string excitations when the states are away from the QCPs in figure 10. By analysing the TBA equations (14)–(16), we observe that it is reasonable to ignore the gapped string states and retain only the gapless string states in both Λ and $k - \Lambda$ strings at low energy. The driving terms in these equations significantly determine the contributions to the low-energy states. The length-n Λ strings and $k - \Lambda$ string make less contribution to the low-energy states when n is larger. Here, we just calculate the contributions from the length-1 Λ and $k - \Lambda$ strings in phase III in which both are gapped. The TBA equations suggest that the greater the value of the chemical potential μ and magnetic field B relative to the temperature T, the smaller the contributions of the $k - \Lambda$ and Λ strings. In phase III, the absolute value of the chemical potential is small, while the magnetic field B is large. Therefore, without losing generality, here we consider the length-1 $k - \Lambda$ and Λ strings at low temperature $|\mu| \sim T$ and $B > T$ in phase III. After tedious iterations on free energy, see the supplementary material[7], we obtain a close form of the free energy

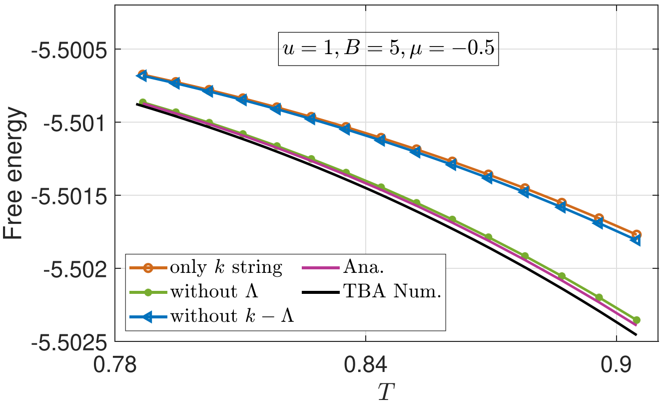

Figure 11. The free energy for gapped length-1 Λ and $k-\Lambda$ strings in phase III. The black and purple solid curves denote the numerical results and analytical results, equation (36), of the free energy, respectively. The red empty-circle–solid line only denotes the contribution from the charge k degrees of freedom, showing a large discrepancy from the solid lines. The green filled-circle–solid line denotes the free energy without Λ strings, showing a little difference from the solid lines. The blue triangular–solid line denotes the free energy without $k-\Lambda$ strings. Thus, the Λ string contribution is negligible in phase III.

$$f = -\mu - u - B + g_{\frac{3}{2}} T^{\frac{3}{2}} + g_2 T^2 + g_{\frac{5}{2}} T^{\frac{5}{2}} + O\left(T^3, \mathrm{e}^{-\frac{4B}{T}}, \mathrm{e}^{\frac{4\mu}{T}}\right), \quad \text{for phase III} \tag{36}$$

where the coefficients are explicitly given by

$$\begin{aligned} g_{\frac{3}{2}} &= -\frac{\lambda_1 \pi^{\frac{1}{2}}}{\eta_1^{\frac{1}{2}}} \mathrm{e}^{-\frac{2B+\eta_0}{T}} + \frac{f_{\frac{1}{2}}}{2\pi^{\frac{1}{2}}} \mathrm{e}^{\frac{2\mu}{T}} + \frac{f_{\frac{3}{2}}}{2\pi^{\frac{1}{2}}}, \\ g_2 &= -\left(\frac{\lambda_1 f_{\frac{3}{2}}}{\eta_1^{\frac{1}{2}} u} + \frac{f_{\frac{1}{2}}}{2\eta_1^{\frac{1}{2}} \pi u}\right) \mathrm{e}^{-\frac{2B+\eta_0}{T}} + \frac{f_{\frac{1}{2}} f_{\frac{3}{2}}}{4\pi u} \mathrm{e}^{\frac{2\mu}{T}}, \\ g_{\frac{5}{2}} &= -\left(\frac{\lambda_1 f^2{}_{\frac{3}{2}}}{2\eta_1^{\frac{1}{2}} \pi^{\frac{1}{2}} u^2} + \frac{\lambda_2 \pi^{\frac{1}{2}}}{4\eta_1^{\frac{3}{2}}} + \frac{f_{\frac{1}{2}} f_{\frac{3}{2}}}{2\eta_1^{\frac{1}{2}} \pi^{\frac{3}{2}} u^2}\right) \mathrm{e}^{-\frac{2B+\eta_0}{T}} \\ &\quad + \left(\frac{3 f_{\frac{1}{2}} f^2{}_{\frac{3}{2}}}{32\pi^{\frac{3}{2}} u^2} + \frac{f_{\frac{3}{2}}}{32\pi^{\frac{1}{2}}}\right) \mathrm{e}^{\frac{2\mu}{T}} + \frac{f_{\frac{5}{2}}}{32\pi^{\frac{1}{2}}}, \end{aligned} \tag{37}$$

where we denote the function $f_n = \mathrm{Li}_n(-\mathrm{e}^{\frac{2-\mu-2u-B}{T}})$, and the parameters $\lambda_1 = \frac{1}{\pi\sqrt{1+u^2}}$, $\lambda_2 = \frac{1-2u^2}{\pi(1+u^2)^{5/2}}$, $\eta_0 = 4(u - \sqrt{1+u^2})$ and $\eta_1 = \frac{2}{(1+u^2)^{3/2}}$. By analysing equation (37), we observe that in the functions $g_{\frac{3}{2}, 2, \frac{5}{2}}$, the terms involving the exponents $\mathrm{e}^{-\frac{2B+\eta_0}{T}}$ and $\mathrm{e}^{\frac{2\mu}{T}}$ come from gapped length-1 Λ and $k-\Lambda$ strings, respectively; meanwhile, the terms that do not contain any exponential terms stem from the contributions of gapless charge k. In the above results, we have omitted the contributions from the strings with lengths more than length-2.

In figure 11, we observe that our analytic expression of the free energy is consistent with the numerical results obtained from the TBA equations (14)–(16). The contributions from the $k-\Lambda$ string are greater than those from the Λ strings due to the choice of parameters $B > T$ and $|\mu| \sim T$. Moreover, from the absolute value of the free energy, we observe that the order of the $k-\Lambda$ string contributions is $O(10^{-4})$ as the temperature tends to $T = 1$. In general, it can be safely ignored in the low-temperature behaviour. In phase III, the contributions from the gapped Λ strings are very small and negligible too. But the length-1 Λ string plays an important role in phases IV and V. More detailed calculations of the free energy for phase III are given in the supplementary material[7].

3.1.3. Magnetic properties at zero temperature near the quadruple critical point.

The magnetic properties of the 1D Hubbard model at zero temperature provide a benchmark for understanding universal low-energy physics. However, most studies in the literature have been carried out in a vanishing magnetic field or half-filled band [20, 22, 112, 113]. To obtain useful analytical results of the magnetic properties of the model, here, we try to analytically calculate the magnetic properties under the conditions of high density (the Fermi point Q tends to π) and high magnetization limits (the Fermi point A tends to 0), namely, the region marked by the white empty circle in figure 1, serving as a pivot which relates four quantum phases. Around the quadruple point, we may conceive the properties of charge only, spin only and spin–charge coexistence. The physics in this region has not been well studied in the literature.

The main objective is to obtain thermodynamic quantities in terms of small parameters $\delta = \pi - Q \ll 1$ and $A \ll 1$. After some lengthy calculations, see the supplementary material[7], the expressions of charge and spin dressed energies and density equations can be written in terms of the orders of δ and A

$$\kappa(k) = \bar{\delta} \boldsymbol{M_c} \bar{A}^T, \varepsilon_1(\Lambda) = \bar{\delta} \boldsymbol{M_s} \bar{A}^T, \tag{38}$$

$$\rho(k) = \bar{\delta} \boldsymbol{M_{dc}} \bar{A}^T, \sigma_1(\Lambda) = \bar{\delta} \boldsymbol{M_{ds}} \bar{A}^T, \tag{39}$$

where $\bar{\delta} = (\delta^0, \delta^1, \delta^2, \delta^3)$, $\bar{A} = (A^0, A^1, A^2, A^3)$, the superscript T denotes transpose and $\boldsymbol{M_c}, \boldsymbol{M_s}, \boldsymbol{M_{dc}}, \boldsymbol{M_{ds}}$ are four matrices given in the supplementary material[7]. By analysing the construction of these four matrices and using the free energy, equation (17) with $T = 0$, we may obtain

$$f = -\mu - u - B - \frac{8\lambda_1}{3(1+u^2)^{\frac{3}{2}}} A^3 - \frac{2}{3\pi} \delta^3 \tag{40}$$

with λ_1 given in the supplementary material[7]. On the other hand, in terms of the discrete symmetries of the repulsive Hubbard model [22], the free energy of the repulsive system can be transformed to that of the attractive case via the relation $f_{\mathrm{r}}(\mu, B, T, u) = f_{\mathrm{a}}(-B, -\mu, T, -u) - \mu - B$, where the subscript $a(r)$ means attractive (repulsive) interaction. It turns out that the results obtained in this part not only cover that of the attractive model in the low-density and strong coupling limits [101], but are also valid for the arbitrary interaction strength away from the strong coupling limit.

In general, it is straightforward to show that there is a one-to-one correspondence from the high-density area in the repulsive case to the low-density regime in the attractive case

[101]. Taking the derivative of free energy, one can obtain the relationship between their thermodynamic quantities:

$$\frac{\partial f_{\mathrm{r}}}{\partial \mu} = -\frac{\partial f_{\mathrm{a}}}{\partial B} - 1 \longrightarrow n_{r,\mu} = 1 - 2m_{a,B}, \tag{41}$$

$$\frac{\partial f_{\mathrm{r}}}{\partial B} = -\frac{\partial f_{\mathrm{a}}}{\partial \mu} - 1 \longrightarrow 2m_{r,B} = 1 - n_{a,\mu}. \tag{42}$$

Based on equations (38) and (39), we are able to obtain the first and second order of derivative thermodynamic quantities, such as the particle number n_c, spin-down number $n_\downarrow$, velocities v_c, v_s, specific heat C_v, and the charge and spin susceptibilities $\chi_c = \frac{\partial n_c}{\partial \mu}|_{B(m)}, \chi_s = \frac{\partial m}{\partial B}|_{\mu(n_c)}$ with $m = \frac{n_c}{2} - n_\downarrow$. The calculation details are relegated to the supplementary material[7].

We would also like to remark that the above results we obtained can be applied to phase II and the Mott phase V; see the region marked by the white empty circle in figure 1. Explicitly, we present our key results in the grand canonical ensemble

phase II:

$$n_c = 1 - \frac{\delta}{\pi}, n_\downarrow = 0, \chi_c = \frac{1}{2\pi\delta}, \chi_s = \frac{1}{4\pi\delta}, v_c = 2\delta - \frac{1}{3}\delta^3,$$
$$C_v = \frac{\pi T}{3}\frac{1}{v_c}, \tag{43}$$

phase V:

$$n_c = 1, \tag{44}$$

$$n_\downarrow = 2\left[\lambda_1 A - \frac{\lambda_1}{\pi u}A^2 + A^3\left(\frac{\lambda_1}{\pi^2 u^2} + \frac{\lambda_2}{6}\right)\right], \tag{45}$$

$$\chi_c = 0, \tag{46}$$

$$\chi_s = \left[2\lambda_1\left(1 - \frac{2}{\pi u}A + \frac{3}{\pi^2 u^2}A^2\right) + \lambda_2 A^2\right]\frac{1}{\eta_1 A\left(1 + \frac{A}{\pi u}\right)}, \tag{47}$$

$$v_s = \frac{\eta_1 A + \frac{\eta_2}{12}A^3}{\pi\left(\lambda_1 + \frac{\lambda_2}{2}A^2 - \frac{\lambda_1}{\pi u}A + \frac{\lambda_1}{3\pi u^3}A^3 + \frac{\lambda_1}{\pi^2 u^2}A^2 - \frac{\lambda_1}{\pi^3 u^3}A^3 - \frac{\lambda_2}{6\pi u}A^3\right)}, \tag{48}$$

$$C_v = \frac{\pi T}{3}\frac{1}{v_s}, \tag{49}$$

phase IV:

$$n_c = 1 - 2\delta\left(\frac{1}{2\pi} - \frac{2\lambda_1}{\pi u}A + \frac{2\lambda_1}{\pi^2 u^2}A^2\right) - \frac{4}{\pi^3 u^2}\delta^2 A, \tag{50}$$

$$n_\downarrow = 2\left[A\left(\lambda_1 - \frac{2}{\pi u}\delta\left(\frac{1}{2\pi} - \frac{2\lambda_1}{\pi u}A\right)\right) - A^2\frac{1}{\pi u}\left(\lambda_1 - \frac{1}{\pi^2 u}\delta\right) + A^3\left(\frac{\lambda_1}{\pi^2 u^2} + \frac{\lambda_2}{6}\right)\right], \tag{51}$$

$$\chi_c = \frac{\partial n}{\partial \mu}|_B = \left(-\frac{1}{\pi} + \frac{4\lambda_1}{\pi u}A - \frac{4\lambda_1}{\pi^2 u^2}A^2 - \frac{8}{\pi^3 u^2}\delta A\right)\frac{\partial \delta}{\partial \mu} + \left(\frac{4\lambda_1}{\pi u}\delta - \frac{8\lambda_1}{\pi^2 u^2}\delta A - \frac{4}{\pi^3 u^2}\delta^2\right)\frac{\partial A}{\partial \mu} = \chi_c^{(1)} + \chi_c^{(2)}, \tag{52}$$

$$\chi_s = \frac{\partial m}{\partial B}|_\mu = \left[-\frac{1}{2\pi} - \frac{4}{\pi^3 u^2}\delta A + \frac{2}{\pi^2 u}(1 + \pi\lambda_1)A - \frac{2}{\pi^3 u^2}(1 + 5\pi\lambda_1)A^2\right]\frac{\partial \delta}{\partial B}$$
$$+ \left[-2\lambda_1\left(1 - \frac{2}{\pi u}A + \frac{3}{\pi^2 u^2}A^2\right) - \frac{2}{\pi^3 u^2}\delta^2 + \frac{2}{\pi^2 u}(1 + \pi\lambda_1)\delta - \frac{4}{\pi^3 u^2}(1 + 5\pi\lambda_1)\delta A - \lambda_2 A^2\right]\frac{\partial A}{\partial B}$$
$$= \chi_s^{(1)} + \chi_s^{(2)}, \tag{53}$$

$$v_c = \frac{2\delta - \frac{1}{3}\delta^3}{2\pi\left(\frac{1}{2\pi} - \frac{2\lambda_1}{\pi u}A + \frac{2\lambda_1}{\pi^2 u^2}A^2 - \frac{2\lambda_1}{\pi^3 u^3}A^3 + \frac{2\lambda_1}{\pi u^3}\delta^2 A + \frac{2\lambda_1}{3\pi u^3}A^3 - \frac{\lambda_2}{3\pi u}A^3 + \frac{\lambda_1}{\pi u}\delta^2 A + \frac{2}{\pi^3 u^2}\delta A - \frac{2}{\pi^4 u^3}(1 + 4\pi\lambda_1)\delta A^2\right)}, \tag{54}$$

$$v_s = \frac{2\eta_1 A + \frac{\eta_2}{6}A^3}{2\pi\left(\lambda_1 + \frac{\lambda_2}{2}A^2 - \frac{1}{\pi^2 u}\delta + \frac{4\lambda_1}{\pi^2 u^2}\delta A - \frac{8\lambda_1}{\pi^3 u^3}\delta A^2 + \frac{1}{\pi^2 u^3}\delta A^2 - \frac{4}{\pi^4 u^3}\delta^2 A + \frac{1}{3\pi^2 u^3}\delta^3 - \frac{\lambda_1}{\pi u}A + \frac{1}{\pi^3 u^2}\delta A + \frac{\lambda_1}{3\pi u^3}A^3 + \frac{\lambda_1}{\pi^2 u^2}A^2 - \frac{1}{\pi^4 u^3}\delta A^2 - \frac{\lambda_1}{\pi^3 u^3}A^3 - \frac{\lambda_2}{6\pi u}A^3\right)}, \tag{55}$$

$$C_v = \frac{\pi T}{3}\left(\frac{1}{v_c} + \frac{1}{v_s}\right), \tag{56}$$

where $\lambda_1, \lambda_2, \eta_1, \eta_2, \frac{\partial \delta}{\partial \mu}, \frac{\partial A}{\partial \mu}, \frac{\partial \delta}{\partial B}$ and $\frac{\partial A}{\partial B}$ are given in the supplementary material[7].

In the grand canonical ensemble, we observe that the charge susceptibilities $\chi_c^{(1)}, \chi_c^{(2)}$ (the spin susceptibility $\chi_s^{(1)}, \chi_s^{(2)}$) constitute two parts of the contributions from different resources δ and A, respectively; see equations (52) and (53). The susceptibilities can be split into two parts, which are reminiscent of the additivity rules found in the Fulde-Ferrell-Larkin-Ovchinnikov (FFLO) state of attractive situations [101]. We also observe that the decomposition terms stem from two sources, i.e. the changes in charge and spin with respect to the chemical potential and magnetic field. We further confirm our analytical result equations (43)–(56) in figure 12 via numerical calculation. The analytical results and numerical simulation of sound velocities and thermodynamic properties from the solution of the TBA equations are shown in figure 12(a). We observe that v_c approaches zero at the critical point for the phase transition from magnetized phase IV to the Mott phase V. On the other hand, v_s goes to zero, which signifies an approach to the spin fully polarized phase II. Thus, the velocities can serve as a signature of quantum phase transitions. In figure 12(b), we show the specific heat in terms of velocities at various temperatures, demonstrating good agreement between our numerical calculation and analytical results. The quantity C_v/T becomes temperature-independent for the TLL states. We plot the magnetic susceptibility in figure 12(c) and observe that the susceptibility does not depend on temperature in the TLL regime, but becomes divergent in the vicinities of the critical points.

In the canonical ensemble with fixed density and magnetization, we obtain the charge and spin susceptibilities in terms of n_c, m

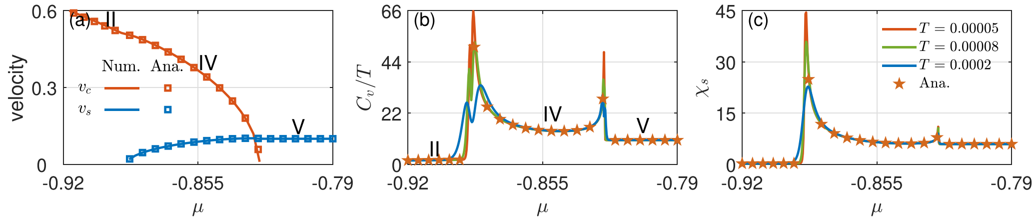

Figure 12. (a) Spin and charge velocities as a function of the chemical potential in phases II, IV and V, in which the analytical results are given by equations (54) and (55) for IV, equation (43) for II and equation (48) for V, respectively. (b) The analytical and numerical results of the specific heat in terms of the chemical potential. The curves of C_v/T at different temperatures collapse to a single curve of the analytical results in each phase. (c) The magnetic susceptibility: agreement between the numerical and analytical results, which are given by equations (43), (47) and (53). In the TLL phases, the susceptibility does not depend on temperature. The whole numerical setting reads $B = 0.825$, $u = 1$, situated within the white empty circle in figure 1.

$$\frac{1}{\chi_c} = \frac{\partial\mu}{\partial n_c}\bigg|_m = 2\delta\left(1-\frac{\delta}{\pi u}\right)\frac{\partial\delta}{\partial\hat{n}_c}\bigg|_m - \eta_1 A\left(1-\frac{3A}{\pi u}\right)\frac{\partial A}{\partial\hat{n}_c}\Big|_m$$
$$= \frac{1}{\chi_c^{(1)}}+\frac{1}{\chi_c^{(2)}}, \tag{57}$$
$$\frac{1}{\chi_s} = \frac{\partial B}{\partial m}\bigg|_{\hat{n}_c} = -\frac{2}{\pi u}\delta^2\frac{\partial\delta}{\partial m}\bigg|_{\hat{n}_c} - \eta_1 A\left(1+\frac{A}{\pi u}\right)\frac{\partial A}{\partial m}\Big|_{\hat{n}_c}$$
$$= \frac{1}{\chi_s^{(1)}}+\frac{1}{\chi_s^{(2)}}. \tag{58}$$

where $\frac{\partial\delta}{\partial\hat{n}_c}$, $\frac{\partial A}{\partial\hat{n}_c}$, $\frac{\partial\delta}{\partial m}$ and $\frac{\partial A}{\partial m}$ are given in the supplementary material[7]. In contrast to the the case for fixed external potentials, these formulas expose a reciprocal additivity relation at a fixed magnetization and density, see equations (57) and (58). The two ensembles are related to each other by the Jacobian determinant evaluated by the total differential of μ, B with respect to n, m. Apart from the numerical arithmetic and approximation method, as we have conducted above, we would like to discuss the dressed-charge matrix Z [22, 34, 35]

$$\mathrm{Z} = \begin{pmatrix} \xi_{cc}(Q) & \xi_{cs}(A) \\ \xi_{sc}(Q) & \xi_{ss}(A) \end{pmatrix}, \tag{59}$$

whose elements are determined by

$$\xi_{ab}(x_b) = \delta_{ab} + \sum_d \int_{-X_d}^{X_d} \mathrm{d}x_d \xi_{ad}(x_d) K_{db}(x_d, x_b). \tag{60}$$

Here, the kernels are given by

$$\begin{aligned} &K_{cc}(x_c, y_c) = 0, \\ &K_{sc}(x_c, x_s) = a_1(\sin(x_c) - x_s), \\ &K_{cs}(x_c, x_s) = \cos(x_c)\, a_1(\sin(x_c) - x_s), \\ &K_{ss}(x_s, y_s) = -a_2(x_s - y_s). \end{aligned} \tag{61}$$

These dressed charges can be used to calculate rigorous solutions for susceptibilities and conformal dimensions in asymptotics of correlation functions [34, 35], as well as spin and charge Drude weights [121]. We will discuss these studies further later.

One advantage of this method is that the iteration process is greatly simplified, both analytically and numerically. In the grand canonical ensemble, some exact relations are relevant to the dressed-charge matrix (59), for example [22],

$$\chi_c\bigg|_B = \frac{\partial n_c}{\partial\mu}\bigg|_B = \frac{\mathrm{Z}_{cc}^2}{\pi v_c} + \frac{\mathrm{Z}_{cs}^2}{\pi v_s} = \chi_c^{(1)} + \chi_c^{(2)}, \tag{62}$$
$$\chi_s\bigg|_\mu = \frac{\partial m}{\partial B}\bigg|_\mu = \frac{(\mathrm{Z}_{cc}-2\mathrm{Z}_{sc})^2}{2\pi v_c} + \frac{(\mathrm{Z}_{cs}-2\mathrm{Z}_{ss})^2}{2\pi v_s} = \chi_s^{(1)} + \chi_s^{(2)}. \tag{63}$$

Regarding the circumstances of variable changes, we can work out the Jacobian determinant from equations (62) and (63), namely, $J = 2(\mathrm{det}\mathrm{Z})^2/(\pi^2 v_c v_s)$. As a result, we obtain[8] for the canonical ensemble

$$\frac{1}{\chi_c}\bigg|_m = \frac{\partial\mu}{\partial n_c}\bigg|_m = \frac{\pi}{4}\frac{v_c(\mathrm{Z}_{cs}-2\mathrm{Z}_{ss})^2 + v_s(\mathrm{Z}_{cc}-2\mathrm{Z}_{sc})^2}{(\mathrm{det}\mathrm{Z})^2}$$
$$= \frac{1}{\chi_c^{(1)}} + \frac{1}{\chi_c^{(2)}}, \tag{64}$$
$$\frac{1}{\chi_s}\bigg|_{n_c} = \frac{\partial B}{\partial m}\bigg|_{n_c} = \frac{\pi}{2}\frac{v_c\mathrm{Z}_{cs}^2 + v_s\mathrm{Z}_{cc}^2}{(\mathrm{det}\mathrm{Z})^2} = \frac{1}{\chi_s^{(1)}} + \frac{1}{\chi_s^{(2)}}. \tag{65}$$

Comparing our analytical results, equations (52) and (53) (or equations (57) and (58)), with the dressed-charge formula, equations (62) and (63) (or equations (64) and (65)), we observe that the derivative term with respect to δ in equation (52) is equivalent to the first term associated with the charge velocity v_c in equation (62), whereas the derivative term with respect to A in equation (52) is equivalent to the second term associated with the spin velocity v_s in equation (62), respectively. Similar correspondences can be found from equations (53) and (63) in the grand canonical ensemble, as well as in equations (57) and (58), and (64) and (65), respectively.

Finally, we make a direct comparison between our analytical results and numerical results from the TBA equations. In

---

[8] The second equality in the equation (6.79) of the book [22] misses a factor of 2.

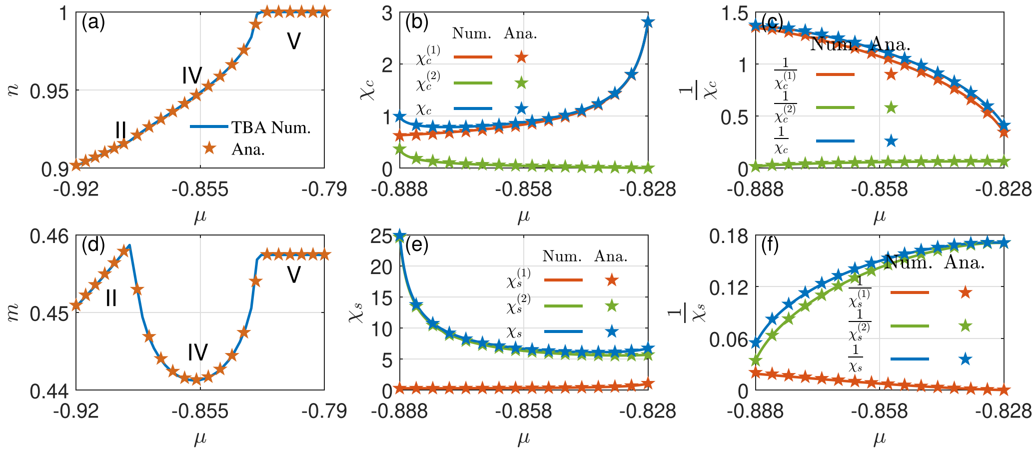

Figure 13. The charge density (a) and (d) magnetization vs the chemical potential in phases II, IV and V: agreement between the analytical results given by equation (43) for phase II, equations (50) and (51) for phase IV, equations (44) and (45) for phase V and the numerical calculations from the TBA equations. The compressibility (b) and susceptibility (e) in the grand canonical ensemble show agreement between the analytical results given by equations (52) and (53) and numerical simulations based on equations (62) and (63). Meanwhile, the compressibility (c) and susceptibility (f) in the canonical ensemble show agreement between the analytical results given by equations (57) and (58) and numerical simulations based on equations (64) and (65). The parameters of all the figures are situated within the white empty circle in figure 1.

figure 13, the first row shows density (a) and compressibility (b) in the grand canonical ensemble and (c) in the canonical ensemble. Whereas the second row shows the magnetization (d) and susceptibility (e) in the grand canonical ensemble and (f) in the canonical ensemble. The density and magnetization in figures 13(a) and (d) cross quantum phases from II, to IV and V as the chemical potential varies. In figures 13(b), (c), (e) and (f), we observe additivity rules in both the grand canonical and the canonical ensemble. All the analytical results agree well with the corresponding numerical results in this figure.

3.1.4. Quantum criticality near the quadruple critical point.

The results obtained in the previous sections present an elementary understanding of the ground-state properties and the behaviour of the TLLs. Although the criticality induced by the variation of external potentials, such as the magnetic field and chemical potential, has been extensively studied, most of the previous works only discuss a few examples, without systematically extracting universal laws. More importantly, the case for the interaction-driven quantum critical behaviour is still missing despite the fact that the interaction plays a central role in quantum many-body systems. This could be explained by the fact that the interaction strength is a parameter that cannot be tuned in typical solid-state materials. However, the tunability of the interaction strength through Feshbach resonance is one of the salient features of cold atoms. This motivates us to provide a detailed study of the interaction-driven criticality. Moreover, the quantum criticality of the Hubbard model near the quadruple critical point is elegantly accessible via analytical calculation.

In this section, we study quantum phase transitions and universal scaling functions of the properties of the 1D Hubbard model in terms of external fields. And in the last section, we focus on the interaction-driven quantum transitions. These two together complete the study of the universality of phase transitions in the model. From the phase diagram in figure 10, it can be observed that a phase transition occurs in the repulsive Hubbard model when certain degrees of freedom appear, disappear or become gapped. These changes induce significant quantum fluctuations. Although quantum phase transition occurs at zero temperature, thermal and quantum fluctuations can reach comparable levels in energy scales in the V-shaped critical regions at finite temperatures. A natural question is whether the quantum critical region has its own set of universal laws similar to the TLL. The obvious answer, of course, is that the quantum criticality for the same universality class of models is insensitive to the microscopic details of the systems and shares general and universal critical phenomena characterized by the critical exponents [123, 124]. For example, the universal scaling laws of magnetization and susceptibility satisfy [123, 124]

$$m = m_0 + T^{d/z+1-1/(\nu z)}\mathcal{O}_1\left[\frac{\mu-\mu_c}{T^{1/\nu z}}, \frac{B-B_c}{T^{1/\nu z}}, \frac{u-u_c}{T^{1/\nu z}}\right], \quad (66)$$

$$\chi_s = \chi_{s0} + T^{d/z+1-2/(\nu z)}\mathcal{O}_2\left[\frac{\mu-\mu_c}{T^{1/\nu z}}, \frac{B-B_c}{T^{1/\nu z}}, \frac{u-u_c}{T^{1/\nu z}}\right], \quad (67)$$

respectively. Here, m, χ_s represent the first and second orders of thermodynamic quantities, respectively, μ_c, B_c, u_c denote the critical fields at the critical point, and z, ν stand for the dynamical and the correlation critical exponent, respectively. The scaling functions, equations (66) and (67), consist of two parts: the first term denotes the background contributions stemming from the unchanged degrees of freedom, and the second term accounts for the singular part stemming from the sudden change in the density of states for the other degrees of freedom. One characteristic of quantum phase transition is that it displays universal scaling laws. Another salient feature of the critical region is that the characteristic length scale diverges, providing us with a feasible opportunity to capture system information by fractional exclusive statistics [123, 125–127].

Next, we embark on the analytical derivation of the singular behaviour of thermodynamic properties involving solely charge quasi-momenta k and length-1 Λ strings. There are five phase transitions in total—I–II, II–III, III–V, II–IV and IV–V—among which the latter four cases can be treated uniformly around the quadruple point.

I-II phase transition: Here, we first study the phase transition from an empty lattice phase I to partially filled phase II with the absence of down-spin. In this transition, the phase transition boundary is simply expressed as $2+2u+B_c+\mu_c=0$ with the subscripts B_c and μ_c standing for the critical fields. Thus, the charge dressed energy is given by $\kappa(k)=-2\cos k-\mu-2u-B$, showing free fermions on a 1D lattice. This gives the free energy $f=u+\frac{T^{3/2}}{2\pi^{1/2}}\mathrm{Li}_{\frac{3}{2}}(-\mathrm{e}^{\frac{\Delta B+\Delta\mu}{T}})$. Using fundamental thermodynamic relations, we directly obtain the first- and second-order thermodynamic quantities

$$m=\frac{n}{2}=-\frac{T^{\frac{1}{2}}}{4\pi^{\frac{1}{2}}}f_{\frac{1}{2}}, \tag{68}$$

$$\chi_s=\frac{\chi_c}{2}=-\frac{T^{-\frac{1}{2}}}{4\pi^{\frac{1}{2}}}f_{-\frac{1}{2}}, \tag{69}$$

$$\begin{aligned}\frac{c_v}{T}=&-\frac{3T^{-\frac{1}{2}}}{8\pi^{\frac{1}{2}}}f_{\frac{3}{2}}+\frac{T^{-\frac{3}{2}}\left(\Delta B+\Delta\mu\right)}{2\pi^{\frac{1}{2}}}f_{\frac{1}{2}}\\&-\frac{T^{-\frac{5}{2}}\left(\Delta B+\Delta\mu\right)^2}{2\pi^{\frac{1}{2}}}f_{-\frac{1}{2}}\end{aligned} \tag{70}$$

with $f_n=\mathrm{Li}_n(-\mathrm{e}^{\frac{\Delta B+\Delta\mu}{T}})$.

For the remaining four phase transitions, what we need to prepare before obtaining the scaling forms is to express the dressed energy equations and the free energy in terms of polylog functions. Under the assumption $n\to1, n_\downarrow\to0$, we expand the kernel function a_n around $k=\pi$ and $\Lambda=0$, and the coupled equations become

$$\begin{aligned}\kappa\left(k\right)=&-2\cos k+2\left(\frac{1}{\pi u^3}I_1-\frac{6}{\pi u^5}I_2\right)\sin^2 k\\&+\left(-\mu-2u-B-\frac{2}{\pi u}I_1+\frac{2}{\pi u^3}I_2\right)\\=&-2\cos k+2C_1\sin^2 k+C_2,\end{aligned} \tag{71}$$

$$\begin{aligned}\varepsilon_1\left(\Lambda\right)=&\Lambda^2\left(\eta_1+\frac{2J_1}{\pi u^3}-\frac{12J_2}{\pi u^5}-\frac{I_1}{4\pi u^3}+\frac{3I_2}{8\pi u^5}\right)\\&+\left(2B+4\left(u-\sqrt{1+u^2}\right)-\frac{2J_1}{\pi u}+\frac{2J_2}{\pi u^3}\right.\\&\left.+\frac{I_1}{\pi u}-\frac{I_2}{4\pi u^3}\right)\\=&D_1\Lambda^2+D_2,\end{aligned} \tag{72}$$

where the functions C_1, C_2, D_1, D_2 denote the corresponding coefficients

$$C_1=\frac{1}{\pi u^3}I_1-\frac{6}{\pi u^5}I_2, \tag{73}$$

$$C_2=-\mu-2u-B-\frac{2}{\pi u}I_1+\frac{2}{\pi u^3}I_2, \tag{74}$$

$$D_1=\eta_1+\frac{2J_1}{\pi u^3}-\frac{12J_2}{\pi u^5}-\frac{I_1}{4\pi u^3}+\frac{3I_2}{8\pi u^5}, \tag{75}$$

$$D_2=2B+4\left(u-\sqrt{1+u^2}\right)-\frac{2J_1}{\pi u}+\frac{2J_2}{\pi u^3}+\frac{I_1}{\pi u}-\frac{I_2}{4\pi u^3}. \tag{76}$$

Meanwhile, the integrals (I_1,I_2) and (J_1,J_2) are related to spin and charge degrees of freedom and make contributions only near the zero point. Integrating by parts, the formal solutions in terms of polylog functions read

$$I_1=\int_0^\infty \mathrm{d}\Lambda T\ \ln\left(1+\mathrm{e}^{-\frac{\varepsilon_1(\Lambda)}{T}}\right)=-\frac{T^{\frac{3}{2}}\pi^{\frac{1}{2}}}{2D_1^{\frac{1}{2}}}\mathrm{Li}_{\frac{3}{2}}\left(-\mathrm{e}^{\frac{-D_2}{T}}\right), \tag{77}$$

$$I_2=\int_0^\infty \mathrm{d}\Lambda\Lambda^2 T\ \ln\left(1+\mathrm{e}^{-\frac{\varepsilon_1(\Lambda)}{T}}\right)=-\frac{T^{\frac{5}{2}}\pi^{\frac{1}{2}}}{4D_1^{\frac{3}{2}}}\mathrm{Li}_{\frac{5}{2}}\left(-\mathrm{e}^{\frac{-D_2}{T}}\right), \tag{78}$$

$$\begin{aligned}J_1=&T\int_0^\pi \mathrm{d}k\cos k\ \ln\left(1+\mathrm{e}^{\frac{\kappa(k)}{T}}\right)\\=&\frac{T^{\frac{3}{2}}}{\sqrt{1-2C_1}}\Gamma\left(\frac{3}{2}\right)\mathrm{Li}_{\frac{3}{2}}\left(-\mathrm{e}^{\frac{2+C_2}{T}}\right)\\&-\frac{T^{\frac{5}{2}}}{8\left(1-2C_1\right)^{\frac{5}{2}}}\Gamma\left(\frac{5}{2}\right)\mathrm{Li}_{\frac{5}{2}}\left(-\mathrm{e}^{\frac{2+C_2}{T}}\right),\end{aligned} \tag{79}$$

$$\begin{aligned}J_2=&T\int_0^\pi \mathrm{d}k\cos k\sin^2 k\ \ln\left(1+\mathrm{e}^{\frac{\kappa(k)}{T}}\right)\\=&\frac{T^{\frac{5}{2}}}{3\left(1-2C_1\right)^{\frac{3}{2}}}\Gamma\left(\frac{5}{2}\right)\mathrm{Li}_{\frac{5}{2}}\left(-\mathrm{e}^{\frac{2+C_2}{T}}\right).\end{aligned} \tag{80}$$

With the help of the presentations of these four integrals, the Gibbs free energy is given by

$$f=-\mu-u-B-2\lambda_1 I_1-\lambda_2 I_2+\frac{1}{\pi}J_1+\frac{1}{2\pi}J_2. \tag{81}$$

Although we have greatly simplified the dressed equations, the four integrals (I_1,I_2) and (J_1,J_2) are still coupled to each other. These four quantities are intertwined and are needed to carefully distinguish the primary and secondary contributions according to the critical field conditions. Based on the above equations (71)–(80), we proceed to evaluate the critical behaviour from three aspects: critical fields, polylog functions and free energy. The polylog functions contain the sources of criticality, from which we can derive the scaling function of the free energy for the quantum critical region. For the part that causes criticality, we take expansions under the limit of $T\gg\Delta B$ or $T\gg\Delta\mu$. Here, we list our main results with details given in the supplementary material[7].

II–III phase transition: for the phase transition II-III, the critical field is determined by $2-2u-B_c-\mu_c=0$ and $\varepsilon_1(\Lambda)$ is gapped. The free energy is given by

$$f=-\mu-u-B+\frac{T^{\frac{3}{2}}}{2\pi^{\frac{1}{2}}}\mathrm{Li}_{\frac{3}{2}}\left(-\mathrm{e}^{\frac{-\Delta B-\Delta\mu}{T}}\right), \tag{82}$$

leading to the scattering forms of thermodynamics

$$m=\frac{n}{2}=\frac{1}{2}+\frac{T^{\frac{1}{2}}}{4\pi^{\frac{1}{2}}}f_{\frac{1}{2}}, \tag{83}$$

$$\chi_s=\frac{\chi_c}{2}=-\frac{T^{-\frac{1}{2}}}{4\pi^{\frac{1}{2}}}f_{-\frac{1}{2}}, \tag{84}$$

$$\frac{C_v}{T}=-\frac{3T^{-\frac{1}{2}}}{8\pi^{\frac{1}{2}}}f_{\frac{3}{2}}-\frac{T^{-\frac{3}{2}}\left(\Delta B+\Delta\mu\right)}{2\pi^{\frac{1}{2}}}f_{\frac{1}{2}}-\frac{T^{-\frac{5}{2}}\left(\Delta B+\Delta\mu\right)^2}{2\pi^{\frac{1}{2}}}f_{-\frac{1}{2}} \tag{85}$$

with $f_n=\mathrm{Li}_n(-\mathrm{e}^{\frac{-\Delta B-\Delta\mu}{T}})$. These present universal scaling behaviour for the charge gapped phase transition in a lattice. The situation is very similar to the I–II transition, where only the charge sector exists.

III–V phase transition: for the phase transition III–V, the emergence of spin degrees of freedom on a half-filled lattice generates the criticality with respect to the critical field $B_c=2\sqrt{1+u^2}-2u$, independent of the chemical potential. Around the quadruple critical point, for charge, J_1,J_2, equations (79) and (80) can be safely neglected, equivalent to the case of an XXX spin chain. Whereas for spin degrees of freedom, the term I_1 in equation (77) is relevant to the low-temperature criticality; by contrast, the integral I_2 has a higher order of power in temperature than that of I_1. Under such circumstances, we determine the free energy near the phase transition III–V as

$$f=-\mu-u-B+\frac{T^{\frac{3}{2}}\pi^{\frac{1}{2}}\lambda_1}{\eta_1^{\frac{1}{2}}}\mathrm{Li}_{\frac{3}{2}}\left(-\mathrm{e}^{-\frac{2\Delta B}{T}}\right). \tag{86}$$

Using the standard thermodynamic relation, we give the following forms of scaling functions for density, magnetization, compressibility, susceptibility and specific heat

$$n=1,\quad m=\frac{1}{2}+\frac{T^{\frac{1}{2}}\pi^{\frac{1}{2}}\lambda_1}{\eta_1^{\frac{1}{2}}}f_{\frac{1}{2}}, \tag{87}$$

$$\chi_c=0,\quad \chi_s=-\frac{2T^{-\frac{1}{2}}\pi^{\frac{1}{2}}\lambda_1}{\eta_1^{\frac{1}{2}}}f_{-\frac{1}{2}}, \tag{88}$$

$$\frac{C_v}{T}=-\frac{3T^{-\frac{1}{2}}\pi^{\frac{1}{2}}\lambda_1}{4\eta_1^{\frac{1}{2}}}f_{\frac{3}{2}}-\frac{2T^{-\frac{3}{2}}\pi^{\frac{1}{2}}\lambda_1\Delta B}{\eta_1^{\frac{1}{2}}}f_{\frac{1}{2}}-\frac{4T^{-\frac{5}{2}}\pi^{\frac{1}{2}}\lambda_1\Delta B^2}{\eta_1^{\frac{1}{2}}}f_{-\frac{1}{2}} \tag{89}$$

with $f_n=\mathrm{Li}_n(-\mathrm{e}^{-\frac{2\Delta B}{T}})$.

II–IV phase transition: for quantum phase transition II–IV, the phase transition occurs at $\varepsilon_1(0)=0$ with charge dispersion $\kappa(k)=-2\cos k-\mu-2u-B$. Let Q denote the Fermi point of $\kappa(k)$, which satisfies $2\cos Q=-\mu-2u-B$. For this case, J_1,J_2, equations (79) and (80), provide a regular part, while I_1 in equation (77) serves as a sudden change of equation of the spin state, i.e. criticality. The explicit expressions of J_1,J_2,I_1 are given in the supplementary material[7]. Substituting the results of J_1,J_2,I_1 into the free energy, equation (81), we have

$$f\approx-\mu-u-B-\frac{2}{3\pi}\beta_1^{\frac{3}{2}}-\frac{1}{60\pi}\beta_1^{\frac{5}{2}}-\frac{\pi T^2}{12\beta_1^{\frac{1}{2}}}-\frac{\pi T^2\beta_1^{\frac{1}{2}}}{96}+\frac{T^{\frac{3}{2}}\pi^{\frac{1}{2}}a_0}{\eta_1^{\frac{1}{2}}}\mathrm{Li}_{\frac{3}{2}}\left(-\mathrm{e}^{-\frac{\Delta t}{T}}\right), \tag{90}$$

where $a_0=\lambda_1-\frac{\beta_1^{\frac{1}{2}}}{\pi^2u}+\beta_1^{\frac{3}{2}}\left(\frac{2\lambda_1}{3\pi u^3\eta_1}-\frac{1}{24\pi^2u}+\frac{1}{3\pi^2u^3}\right)$ and $\Delta t=2(1-\frac{\beta_{1c}^{\frac{1}{2}}}{\pi u})\Delta B-\frac{2\beta_{1c}^{\frac{1}{2}}}{\pi u}\Delta\mu$. Taking the derivatives of the free energy with respect to B, μ and T, we obtain the following scaling forms of the thermal and magnetic properties

$$n=1-\frac{\beta_1^{\frac{1}{2}}}{\pi}-\frac{\beta_1^{\frac{3}{2}}}{24\pi}-\frac{2T^{\frac{1}{2}}\beta_{1c}^{\frac{1}{2}}a_0}{\pi^{\frac{1}{2}}u\eta_1^{\frac{1}{2}}}f_{\frac{1}{2}}, \tag{91}$$

$$m=\frac{1}{2}-\frac{\beta_1^{\frac{1}{2}}}{2\pi}-\frac{\beta_1^{\frac{3}{2}}}{48\pi}+\frac{T^{\frac{1}{2}}\left(1-\frac{\beta_{1c}^{\frac{1}{2}}}{\pi u}\right)\pi^{\frac{1}{2}}a_0}{\eta_1^{\frac{1}{2}}}f_{\frac{1}{2}}, \tag{92}$$

$$\chi_c=\frac{1}{2\pi\beta_1^{\frac{1}{2}}}+\frac{\beta_1^{\frac{1}{2}}}{16\pi}-\frac{4T^{-\frac{1}{2}}\beta_{1c}a_0}{\pi^{\frac{3}{2}}u^2\eta_1^{\frac{1}{2}}}f_{-\frac{1}{2}}, \tag{93}$$

$$\chi_s=\frac{1}{4\pi\beta_1^{\frac{1}{2}}}+\frac{\beta_1^{\frac{1}{2}}}{32\pi}-\frac{2T^{-\frac{1}{2}}\left(1-\frac{\beta_{1c}^{\frac{1}{2}}}{\pi u}\right)^2\pi^{\frac{1}{2}}a_0}{\eta_1^{\frac{1}{2}}}f_{-\frac{1}{2}}, \tag{94}$$

$$\frac{C_v}{T}=\frac{\pi}{6\beta_1^{\frac{1}{2}}}+\frac{\pi\beta_1^{\frac{1}{2}}}{48}-\frac{3T^{-\frac{1}{2}}\pi^{\frac{1}{2}}a_0}{4\eta_1^{\frac{1}{2}}}f_{\frac{3}{2}}-\frac{2T^{-\frac{3}{2}}\pi^{\frac{1}{2}}a_0}{\eta_1^{\frac{1}{2}}}\left[\left(1-\frac{\beta_{1c}^{\frac{1}{2}}}{\pi u}\right)\Delta B-\frac{\beta_{1c}^{\frac{1}{2}}}{\pi u}\Delta\mu\right]f_{\frac{1}{2}}-\frac{4T^{-\frac{5}{2}}\pi^{\frac{1}{2}}a_0}{\eta_1^{\frac{1}{2}}}\left[\left(1-\frac{\beta_{1c}^{\frac{1}{2}}}{\pi u}\right)\Delta B-\frac{\beta_{1c}^{\frac{1}{2}}}{\pi u}\Delta\mu\right]^2f_{-\frac{1}{2}} \tag{95}$$

with $f_n=\mathrm{Li}_n(-\mathrm{e}^{-\frac{\Delta t}{T}})$.

It is further noticed from equation (90) that the background of the free energy involves two types of terms; the temperature-dependent term $-\frac{\pi T^2}{12\beta_1^{\frac{1}{2}}}-\frac{\pi T^2\beta_1^{\frac{1}{2}}}{96}$ comes from the contribution of TLL, whereas the remaining term, $-\mu-u-B-\frac{2}{3\pi}\beta_1^{\frac{3}{2}}-\frac{1}{60\pi}\beta_1^{\frac{5}{2}}$, is equivalent to the energy of noninteracting electrons on a lattice. For simplicity, and without losing generality, we only keep the order of $\beta_1^{\frac{3}{2}}$ in the free energy. For the 1D repulsive Hubbard model, the zero-temperature background is given by

$$f_{\mathrm{H}} \approx -\mu - u - B - \frac{2}{3\pi}\beta_1^{\frac{3}{2}} \approx \beta_1 - 2 - \frac{2}{3\pi}\beta_1^{\frac{3}{2}}. \tag{96}$$

Meanwhile, the ground-state free energy of a noninteracting lattice system is given by

$$f_{\mathrm{NI}} = -\frac{1}{\pi}\left[\sum_{\sigma=\uparrow,\downarrow} 2\sin\left(k_{F,\sigma}\right) + \mu_\sigma \sin\left(k_{F,\sigma}\right)\right], \tag{97}$$

in which $k_{F,\sigma} = \arccos(-\mu_\sigma/2) = \pi n_\sigma, \mu_\uparrow = \mu + B, \mu_\downarrow = \mu - B$. In the limit of high density in the spin-polarized phase, these two free energies, equations (96) and (97), are equivalent

$$\begin{aligned} f_{\mathrm{NI}} &\approx -\frac{2}{\pi}\left(\beta_1^{\frac{1}{2}} - \frac{1}{6}\beta_1^{\frac{3}{2}}\right) - (\mu + B)\,n \\ &\approx -\frac{2}{\pi}\left(\beta_1^{\frac{1}{2}} - \frac{1}{6}\beta_1^{\frac{3}{2}}\right) - (2 - \beta_1)\left(1 - \frac{\beta_1^{\frac{1}{2}}}{\pi}\right) = f_{\mathrm{H}}. \end{aligned} \tag{98}$$

In light of quantum criticality, we refer to phase II as the background. Thus, the terms that do not contribute to the singular part in thermodynamic quantities can be readily recognized, namely,

$$\chi_c^{\mathrm{II}} = \frac{1}{2\pi\beta_1^{\frac{1}{2}}} + \frac{\beta_1^{\frac{1}{2}}}{16\pi}, \tag{99}$$

$$\chi_s^{\mathrm{II}} = \frac{1}{4\pi\beta_1^{\frac{1}{2}}} + \frac{\beta_1^{\frac{1}{2}}}{32\pi}, \tag{100}$$

$$\frac{C_v^{\mathrm{II}}}{T} = \frac{\pi}{6\beta_1^{\frac{1}{2}}} + \frac{\pi\beta_1^{\frac{1}{2}}}{48}. \tag{101}$$

These background results are in agreement with equation (43) with $\delta = \beta_1^{\frac{1}{2}}\left(1 + \frac{1}{24}\beta_1\right)$; here, $\beta_1 = 2 - \mu - 2u - B \approx (\pi - Q)^2 - \frac{1}{12}(\pi - Q)^4 = \delta^2 - \frac{1}{12}\delta^4$. Furthermore, the Wilson ratios for phase II are given by

$$R_{\mathrm{w}}^{\chi_s} = \frac{4\pi^2}{3}\frac{\chi_s}{C_v/T} \approx 2, \qquad R_{\mathrm{w}}^{\chi_c} = \frac{\pi^2}{3}\frac{\chi_c}{C_v/T} \approx 1. \tag{102}$$

IV–V phase transition: the phase transition from IV to V displays a novel subtlety of quantum criticality with charge. At this phase transition, the charge degrees of freedom become gapped and the dressed energy $\kappa(\pi)$ approaches zero. We can directly use the dressed-energy equations with the help of (48) in the supplementary material[7] and $\kappa(\pi) = 0$ under the condition $\delta = 0$, giving the critical fields μ_c, B_c. The integrals I_1 and I_2 in equations (77) and (78) serve as the background contributions resulting from the spin degrees of freedom of the TLL, and the scaling is reflected by J_1 (see explicit derivations in the supplementary material[7]). Using the leading-order contribution in J_1 and I_1, I_2, we finally obtain the following scaling form of the Gibbs free energy

$$\begin{aligned} f \approx & -\mu - u - B - \frac{4}{3}\lambda_1\eta_1 A^3 - \frac{\pi^2 T^2\lambda_1}{6\eta_1 A} - \frac{2}{15}\lambda_2\eta_1 A^5 \\ & - \frac{\pi^2 T^2 \lambda_2}{12\eta_1}A + \frac{T^{\frac{3}{2}} b_0}{2\pi^{\frac{1}{2}}}\mathrm{Li}_{\frac{3}{2}}\left(-\mathrm{e}^{\frac{\Delta t}{T}}\right) \end{aligned} \tag{103}$$

with $b_0 = 1 - \frac{4\lambda_1}{u}A + \left(\frac{\eta_1}{\pi} + 2\lambda_1 - u^2\lambda_2\right)\frac{2A^3}{3u^3}$. Using the thermodynamic relations, the scaling forms of thermal and magnetic properties are explicitly given by

$$n = 1 + \frac{T^{\frac{1}{2}} b_0}{2\pi^{\frac{1}{2}}} f_{\frac{1}{2}}, \tag{104}$$

$$m = \frac{1}{2} - \frac{2\lambda_1 A}{1 + \frac{A}{\pi u}} - \frac{1}{3}\lambda_2 A^3 + \frac{T^{\frac{1}{2}}\left(1 - \frac{4A_c}{\pi u + A_c}\right) b_0}{4\pi^{\frac{1}{2}}} f_{\frac{1}{2}}, \tag{105}$$

$$\chi_c = -\frac{T^{-\frac{1}{2}} b_0}{2\pi^{\frac{1}{2}}} f_{-\frac{1}{2}}, \tag{106}$$

$$\begin{aligned} \chi_s = & \frac{2\lambda_1}{\eta_1 A\left(1 + \frac{A}{\pi u}\right)^3} + \frac{\lambda_2}{\eta_1}\frac{A}{1 + \frac{A}{\pi u}} \\ & - \frac{T^{-\frac{1}{2}}\left(1 - \frac{4A_c}{\pi u + A_c}\right)^2 b_0}{4\pi^{\frac{1}{2}}} f_{-\frac{1}{2}}, \end{aligned} \tag{107}$$

$$\begin{aligned} \frac{C_v}{T} = & \frac{\pi^2\lambda_1}{3\eta_1 A} + \frac{\pi^2\lambda_2 A}{6\eta_1} - \frac{3T^{-\frac{1}{2}} b_0}{8\pi^{\frac{1}{2}}} f_{\frac{3}{2}} \\ & - \frac{T^{-\frac{3}{2}} b_0}{2\pi^{\frac{1}{2}}}\left[\Delta\mu + \left(1 - \frac{4A_c}{\pi u + A_c}\right)\Delta B\right] f_{\frac{1}{2}} \\ & - \frac{T^{-\frac{5}{2}} b_0}{2\pi^{\frac{1}{2}}}\left[\Delta\mu + \left(1 - \frac{4A_c}{\pi u + A_c}\right)\Delta B\right]^2 f_{-\frac{1}{2}}, \end{aligned} \tag{108}$$

where we denoted $f_n = \mathrm{Li}_n(-\mathrm{e}^{\frac{\Delta t}{T}})$.

Moreover, we observe that phase V represents the source of the background for the spin degrees of freedom. Thus, we may easily identify the contributions from the Mott phase V in the above scaling functions, namely,

$$\chi_c^{\mathrm{V}} = 0, \tag{109}$$

$$\chi_s^{\mathrm{V}} = \frac{2\lambda_1}{\eta_1 A\left(1 + \frac{A}{\pi u}\right)^3} + \frac{\lambda_2}{\eta_1}\frac{A}{1 + \frac{A}{\pi u}}, \tag{110}$$

$$\frac{C_v^{\mathrm{V}}}{T} = \frac{\pi^2\lambda_1}{3\eta_1 A} + \frac{\pi^2\lambda_2 A}{6\eta_1}. \tag{111}$$

Comparing the above results with equations (44)–(49), we find these results are consistent with each other. Consequently, the Wilson ratios are given by

$$\begin{aligned} R_{\mathrm{w}}^{\chi_s} &= \frac{4\pi^2}{3}\frac{\chi_s}{C_v/T} \approx \frac{8}{\left(1 + \frac{A}{\pi u}\right)^3} + \frac{8\lambda_2 A^3}{\pi u\lambda_1}, \\ R_{\mathrm{w}}^{\chi_c} &= \frac{\pi^2}{3}\frac{\chi_c}{C_v/T} = 0, \end{aligned} \tag{112}$$

showing the nature of the TLL at low temperature.

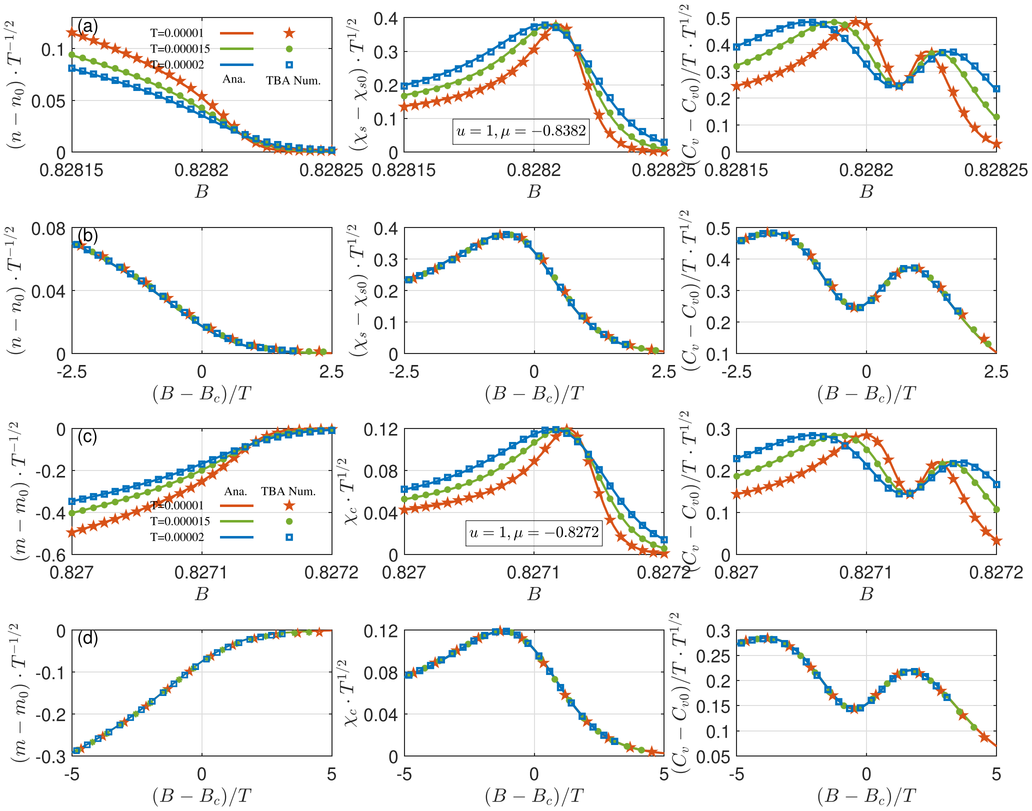

Figure 14. Rows (a) and (b) show the universal scaling behaviour of electron density and spin susceptibility, as well as specific heat vs the magnetic field B (the argument $(B-B_c)/T$) for phase transitions II–IV. The analytical results (solid lines), equations (91)–(95), agree well with the numerical solutions of the TBA equations. Rows (c) and (d) show the universal scaling behaviour of magnetization and charge susceptibility, as well as specific heat vs the magnetic field B (the argument $(B-B_c)/T$) for phase transitions IV–V. The analytical results (solid lines), equations (104)–(108), agree well with the numerical solution of the TBA equations. All the parameters are situated within the white empty circle in figure 1.

In figures 14(a) and (b) and 14(c) and (d), we plot the universal scaling behaviour of electron density and magnetization, and spin and charge susceptibilities, as well as specific heat for phase transitions II–IV and IV–V, respectively. They show that analytic expressions of their scaling functions, equations (91)–(95) and equations (104)–(108), are in good agreement with the numerical results obtained from the TBA equations. We note that in figures 14(a) and (c), all lines at different temperatures intersect at the QCP, while figures 14(b) and (d) show the scaling function invariant in terms of $\frac{\Delta B}{T}$. It is essential to note that all these scaling functions read off the dynamical exponent $z=2$ and the correlation critical exponent $\nu=1/2$, for example, the susceptibility, equation (67): also, see [123]. In the critical region, the polylog function represents the free fermion type of generating function associated with the dynamic critical exponent $z=2$ and the correlation critical exponent $\nu=\frac{1}{2}$ [123, 128]. In the zero temperature limit, the singular part of the susceptibility can be expressed as $\chi_s^s\propto T^{-\frac{1}{2}}(\Delta B/T)^{-\frac{1}{2}}=(\Delta B)^{-\frac{1}{2}}$. Regarding the definition of the critical exponent γ with respect to the general form $\chi\propto(g-g_c)^{-\gamma}$, here g is the driving parameter; we find $\gamma=\frac{1}{2}$ for the second-order derivatives of the free energy. On the other hand, the correlation length can be expressed as $\xi\propto T^{-\frac{1}{z}}$. In summary, at the critical point $\Delta B=0$, we also find that thermodynamic properties $\frac{C_v}{T}$, χ_s, ξ satisfy the following scaling laws

$$\frac{C_v}{T}\propto T^{\frac{d-z}{z}},\quad \chi_s\propto T^{-\frac{\gamma}{\nu z}},\quad \xi\propto T^{-\frac{1}{z}}, \tag{113}$$

which signify the non-Fermi liquid behaviour at the QCP [128–130].

3.1.5. *General scaling functions at quantum criticality.*

In the previous subsection, we presented some analytical results for each phase transition. We observe that the coefficients a_0 in equation (90) and b_0 in equation (103) of free energies solely rely on the root densities (60) and (62) in the supplementary material[7] with $a_0\approx\sigma(0), b_0\approx 2\pi\rho(\pi)$. Significantly, it is found that the free energies are related to densities and dressed energies in compact forms for different phase transitions

$$\text{I-II: } f=u+T^{\frac{3}{2}}\pi^{\frac{1}{2}}\rho(0)\left(\frac{\kappa''(0)}{2}\right)^{-\frac{1}{2}}\mathrm{Li}_{\frac{3}{2}}\left(-\mathrm{e}^{-\frac{\kappa(0)}{T}}\right), \tag{114}$$

$$\text{II-III: } f = f_0 + T^{\frac{3}{2}}\pi^{\frac{1}{2}}\rho(\pi)\left(\frac{-\kappa''(\pi)}{2}\right)^{-\frac{1}{2}}\mathrm{Li}_{\frac{3}{2}}\left(-\mathrm{e}^{\frac{\kappa(\pi)}{T}}\right), \tag{115}$$

$$\text{V-III: } f = f_0 + T^{\frac{3}{2}}\pi^{\frac{1}{2}}\sigma_1(0)\left(\frac{\varepsilon_1''(0)}{2}\right)^{-\frac{1}{2}}\mathrm{Li}_{\frac{3}{2}}\left(-\mathrm{e}^{-\frac{\varepsilon_1(0)}{T}}\right), \tag{116}$$

$$\text{II-IV: } f = f_0 - \frac{\pi T^2}{6v_c} + T^{\frac{3}{2}}\pi^{\frac{1}{2}}\sigma_1(0)\left(\frac{\varepsilon_1''(0)}{2}\right)^{-\frac{1}{2}} \mathrm{Li}_{\frac{3}{2}}\left(-\mathrm{e}^{-\frac{\varepsilon_1(0)}{T}}\right), \tag{117}$$

$$\text{V-IV: } f = f_0 - \frac{\pi T^2}{6v_s} + T^{\frac{3}{2}}\pi^{\frac{1}{2}}\rho(\pi)\left(\frac{-\kappa''(\pi)}{2}\right)^{-\frac{1}{2}} \mathrm{Li}_{\frac{3}{2}}\left(-\mathrm{e}^{\frac{\kappa(\pi)}{T}}\right), \tag{118}$$

where f_0 comes from the ground state; the terms with T^2 reflect the contributions from the background parts; $\sigma_1(0)$ denotes the density of length-1 spin strings at $\Lambda = 0$; the second derivative $\varepsilon_1''(0) \equiv \frac{\mathrm{d}^2\varepsilon_1}{\mathrm{d}\Lambda^2}\Big|_{\Lambda=0}$; and $\rho(0)$, $\rho(\pi)$ denotes the charge density at $k = 0, \pi$, respectively. Similarly, for the charge dressed energy, $\kappa''(0) \equiv \frac{\mathrm{d}^2\kappa}{\mathrm{d}k^2}\Big|_{k=0}, \kappa''(\pi) \equiv \frac{\mathrm{d}^2\kappa}{\mathrm{d}k^2}\Big|_{k=\pi}$. The polylog function $\mathrm{Li}_{\frac{3}{2}}$ represents the generating function of free fermion criticality. The above scaling functions of the free energy for different quantum phase transitions are valid for arbitrary interaction strengths and fillings, revealing a microscopic origin of the quantum phase transitions associated with the dressed energies. The functions $-\varepsilon_1(0)$, $-\kappa(0)$, $\kappa(\pi)$ serve as criticality and depend on the energy gaps away from the QCPs, i.e.

$$-\varepsilon_1(0), -\kappa(0), \kappa(\pi) \approx \alpha_B\Delta B + \alpha_\mu\Delta\mu + \alpha_u\Delta u. \tag{119}$$

The factors $\alpha_{(B,\mu,u)}$ represent the different transition paths in the vicinities of QCPs driven by external fields. These expressions, equations (114)–(118), display concise and elegant configurations that are independent of specific details for arbitrary filling and interaction strength, and can apply to other models with second-order phase transitions associated with the dynamical critical experiment $z = 2$ and correlation length exponent $\nu = 1/2$. The detailed derivations for these formulas are given in the supplementary material[7].

3.2. Spin-incoherent Luttinger liquid

Although SILL has been studied in the literature [65–69], almost all those works are based on the framework of bosonization. There are still no studies of such novel phenomenon from the Bethe ansatz perspective and quantum phase transition. It is very insightful to conceive the SILL from both correlation functions and thermodynamics. In section 2, we used the variations of η-pair and spin magnetizations $(\Delta\eta^z, \Delta S^z)$ to characterize the fractional charge and spinon excitations. Such fractionalized quasi-particles reveal the fermionic nature of quasiparticles, forming the Luttinger liquid. Meanwhile, we found the only possible fractional spin excitations, which can lead to the spin-incoherent liquid at low temperatures. In this section, we focus on rigorous results of the SILL in terms of specific heat, criticality and correlation functions.

3.2.1. Thermodynamics in SILL. In the previous analysis given in section 2, we observe that a crossover region fanning out from the critical point does show the existence of the SILL above the phase boundary of the TLL and up to a critical temperature, see figure 15. This phenomenon can be revealed through thermodynamic quantities of the model, such as specific heat. We now identify different energy scaling of the SILL from the TLL and quantum criticality. We first analyze the variables $\varepsilon_1(0)$ emerged in the polylog functions of II–IV transition in equation (117),

$$\varepsilon_1(0) = 2B - \int_{-\pi}^{\pi}\mathrm{d}k\cos k a_1(\sin k - \Lambda)T\ln\left(1 + e^{-\frac{\kappa(k)}{T}}\right)|_{\Lambda=0}, \tag{120}$$

where $\varepsilon_1(0) = 0$, <0, >0 at the exact critical point, in phase IV and phase II, respectively, measuring the distance away from the phase boundary of II–IV. In this case, the Fermi point of the charge $\kappa(Q) = 0$ gives $2\cos Q = -\mu - 2u - B$, leading to $\kappa(k) = -2\cos k + 2\cos Q$; here, Q is the Fermi point in the charge sector. Thus, $\varepsilon_1(0)$ at zero temperature can be simplified by

$$\varepsilon_1(0) = 2B - \frac{4u}{\pi}\int_0^Q \mathrm{d}k\frac{\cos k}{u^2 + \sin^2 k}(\cos k - \cos Q) + O\left(T^2\right) \tag{121}$$

with the temperature term omitted. By further performing Taylor expansion around the critical point B_c for fixed μ and u, we have

$$Q \approx Q_c + \frac{1}{2\sin Q_c}\Delta B \tag{122}$$

with $Q_c = \arccos\left(-\frac{1}{2}(\mu_c + 2u_c + B_c)\right)$. After some algebra, the quantity $\varepsilon_1(0)$ in the vicinity of the critical point of the phase transition II–IV can be found to be given by

$$\begin{aligned}\varepsilon_1(0) &\approx 2B - \frac{4u}{\pi}\int_0^{Q_c}\mathrm{d}k\frac{\cos k}{u^2 + \sin^2 k}(\cos k - \cos Q_c \\ &\quad + \sin Q_c(Q - Q_c)) \\ &\approx 2\Delta B - \frac{2u}{\pi}\int_0^{Q_c}\mathrm{d}k\frac{\cos k}{u^2 + \sin^2 k}\Delta B \\ &\approx 2\Delta B\left[1 - \frac{1}{\pi}\arctan\left(\frac{\sin Q_c}{u}\right)\right],\end{aligned} \tag{123}$$

where the second line brings in the condition $\varepsilon_1(0)|_{B,Q_c} = 2\Delta B$ with the limit $\varepsilon_1(0)|_{B_c,Q_c} = 0$. Therefore, $\alpha_B = -2\left[1 - \arctan\left(\sin Q_c/u\right)/\pi\right]$ can be obtained from the definition $-\varepsilon_1(0) \equiv: \alpha_B\Delta B$.

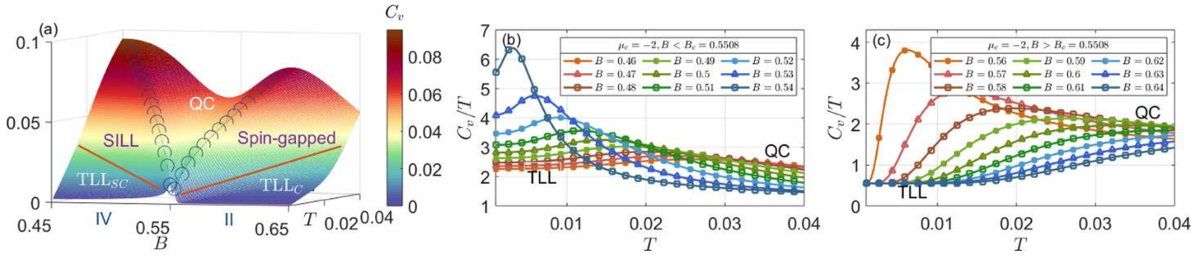

Figure 15. (a) A 3D plot of specific heat in the $T-B-C_v$ coordinate at $\mu=-2, u=1$ for the IV-II phase transition, which is marked with a dashed line in figure 1. The blue circled symbols present the critical temperatures determined by the maximum values of the specific heat (equation (124)), consistent with numerical simulation. The red lines mark the TLL phase boundaries, below which the specific heat shows a linear temperature dependency. Crossover regimes between the blue circled symbols and the red lines denote the SILL phase (on the left) and the spin-gapped phase (on the right). (b) and (c) The specific heat vs temperature near the phase transition IV-II for the magnetic field is less than (greater than) the critical magnetic field B_c, respectively. The temperature-independent region and the temperature-square-dependent region in the ratio C_v/T can be visible, characterizng the thermodynamics of the TLL and SILL, respectively.

On the other hand, in the quantum critical region, the heat capacity satisfies the universal scaling form

$$C_v/T = c_0 + c_1 T^{-1/2}\left[\frac{3}{4}\mathrm{Li}_{\frac{3}{2}}\left(-\mathrm{e}^x\right) - x\mathrm{Li}_{\frac{1}{2}}\left(-\mathrm{e}^x\right) + x^2\mathrm{Li}_{-\frac{1}{2}}\left(-\mathrm{e}^x\right)\right] + O\left(\left(\Delta B/T\right)^{5/2}\right), \tag{124}$$

where c_0 is the zero temperature background, c_1 is a coefficient depending on the transition point, explicitly see equation (95), and $x = -\varepsilon_1(0)/T = \alpha_B \Delta B/T$. A brief discussion about an interaction-driven case is given in [109]. One characteristic of the heat capacity is that it displays bimodal structures around the QCP. Thus, the peaks of the heat capacity conveniently mark out the quantum critical (QC) boundaries. These peaks can be determined from $\partial C_v/\partial B = 0$, i.e.

$$\frac{1}{4}\mathrm{Li}_{\frac{1}{2}}\left(-\mathrm{e}^x\right) - x\mathrm{Li}_{-\frac{1}{2}}\left(-\mathrm{e}^x\right) - x^2\mathrm{Li}_{-\frac{3}{2}}\left(-\mathrm{e}^x\right) = 0, \tag{125}$$

which gives two solutions $x_1 = -1.5629, x_2 = 3.6205$. Figure 15(a) shows the overall behaviour of the quantum criticality in the vicinity of the IV-II phase transition in the $T-B-C_v$ coordinate. The blue circled symbols denote the maxima of specific heat from the analytical results, equation (124), showing good agreement with the numerical calculations based on the TBA equations. In this critical region, $T \gg \Delta B = B - B_c$, and the other thermodynamic properties also show universal scaling behaviour given by equations (91)–(95).

As the temperature gradually decreases from the QC part to a certain extent, TLL regions appear; see the areas below the red lines in figure 15(a). Around the critical point $B_c = 0.55$, two TLLs emerge. In the region with $B < B_c$, denoted as TLL$_{SC}$, the system lies in phase IV with spin and charge degrees of freedom coexisting. For $B > B_c$, the system lies in phase II with only charge degrees of freedom, denoted as TLL$_C$. In the TLL region, the specific heat C_v is linearly dependent on T; also, see the discussion in section 3. In the crossover region between QC and the TLL$_C$ phase, the spin sector is gapped. By utilizing the asymptotic behaviour of the polylog function [131] and expanding equation (95), the specific heat in this gapped region is given by

$$C_v \approx \frac{\pi T}{3v_c} + \frac{3\pi^{\frac{1}{2}}a_0}{4}\left(\eta_1\right)^{-\frac{1}{2}} T^{\frac{1}{2}}\mathrm{e}^{\alpha_B \Delta B/T} + O\left(\Delta B \mathrm{e}^{\alpha_B \Delta B/T}\right). \tag{126}$$

In comparison, in the crossover region between QC and the TLL$_{SC}$ phase, i.e. in the temperature range $E_s \sim k_F v_s \ll k_B T \ll E_c \sim k_F v_c$, lies the SILL [65–69]. In this region, the specific heat is given by

$$C_v \approx \frac{\pi T}{3v_c} + \frac{\pi^2 a_0\left(\eta_1\right)^{-\frac{1}{2}}\left(-\varepsilon_1(0)\right)^{-\frac{1}{2}}T}{3} \times\left[1 + \frac{21\pi^2}{40}\left(-\varepsilon_1(0)\right)^{-2}T^2\right] + O\left(T^4\right), \tag{127}$$

which manifests a gas–liquid coexistence. We note that the coefficient before the square bracket should be $\pi T/(3v_s)$. The proof is given in the following. The spin dressed energy around the QCP is written as $\varepsilon_1(\Lambda) = D_1\Lambda^2 + D_2$. Thus, for the SILL region, the spin Fermi point A is related to $\varepsilon_1(A) = D_1 A^2 + D_2 = 0$, resulting in $A = (-D_2/D_1)^{1/2}$. On the other hand, by the definition of $D_{1,2}$ given in equations (75) and (76), we have $D_1 = \varepsilon_1''(0)/2 = \eta_1, D_2 = \varepsilon_1(0)$. Therefore, the Fermi point A is expressed as $A = (-\varepsilon_1(0)/\eta_1)^{1/2}$. Using the definition of a_0, see equation (90), we have $a_0 = \sigma_1(0) \approx \sigma_1(A)$ and $\varepsilon_1'(A) = 2\eta_1 A$, which renders

$$\begin{aligned}\frac{\pi^2 a_0\left(\eta_1\right)^{-\frac{1}{2}}\left(-\varepsilon_1(0)\right)^{-\frac{1}{2}}T}{3} &= \frac{\pi^2\sigma_1(A)T\left(\eta_1\right)^{\frac{1}{2}}}{3}\frac{1}{\eta_1\left(-\varepsilon_1(0)\right)^{\frac{1}{2}}} \\ &= \frac{\pi^2\sigma_1(A)T}{3\eta_1 A} = \frac{\pi\cdot 2\pi\sigma_1(A)T}{3\varepsilon_1'(A)} \\ &= \frac{\pi T}{3v_s}.\end{aligned} \tag{128}$$

This immediately gives a universal thermodynamic relation of the SILL

$$C_v \approx \frac{\pi T}{3}\left(\frac{1}{v_c}+\frac{1}{v_s}\right)+\frac{7\pi^3 T^3}{40 v_s\left(-\varepsilon_1(0)\right)^2}+O\left(T^4\right). \tag{129}$$

The result in equation(129) is complementary to the correlation function in SILL, which will be studied below.

Furthermore, in figures 15(b) and (c), we plot the specific heat below and above the QCP for different values of magnetic fields. It is obvious to see the region of the linear temperature-dependent specific heat, a crossover region of the SILL with both the linear and cubic temperature-dependent specific heat. The latter marks the crossover region $E_s \sim k_F v_s \ll k_B T \ll E_c \sim k_F v_c$, showing the thermodynamic behaviour of the SILL.

3.2.2. *Correlation functions in SILL.*

The SILL regime with $k_F v_s < k_B T \ll k_F v_c$ lies between the boundaries of TLL and QC. In this region, the spin degrees of freedom behave like hot spins, whereas the charge still behaves as a collective motion of bosons. As a result, the SILL largely behaves like a spin and charge decoherence liquid, i.e. possessing only a propagating charge mode but not a spin mode, see [65–69]. In the spin sector, the magnetic exchange energy is lower than the Fermi energy, resulting in the spin being thermally excited with equal probability [69]. In the strong coupling regime, the spin degrees of freedom show spin dynamics of a Heisenberg chain with a nondispersive spinon band due to small effective exchange coupling $J = 4t^2/U$, whereas the charge acts as noninteracting fermions with a dispersive spectrum $\kappa(k) = -2t\cos(k)$. This SILL theory can also be captured in the excitation spectrum in the low-density regime in figure 6(b). The concept of SILL is helpful for explaining the appearance of a conductance plateau in a quantum wire [70]. When interaction increases, or in the vicinity of the QCP, the spin velocity progressively dwindles to zero. This means that the spin sector loses dynamics, indicating the emergence of the SILL.

In this regime $E_s \ll T \ll E_c$, the spin sector is totally thermally averaged and equally excited, whereas the charge remains at a relevant low-energy performance, rendering the correlation functions independent of temperature [67]. We note that the TLL theory has its own applicable condition $T \ll E_c, E_s$, whereas for the region $E_s \ll T \ll E_c$, the energy scales of charge and spin degrees of freedom can be dealt with separately [65]. Under such a circumstance, the finite-temperature correlation functions in terms of conformal field theory [6, 34, 35] still remain valid for the charge and spin degrees of freedom operating with different limits, i.e.

$$|x \pm \mathrm{i}v_c t| \ll v_c/T, \qquad |x \pm \mathrm{i}v_s t| \gg v_s/T. \tag{130}$$

This is essential to capture the asymptotic behaviour of the SILL. Here, we would like to mention that the remaining temperature term in the spin sector can be replaced by the typical energy scale of spin

$$T \sim E_s \sim J \sim \left(k_{F\uparrow}+k_{F\downarrow}\right)/2 \cdot v_s \equiv k_F v_s.$$

With the help of the finite-temperature asymptotics of correlation functions under the condition in equation (130), the two-point correlation functions of prime fields can be obtained as

$$\begin{aligned}\langle \phi(x,t)\,\phi(0,0)\rangle = {} & \sum A\left(D_c, D_s, N_c^{\pm}, N_s^{\pm}\right)\exp\left(-2\mathrm{i}D_c k_{F,\uparrow}x\right)\\ & \times \exp\left(-2\mathrm{i}\left(D_c+D_s\right)k_{F,\downarrow}x\right)\\ & \times \frac{1}{\left(x-\mathrm{i}v_c t\right)^{2\Delta_c^+}\left(x+\mathrm{i}v_c t\right)^{2\Delta_c^-}}\\ & \times \left(2\pi\alpha k_F\right)^{2\Delta_s^+ + 2\Delta_s^-}\,\mathrm{e}^{-\pi\alpha\left(2\Delta_s^+ + 2\Delta_s^-\right)k_F x},\end{aligned} \tag{131}$$

where the conformal dimensions in gapless phases read

$$\begin{aligned}2\Delta_c^{\pm}\left(\Delta\boldsymbol{N},\boldsymbol{D}\right) = {} & \left(\mathrm{Z}_{cc}D_c+\mathrm{Z}_{sc}D_s \pm \frac{\mathrm{Z}_{ss}\Delta N_c - \mathrm{Z}_{cs}\Delta N_s}{2\det\mathrm{Z}}\right)^2\\ & + 2N_c^{\pm},\\ 2\Delta_s^{\pm}\left(\Delta\boldsymbol{N},\boldsymbol{D}\right) = {} & \left(\mathrm{Z}_{cs}D_c+\mathrm{Z}_{ss}D_s \pm \frac{\mathrm{Z}_{cc}\Delta N_s - \mathrm{Z}_{sc}\Delta N_c}{2\det\mathrm{Z}}\right)^2\\ & + 2N_s^{\pm}.\end{aligned} \tag{132}$$

Here, Z is the dressed-charge matrix given in equation (59), while $N_\alpha^{\pm}, \Delta\vec{N}, \vec{D}$ are related to the three types of excitations: adding particles from left and right Fermi points, changing the total particle number, and moving a number of particles from the left Fermi point to the right Fermi point (also, see [22]). From equation (131), the spin-spin correlation in the spin sector displays exponential decay as a function of distance, while the correlation in the charge sector shows a power-law decay. Explicitly, based on the correlation functions obtained from the finite-temperature conformal field theory (CFT), we may calculate various two-point correlations of field operators close to the critical field B_c in the SILL regime, including the single-particle Green's function

(1) $G^{\uparrow}$

$$\begin{aligned}G^{\uparrow}_{B\to B_c} \sim {} & \frac{\exp\left(-\mathrm{i}k_{F,\uparrow}x\right)}{\left(x-\mathrm{i}v_c t\right)^{1-\frac{2}{\pi}\sqrt{1-\frac{B}{B_c}}}}\\ & \times \left(2\pi\alpha k_F\right)^{\frac{1}{2}-\frac{1}{\pi}\sqrt{1-\frac{B}{B_c}}}\,\mathrm{e}^{-\pi\alpha\left(\frac{1}{2}-\frac{1}{\pi}\sqrt{1-\frac{B}{B_c}}\right)k_F x}\\ & + h.c.\end{aligned} \tag{133}$$

This result was derived for the region close to the critical field B_c, corresponding to the phase transition II–IV. Similarly, for other correlations

(2) $G^{\downarrow}$

$$\begin{aligned}G^{\downarrow}_{B\to B_c} \sim {} & \frac{\exp\left(-\mathrm{i}k_{F,\downarrow}x\right)}{\left(x-\mathrm{i}v_c t\right)^{\frac{1}{4}+\frac{1}{\pi}\sqrt{1-\frac{B}{B_c}}}\left(x+\mathrm{i}v_c t\right)^{\frac{1}{4}-\frac{1}{\pi}\sqrt{1-\frac{B}{B_c}}}}\\ & \times \left(2\pi\alpha k_F\right)^{1-\frac{2}{\pi}\sqrt{1-\frac{B}{B_c}}}\,\mathrm{e}^{-\pi\alpha\left(1-\frac{2}{\pi}\sqrt{1-\frac{B}{B_c}}\right)k_F x}\\ & + h.c.\end{aligned} \tag{134}$$

(3) G^n

$$
\begin{aligned}
G^n_{B\to B_c} \sim\, & n^2 + (\exp(2\mathrm{i}k_{F,\uparrow}x) \\
& + \exp(-2\mathrm{i}k_{F,\uparrow}x))\,\frac{1}{|x-\mathrm{i}v_ct|^{2-\frac{8}{\pi}\sqrt{1-\frac{B}{B_c}}}} \\
& \times (2\pi\alpha k_F)^{2-\frac{4}{\pi}\sqrt{1-\frac{B}{B_c}}} \\
& \mathrm{e}^{-\pi\alpha\left(2-\frac{4}{\pi}\sqrt{1-\frac{B}{B_c}}\right)k_Fx} + (\exp(2\mathrm{i}k_{F,\downarrow}x) \\
& + \exp(-2\mathrm{i}k_{F,\downarrow}x)) \\
& \times (2\pi\alpha k_F)^{2-\frac{4}{\pi}\sqrt{1-\frac{B}{B_c}}}\,\mathrm{e}^{-\pi\alpha\left(2-\frac{4}{\pi}\sqrt{1-\frac{B}{B_c}}\right)k_Fx} \\
& + (\exp(2\mathrm{i}(k_{F,\uparrow}+k_{F,\downarrow})x) \\
& + \exp(-2\mathrm{i}(k_{F,\uparrow}+k_{F,\downarrow})x))\,\frac{1}{|x-\mathrm{i}v_ct|^2}.
\end{aligned} \tag{135}
$$

(4) $G^\perp$

$$
\begin{aligned}
G^\perp_{B\to B_c} \sim\, & (\exp(\mathrm{i}(k_{F,\uparrow}+k_{F,\downarrow})x) \\
& + \exp(-\mathrm{i}(k_{F,\uparrow}+k_{F,\downarrow})x))\,\frac{1}{|x-\mathrm{i}v_ct|^{\frac{1}{2}}} \\
& \times (2\pi\alpha k_F)^{\frac{1}{2}+\frac{1}{\pi}\sqrt{1-\frac{B}{B_c}}}\,\mathrm{e}^{-\pi\alpha\left(\frac{1}{2}+\frac{1}{\pi}\sqrt{1-\frac{B}{B_c}}\right)k_Fx}.
\end{aligned} \tag{136}
$$

(5) G^p

$$
\begin{aligned}
G^p_{B\to B_c} \sim\, & \exp(-\mathrm{i}(k_{F,\uparrow}+k_{F,\downarrow})x)\,\frac{1}{(x-\mathrm{i}v_ct)^{\frac{9}{4}}(x+\mathrm{i}v_ct)^{\frac{1}{4}}} \\
& \times (2\pi\alpha k_F)^{\frac{1}{2}-\frac{3}{\pi}\sqrt{1-\frac{B}{B_c}}}\,\mathrm{e}^{-\pi\alpha\left(\frac{1}{2}-\frac{3}{\pi}\sqrt{1-\frac{B}{B_c}}\right)k_Fx} \\
& + h.c.
\end{aligned} \tag{137}
$$

It should be noted that although these results are obtained in a very rough approximation, they capture the essential features of the SILL [67], i.e. spin-spin correlation decays exponentially while the correlations in the charge degrees of freedom behave like spinless noninteracting fermions. The field theory approach was given in [65–67]. The reason why the crossover in the vicinity of the phase transition between IV and V cannot develop such a similar concept as charge-incoherent Luttinger liquid is that near a half-filled lattice, the charge velocity monotonically and exponentially tends to zero [72]. This means subtlety occurs near the Mott phase transition due to the rapidly vanishing charge collective mode. This limitation is called the holon confinement. In the next section, we will develop a new concept, contact susceptibility, to study the Mott phase transition.

3.3. Contact and contact susceptibility

In this section, we focus on an experimentally measurable quantity double occupancy [132, 133], as well as the associated contact, revealing the competition between thermal fluctuations and quantum fluctuations from different sources, i.e. external fields and interaction. The double occupancy serves as an efficient instrument to demarcate phase transitions, especially the Mott phase transition in the extended Hubbard model with long-range interaction [30, 31]. On the other hand, the partial wave contact, which was first proposed in ultracold Fermi gas [134, 135], has become an important theme in the study of ultracold atoms [136–141]. Here, we will introduce the concept of contact susceptibilities with respect to the temperature, magnetic field and chemical potential, and investigate applications of these contact susceptibilities. We will show that the susceptibilities build up a general connection between interaction-driven quantum criticality and the phase transitions induced by external fields. Using these relations, we will also obtain caloric effects in interaction-driven quantum refrigeration and scaling laws at quantum criticality, which will pave a way for future studies of interaction-driven quantum cooling.

3.3.1. Double occupancy and Mott phase.

In the Hubbard model, the lattice filling parameter, interaction strength and external fields can drive different phase transitions [75, 142]. In contrast to the dilute limit case, the Mott insulator phase induced by interaction is much less understood. When the interaction strength increases up to a critical value u_c [30, 31, 72] in the canonical ensemble, the system reaches a Mott insulator state in the extended Hubbard model. The half-filled phase can be delineated by the Luther–Emery liquid with a charge gapless mode and a spin-gapped mode [79], in which the excitations comply with bosonic and fermionic statistics, respectively. To explore the magnetic order and detect the Mott phase transition, one can introduce the double occupancy $d=\frac{1}{N}\sum_i\langle n_{i,\uparrow}n_{i,\downarrow}\rangle$, which depicts the probability of two electrons with opposite spin occupying a single lattice site with potential energy $E_{\mathrm{pot}}=ud$. The double occupancy has been invested extensively in theoretical and experimental research on the Hubbard model in the half filled state. It appears to show discontinuity as the interaction approaches critical coupling in interaction-induced Mott transition (note that $u_c=0$ for this model in the canonical ensemble, in which this phenomenon is inconspicuous) and exhibits nonmonotonic behaviour in the half-filled state as the temperature varies, similar to the Pomeranchuk effect (the melting pressure of liquid helium-3 shows a trend of first decreasing and then increasing with temperature) [30, 31, 33]. It also reveals the competing physics from the charge and spin fluctuations. For doping-induced Mott transition, d is significantly suppressed in the area of $\mu<u$ and generates a pronounced signal when the density exceeds unity [31]. It is useful to locate the Mott transition point through the detection of double occupancy.

In the canonical ensemble, the double occupancy can be obtained from the free energy f by

$$
d=\frac{1}{N}\sum_i\langle n_{i,\uparrow}n_{i,\downarrow}\rangle=\frac{1}{4}\frac{\partial f}{\partial u}-\frac{1}{4}+\frac{n_c}{2}, \tag{138}
$$

in which the last two terms $-1/4+n_c/2$ stem from the extra terms $-2uN+uL$ in the Hamiltonian. We can define $C=\partial f/\partial u$ to be the lattice version of contact C,

$$
C=\partial f/\partial u=4d-2n_c+1, \tag{139}
$$

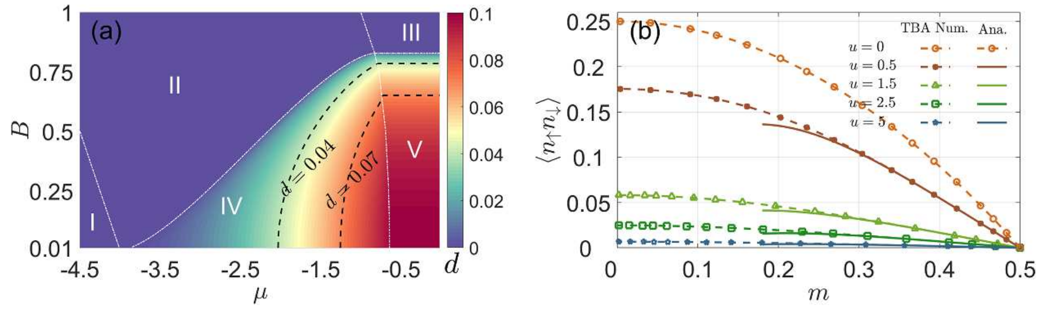

Figure 16. (a) Double occupancy maps out the phase diagram of the 1D Hubbard model plotted. The white dot–dashed lines show the zero-temperature phase boundaries, while the thick dashed lines show the contour lines of $d = 0.04$ and $d = 0.07$, respectively. At the critical points, the double occupancy suddenly changes. The parameter setting for the numerics is the same as figure 10(a), i.e. $T = 0.005$ and $u = 1$. (b) Double occupancy versus magnetization in the Mott phase for various coupling strengths. The numerics from the TBA equations confirm the accuracy of the analytical result, equation (138), with the contact given by equation (140).

which is analogous to Tan's contact [134, 141] in the continuous systems of ultracold atoms. Regarding the role that the double occupancy can reflect the phase information, we expect that d distinguishes different phases with and without internal degrees of freedom, see figure 16(a). The d always vanishes for phases I, II and III and has no demarcation lines between these phases. The boundaries of II and IV or III and V are obvious, while for IV and V the inflection point of the contour line marks the phase transition. Due to the fact that the double occupancy essentially reflects charge fluctuations at the Mott insulator accompanied by the existence of the antiferromagnetic order, we demonstrate the roles of the magnetic field B and the interaction strength u on d in figure 16(b). It is clear that repulsive interaction always lowers the possibility of double occupancy, which is quite intuitive. When the interaction increases, the electrons with different spins repel each other more strongly and the system becomes more incompressible. The infinity coupling $u \to \infty$ makes the particles fully localized. The decrease caused by magnetization originates from the tendency that the magnetic field tends to align the spins of electrons in the field direction. Through the derivative of the background term in equation (103) with respect to u, the exact analytic expression of the contact C_0 in the Mott phase V of the ground state can be obtained as

$$C_0 = -1 - \frac{4}{3}\frac{\partial}{\partial u}(\lambda_1\eta_1)A^3 - 4\lambda_1\eta_1 A^2\frac{\partial A}{\partial u} - \frac{2}{15}\frac{\partial}{\partial u}(\lambda_2\eta_1)A^5 - \frac{2}{3}\lambda_2\eta_1 A^4\frac{\partial A}{\partial u}, \tag{140}$$

where $\partial A/\partial u$ is given in equation (151). We plotted the double occupancy through equation (140) (solid lines) in figure 16(b), showing good agreement between this analytical result and the numerical calculation from the TBA equations. Based on the relation from equation (139), it is more essential to investigate the variations of the contact with respect to the changes in the external fields and temperature.

3.3.2. *Contact susceptibilities and Mott phase transition.*

In comparison to the double occupancy d, the contact C is more essential to capture many-body effects induced by the variation of the interaction strength. Using the thermal potential $f = e - \mu n_c - 2Bm - Ts - uC$ and the Maxwell relations in its derivatives with respect to the temperature, chemical potential and magnetic fields, we may build up general relations between contact susceptibilities and interaction-driven variations of density, magnetization and entropy:

$$\frac{\partial n_c}{\partial u} = -\frac{\partial C}{\partial \mu}, \tag{141}$$

$$\frac{\partial m}{\partial u} = -\frac{\partial C}{\partial (2B)}, \tag{142}$$

$$\frac{\partial s}{\partial u} = -\frac{\partial C}{\partial T}. \tag{143}$$

We prove that these contact susceptibilities will provide striking features of interaction effects in the thermodynamics of the model. In particular, the relations (141) and (142) respectively provide important input on the interaction-driven quantum mechanism and equation (143) for quantum cooling, to be discussed in more detail later.

Building on the contact susceptibilities' relations, equations (141)–(143), we further show that the contact susceptibilities exhibit universal scaling behaviour in the quantum critical region [141]. The Mott insulator phase with an average of one electron occupying one site is of particular interest in many-body physics. Here, using the free energy, equation (103), for the transition from IV to V, we obtain the contact susceptibilities

$$C = -1 - \frac{4}{3}f_{11}A^3 - 4\lambda_1\eta_1 A^2\frac{\partial A}{\partial u} - \frac{2}{15}f_{21}A^5 - \frac{2}{3}\lambda_2\eta_1 A^4\frac{\partial A}{\partial u} + \frac{T^{\frac{1}{2}}b_0 b_1}{2\pi^{\frac{1}{2}}}f_{\frac{1}{2}}, \tag{144}$$

$$\frac{\partial C}{\partial \mu} = -\frac{b_0 b_1}{2\pi^{\frac{1}{2}}T^{\frac{1}{2}}}f_{-\frac{1}{2}}, \tag{145}$$

$$\frac{\partial C}{\partial (2B)} = \frac{\partial C_0}{\partial 2B} - \frac{b_0 b_1}{4\pi^{\frac{1}{2}}T^{\frac{1}{2}}}\left(1 - \frac{4A_c}{\pi u + A_c}\right)f_{-\frac{1}{2}}, \tag{146}$$

$$\frac{\partial C}{\partial T} = \frac{b_0 b_1}{4\pi^{\frac{1}{2}}T^{\frac{1}{2}}}f_{\frac{1}{2}} + \frac{b_0 b_1}{2\pi^{\frac{1}{2}}T^{\frac{3}{2}}}\left[\Delta\mu + \left(1 - \frac{4A_c}{\pi u + A_c}\right)\Delta B\right]f_{-\frac{1}{2}}, \tag{147}$$

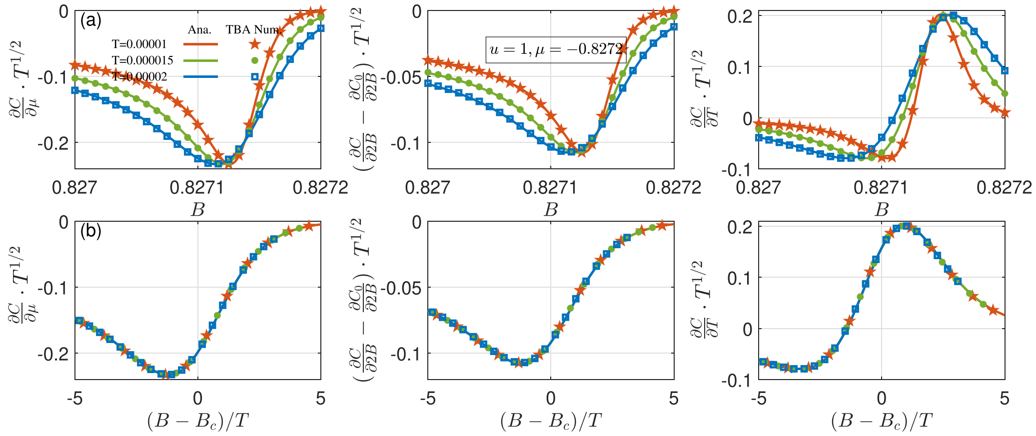

Figure 17. The universal scaling behaviour of susceptibilities: (a) contact susceptibilities with respect to the chemical potential, magnetic field and temperature vs the magnetic field at the quantum criticality of phase transition IV–V. (b) Contact susceptibilities vs the argument $(B - B_c)/T$ show universal scaling forms at quantum criticality. The parameters are set within the white empty circle in figure 1. The numerical results obtained from the TBA equations (symbols) confirm the scaling functions of the contact susceptibilities, equations (144)–(147) (solid lines).

where C_0 denotes the background terms of the ground state, that is equation (140). We have denoted the background of the magnetic susceptibility and other functions as

$$\begin{aligned}\frac{\partial C_0}{\partial 2B} = &-4A^2\left(f_{11} + \frac{1}{6}f_{21}A^2\right)\frac{\partial A}{\partial(2B)} \\ &- 8\eta_1 A\left(\lambda_1 + \frac{1}{3}\lambda_2 A^2\right)\frac{\partial A}{\partial(2B)}\frac{\partial A}{\partial u}, \\ &- 4\eta_1 A^2\left(\lambda_1 + \frac{1}{6}\lambda_2 A^2\right)\frac{\partial^2 A}{\partial(2B)\partial u},\end{aligned} \tag{148}$$

$$f_{11} = \frac{\partial}{\partial u}(\lambda_1\eta_1), f_{21} = \frac{\partial}{\partial u}(\lambda_2\eta_1), \ \frac{\partial A}{\partial B} = -\frac{1}{\eta_1 A\left(1 + \frac{A}{\pi u}\right)}, \tag{149}$$

$$b_1 = \frac{\partial(2 + C_2)}{\partial u} = -2 - \frac{8}{\pi u(1+u^2)^{\frac{3}{2}}}A^2\frac{\partial A}{\partial u}. \tag{150}$$

Solving (84) in the supplementary material[7], we have the following explicit forms of the quantities

$$\begin{aligned}\frac{\partial A}{\partial u} = &\left(1+u^2\right)\frac{u - \left(1+u^2\right)^{\frac{1}{2}}}{A\left(1 + \frac{A}{\pi u}\right)} \\ &+ \frac{3u}{2(1+u^2)}\frac{A\left[1 + \frac{2}{9\pi u}\left(4 + \frac{1}{u^2}\right)A\right]}{1 + \frac{A}{\pi u}},\end{aligned} \tag{151}$$

$$\frac{\partial^2 A}{\partial B\partial u} = \frac{1 + \frac{2A}{\pi u}}{\eta_1 A^2\left(1 + \frac{A}{\pi u}\right)^2}\frac{\partial A}{\partial u} - \frac{1}{\eta_1 \pi u^2\left(1 + \frac{A}{\pi u}\right)^2}. \tag{152}$$

In figure 17, we demonstrate the scaling behaviour of contact susceptibilities, confirming the analytic expressions (144)–(147) (solid lines) with the numerical data from TBA (symbols).

3.3.3. *Interaction-driven quantum cooling.*

It is remarkable to observe that equation (143) essentially relates the entropy, temperature and interaction strength. This relation is of great importance for interaction-driven quantum cooling since the interaction can be tuned in cold atom experiments via Feshbach resonance, and temperature plays a vital role in controlling the entropy. Therefore, an adiabatic cycle process can be used in realization of quantum refrigeration in real physical systems. Inspired by this, here we consider an isentropic process by ramping the interaction strength up or down. Focusing on the (T, u) coordinates for a fixed magnetic field, we perform total derivatives on the entropy s, i.e.

$$\mathrm{d}s = \frac{\partial s}{\partial u}\mathrm{d}u + \frac{\partial s}{\partial T}\mathrm{d}T = 0. \tag{153}$$

Using equation (143) and the relation $\partial s/\partial T = C_v/T$, the points on the isentropic line in the (u, T) coordinates satisfy the relation:

$$\frac{C_v}{T}\frac{\partial T}{\partial u} = \frac{\partial C}{\partial T}. \tag{154}$$

Thus, the interaction-driven Grüneisen ratio Γ_{int} is related to $\partial C/\partial T$ via the relation $\Gamma_{\text{int}} = \partial C/\partial T \cdot u/C_v$. Note that $\partial C/\partial T$ dramatically changes near quantum phase transition (see equation (147) and figure 17), where C_v has a minimum (see figure 14) and the entropy has a maximum (see figure 18). A good cooling effect is observed when the interaction drives the system approaching a critical point. The lowest temperature point can be estimated by $\partial C/\partial T = 0$. To characterize the refrigeration efficiency, we give a brief description of the lowest reachable temperature during an adiabatic cooling cycle. From the results, equation (147), of $\partial C/\partial T$, the condition for determining the lowest temperature reads

$$\frac{1}{2}\mathrm{Li}_{\frac{1}{2}}\left(-\mathrm{e}^{x}\right) - x\mathrm{Li}_{-\frac{1}{2}}\left(-\mathrm{e}^{x}\right) = 0, \tag{155}$$

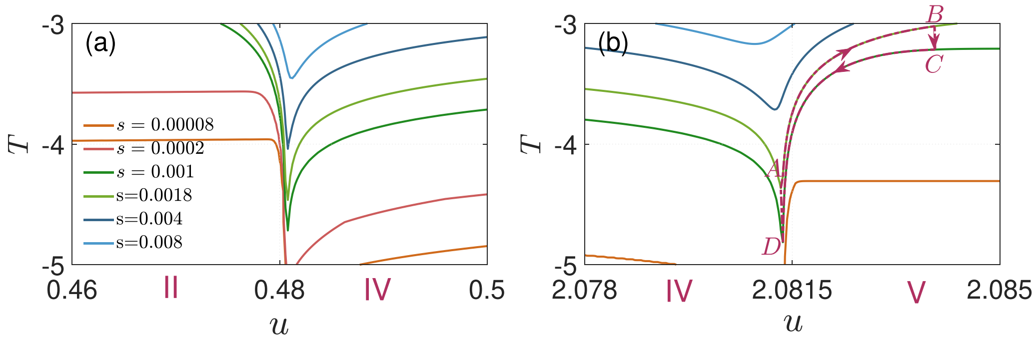

Figure 18. Plots of isentropic lines in the $T-u$ plane for the interaction-driven phase transitions II–IV (a) and IV–V (b) at $B = 0.15$ and $\mu = -2.5$, which is initially located in phase II, then enters phase IV, finally reaching phase V as the interaction increases. The temperature on the vertical axis is logarithmic. The purple dotted lines in (b) denote the interaction-driven Otto cycle, where stages A and B (or stages C and D) lie on the isentropic lines; see the main text.

where $x = \alpha_u \Delta u/T$. It is found that, to a good approximation, $x \approx 1.3117$. Thus, the extreme point can be determined. In figure 18, we plot the isentropic lines near the phase boundaries of II–IV (a) and IV–V (b), respectively. It is obvious that entropy shows a minimum in the quantum critical regions. Away from the QCP with temperature $T \ll |u-u_c|$, the entropy linearly depends on temperature; see the left part of figure 18(a) and the right part of figure 18(b). In figure 18(b), we draw an Otto cycle for the interaction-driven refrigeration process. Stages A and D lie around the QCP, whereas stages B and C are located in the TLL area. There are four steps to cool the target material. For A $\to$ B, the working substance is adiabatically ramped up from the target temperature T_{target} to the nonthermal higher temperature stage B. Then, through a hot isochore process B $\to$ C, the working substance comes into contact with the ambient conditions, transferring heat to the high-temperature source. Meanwhile, the temperature of the working substance reduces to the one at the thermal state C. Next, for the isentrope process C $\to$ D, the working substance is adiabatically ramped down to the low-temperature stage D. This is an opposite process in contrast to the A $\to$ B process. Finally, for the isochore process D $\to$ A, the working substance contacts with the target object, absorbing heat from the target material and reaching the thermal state A. Consequently, the target object is cooled down by this cycle.

Now let us determine the lowest temperature which can be reached through an isentropic process indicated in figure 18. From equations (114)–(118), phase II (V) contains one charge (spin) degrees of freedom. Consequently, their entropies $s_{\text{L}1}$ and $s_{\text{L}2}$ are given by equations (34) and (35), respectively, namely,

$$s_{\text{L}1} \approx \frac{\pi T_{\text{L}1}}{3 v_c}, \tag{156}$$

$$s_{\text{L}2} \approx \frac{\pi T_{\text{L}2}}{3 v_s}. \tag{157}$$

Comparing isentropic lines with the same entropy for phases II, IV and V, for example, $s = 0.00008$ in figure 18, the temperature of TLL$_C$ (phase II) is higher than that of TLL$_S$ (phase V) since the charge velocity v_c changes faster than the spin velocity v_s when the interaction is changed around the critical point, i.e.

$$T_{\text{L}1} > T_{\text{L}2}. \tag{158}$$

On the other hand, when it approaches the QCP, i.e. at the extreme low temperature for each isentropic line, the entropy has explicit expressions for the transitions II–IV and IV–V

$$s_{s1} \approx \lambda_3 \pi^{1/2} \sigma_1(0) \left(\varepsilon_1''(0)/2\right)^{-1/2} T_{c1}^{1/2}, \tag{159}$$

$$s_{s2} \approx \lambda_3 \pi^{1/2} \rho(\pi) \left(-\kappa''(\pi)/2\right)^{-1/2} T_{c2}^{1/2}, \tag{160}$$

respectively, where $\lambda_3 = x\text{Li}_{1/2}(-\text{e}^x) - 3/2\text{Li}_{3/2}(-\text{e}^x) \approx 1.3467$.

With the above analysis, we observe that the entropy shows a square root dependence on the temperature at an extreme point; it is proportional to the temperature in the Luttinger liquid. Therefore, by considering an isentropic cooling process through the ramping up or down in the $T-u$ plane around critical phase transitions from II to IV or from V to IV, see figure 18, the minimum temperatures can be reached

$$\text{II–IV: } \frac{T_{c1}^{1/2}}{T_{L1}} = \frac{\pi^{1/2}\left(\varepsilon_1''(0)/2\right)^{1/2}}{3\lambda_3 v_c \sigma_1(0)}, \tag{161}$$

$$\text{V–IV: } \frac{T_{c2}^{1/2}}{T_{L2}} = \frac{\pi^{1/2}\left(-\kappa''(\pi)/2\right)^{1/2}}{3\lambda_3 v_s \rho(\pi)}, \tag{162}$$

respectively. A brief discussion about interaction-driven quantum cooling is given in [109]. Based on previous results, equations (43) and (48), the leading contributions to the minimum temperature near the quadruple critical point are

$$\text{II–IV: } \frac{T_{c1}^{1/2}}{T_{L1}} \approx \frac{\pi^{1/2}\eta_1^{1/2}}{6\lambda_1\lambda_3\delta}, \tag{163}$$

$$\text{V–IV: } \frac{T_{c2}^{1/2}}{T_{L2}} \approx \frac{2\lambda_1\pi^{5/2}}{3\lambda_3\eta_1 A}. \tag{164}$$

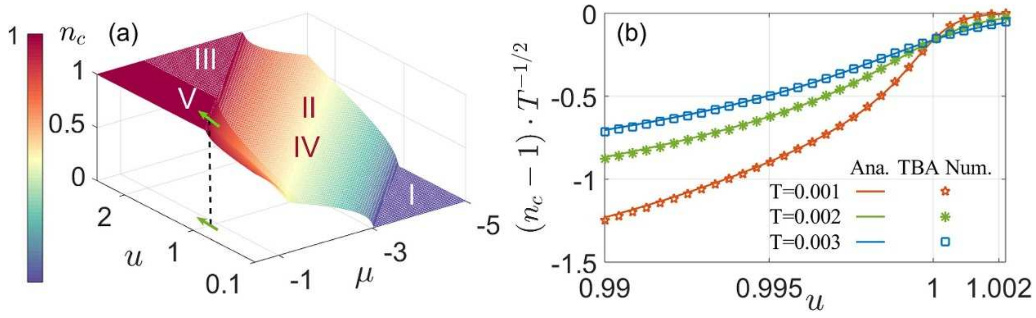

Figure 19. (a) A 3D plot of the density n_c in the $u-\mu-n_c$ coordinate with fixed $B = 0.827\,14$, showing quantum phases I, IV (or II) and V (or III). The green arrow on the 3D coordinate denotes the phase transition from IV to V around $u_c = 1$. And the green arrow in the $u-\mu$ plane represents a 3D projection onto the $u-\mu$ plane when the density firstly reaches unity from phase IV to V. (b) Quantum scaling behaviour of density near phase transition from IV to V driven by interaction. The numerical results from the TBA equations and analytical results are in good agreement.

These suggest that the lowest temperature can be reached around the QCPs, which can also be reachable through adiabatic demagnetization cooling, see the study of the Grüneisen parameters in [120]. Moreover, we further note that the location of the minimum temperature for each contour entropy line in the T-u plane is governed by the relation $\alpha_u \Delta u/T \approx 1.3117$ in equation (155), where α_u needs to be determined.

3.3.4. Calculation of α_u for phase transition IV–V. One remaining problem from the discussion in the previous subsection is that the underlying coefficient α_u is not given. It not only determines the scaling factor of the critical temperature at quantum criticality driven by the interaction, but also determines the extreme point associated with the lowest temperature in an isotropic process in the refrigeration cycle. We know that α_u emerging in a polylog function is related to the phase transition line via the formula $\kappa(\pi) = \alpha_B \Delta B + \alpha_\mu \Delta\mu + \alpha_u \Delta u$. For transition IV–V, the phase boundary between phase IV and V is marked by $\kappa(\pi) = 0$, where $\kappa(\pi)$ is expressed via $\varepsilon_1(\Lambda)$ by

$$\kappa(\pi) = 2 - \mu - 2u - B + \int_{-A}^{A} \mathrm{d}\Lambda a_1(\Lambda)\varepsilon_1(\Lambda), \tag{165}$$

$$\begin{aligned}\varepsilon_1(\Lambda) &= 2B - 4\mathrm{Re}\sqrt{1-(\Lambda - \mathrm{i}u)^2} + 4u \\ &\quad - \int_{-A}^{A} \mathrm{d}\Lambda' a_2(\Lambda - \Lambda')\varepsilon_1(\Lambda').\end{aligned} \tag{166}$$

However, for transition IV–V, the corresponding equations (165) and (166) are not in polynomial forms in terms of the interaction u. In this section, we present a numerical scheme with equation (141) based on the fact that phase transition from IV to V occurs due to the emergence of the Mott insulator with constant density. In addition to the magnetic field B and chemical potential μ that can drive the phase transition, the interaction drives the system from one phase to others. In figure 19(a), we plot the phase diagram in the $(u-\mu-n_c)$ coordinate at a fixed magnetic field $B = 0.827\,14$. The vacuum phase I has $n_c = 0$. The density is $0 < n_c < 1$ for phases II or IV, and $n_c = 1$ for phases III or V. The boundary line for IV and V (or II and III) is marked with a constant density $n_c = 1$. On this transition line, we perform total derivatives of n_c, yielding

$$\mathrm{d}n_c = \frac{\partial n_c}{\partial u}\mathrm{d}u + \frac{\partial n_c}{\partial \mu}\mathrm{d}\mu = 0. \tag{167}$$

Substituting equation (141) for $\partial n_c/\partial u = -\partial C/\partial\mu$ with equation (145) and substituting$\partial n_c/\partial\mu = \chi_c$ with equation (106) into (167), near the boundary line $n_c = 1$ in the $u-\mu$ plane, we have

$$\alpha_u = -\alpha_\mu \frac{\partial\mu}{\partial u} \tag{168}$$

where we note that $\alpha_u = \frac{\partial(2+C_2)}{\partial u}$; $-1 = \alpha_\mu$; see equation (150). Near the phase transition IV to V, we see $\alpha_\mu = -1$ since the chemical potential μ only appears in the charge leading term, with no contribution to the driving terms in spin string; see equations (165) and (166). At this point, we relate the value of α_u to the slope at the QCP in the $u_c - \mu_c$ plane. Therefore, equation (168) provides us with a way to obtain the unknown coefficient α_u. Moreover, $\partial\mu/\partial u$ can also be obtained directly from equations (165) and (166)

$$2\frac{\partial\mu}{\partial u} = -2 + \int_{-A}^{A} \mathrm{d}\Lambda \left[\frac{\partial a_1(\Lambda)}{\partial u}\varepsilon_1(\Lambda) + a_1(\Lambda)\frac{\partial\varepsilon_1(\Lambda)}{\partial u}\right], \tag{169}$$

$$\begin{aligned}\frac{\partial\varepsilon_1(\Lambda)}{\partial u} &= -4\frac{\partial}{\partial u}\left[\mathrm{Re}\sqrt{1-(\Lambda-\mathrm{i}u)^2} - u\right] \\ &\quad - \int_{-A}^{A} \mathrm{d}\Lambda' \frac{\partial}{\partial u}\left[a_2(\Lambda - \Lambda')\varepsilon_1(\Lambda')\right].\end{aligned} \tag{170}$$

Then, $\partial\mu/\partial u$ can be obtained by iteratively solving the above two equations. Here, we use a colour map to get α_u instead, which can apply to arbitrary systems without knowing explicit analytic formulas. In figure 19(a), we plot the density in terms of (u_c, μ_c), showing quantum phase transitions. To evaluate $\alpha_u(u_c, \mu_c)$ numerically for the interaction-driven phase transitions, compared to figures 14(c) and (d) driven by external fields, we choose two adjacent points $(u_1, \mu_1), (u_2, \mu_2)$ near the

QCP $u_c = 1$. It is evaluated from equation (168) that $\alpha_u(u_c = 1) \approx (\mu_1 - \mu_2)/(u_1 - u_2) \approx -1.9627$. Using this value as the argument factor of the scaling function for the phase transition IV–V with the help of the scaling functions, equations (103) and (118), we plot the density scaling law in figure 19(b) in terms of the variation of interaction strength. This shows an excellent agreement between the numerical calculation and these analytical scaling functions, equations (103), (118) and (168). One can see that the obtained α_u captures the thermodynamic scaling law well.

3.3.5. Calculation of α_u for phase transition II–IV. Similar to the analysis of the parameter α_u for the transition of IV to V, the relevant coefficients $\alpha_B, \alpha_\mu, \alpha_u$ for transition II to IV are related to each other. In contrast to the Mott-insulator transition, this transition arises from the introduction of spin-down electrons, i.e. the phase transition points are determined by zero spin-down particle density $n_\downarrow = 0$. Considering a magnetic field B and coupling strength u-driven phase transition, we perform the total derivative of $n_\downarrow$, i.e.

$$\mathrm{d}n_\downarrow = \frac{\partial n_\downarrow}{\partial u}\mathrm{d}u + \frac{\partial n_\downarrow}{\partial (2B)}\mathrm{d}(2B) = 0. \tag{171}$$

Substituting $\partial m/\partial B = \chi_s$ with equation (94) and inserting equation (142) into equation (171), with the help of $n_\downarrow = n_c/2 - m$ we obtain

$$\alpha_u = -\alpha_B \frac{\partial B}{\partial u}. \tag{172}$$

Recall that equation (123) gives us the value of $\alpha_B = -2\left[1 - \arctan\left(\sin Q_c/u\right)/\pi\right]$. We also note that the quantity $\partial B/\partial u$ can be obtained from equation (121), namely, near the critical line, we have the following relation

$$B = \frac{2u}{\pi}\int_0^Q \mathrm{d}k \frac{\cos k}{u^2 + \sin^2 k}\left(\cos k - \cos Q\right). \tag{173}$$

Therefore, $\partial B/\partial u$ is easily obtained through the derivative on both sides of this equation with respect to u. From equation (172), we finally get the following analytic expression

$$\alpha_u = \frac{4}{\pi}\left[\int_0^{Q_c} \mathrm{d}k \frac{\cos^2 k}{u_c^2 + \sin^2 k} - 2u_c^2 \int_0^{Q_c} \mathrm{d}k \frac{\cos^2 k}{\left(u_c^2 + \sin^2 k\right)^2} + \arctan\left(\frac{\sin Q_c}{u_c}\right) + \frac{\sin\left(2Q_c\right)}{2\left(u_c^2 + \sin Q_c^2\right)}\right]. \tag{174}$$

In summary, simple relations exist between any pair of these scaling factors α_B, α_μ and α_u. In the previous two subsections, via the contact susceptibility expressions (141) and (142), we build up relationships between α_u and α_μ as well as between α_u and α_B; see equations (168) and (172). In fact, in terms of thermodynamic potential, Maxwell relations can also build a connection between the charge susceptibility $\partial n_c/\partial(2B)$ and magnetization susceptibility $\partial m/\partial \mu$. Moreover, equations (168) and (172) remain valid for other transitions, like I–II, II–III and III–V. Based on this feature, we can conclude that the following relations

$$\frac{\alpha_u}{\alpha_\mu} = -\frac{\partial \mu}{\partial u}, \tag{175}$$

$$\frac{\alpha_u}{\alpha_B} = -\frac{\partial B}{\partial u}, \tag{176}$$

$$\frac{\alpha_B}{\alpha_\mu} = -\frac{\partial \mu}{\partial B} \tag{177}$$

hold true in general, i.e. for arbitrary interaction strength and density. In the above, we have discussed the exact values of α_B for the phase transition II–IV and α_μ for the phase transition IV–V. The remaining coefficients can be derived through equations (175), (176) and (177) in a straightforward way. Here, we give the values of α_μ for II–IV and α_B for IV–V

$$\text{II–IV: } \alpha_\mu = \frac{2}{\pi}\arctan\left(\frac{\sin Q_c}{u}\right), \tag{178}$$

$$\text{IV–V: } \alpha_B = -\frac{1}{2} + \int_0^A \mathrm{d}\Lambda a_1\left(\Lambda\right)\frac{\partial \varepsilon_1\left(\Lambda\right)}{\partial B}. \tag{179}$$

Together with equations (114)–(118), the results obtained here offer a more general description of quantum criticality in terms of full internal and external potentials in the 1D Hubbard model in arbitrary experimentally controllable parameters. These hold true for the second-order phase transition in higher-dimensional quantum systems too.

4. Conclusion and remarks

We have presented analytical results of the thermal and magnetic properties of the 1D Hubbard model, ranging from elementary spin and charge excitations, to the SILL, universal thermodynamics, quantum criticality and interaction-driven refrigeration. A summary of our new results is as follows:

(1) We have presented exact results of various excitations and multiple particle excitations, which are created by few elementary excitations involving fractional spin and charge excitations, showing the origin of the spin and charge separation and spin-incoherent liquid. Meanwhile, the gapped charge $k - \Lambda$ strings and spinon bound-state excitations, as well as some combinations of them, have been given in the supplementary material[7]. These are complementary to that studied in [22].

(2) Based on the study of such excitations, together with the dimensionless Wilson ratio, and universal scaling of the thermodynamics of the model, we have a rigorous investigation of the SILL, which was previously studied only within the framework of effective theory via bosonization. From the conformal field theory point of view, we have rigorously given the characteristics of various correlation functions near the phase transition from phase II to phase IV, showing the existence of a collective mode in charge degrees of freedom rather than the spin degrees of freedom. The crossover regime between the TLL and the

quantum critical region belongs to the SILL and indicates a coexistence of liquid and gas, see equation (129), giving the behaviour beyond TLL theory.

(3) We have presented general analytical results of thermodynamics, independent of the microscopic details of the model. Explicitly, we have determined the additivity rules of charge and spin susceptibilities in the grand canonical ensemble equations (52) and (53) and canonical ensemble equations (57) and (58). Away from the critical point and in the low-energy regime, in general, coherent spin and charge degrees of freedom give rise to the well-known phenomenon of spin–charge separation, indicating the nature of the TLL. Besides the thermodynamics, the quantum criticality and universal scaling laws induced by the variation of the magnetic field and chemical potential have been obtained analytically and confirmed numerically; see the general results of the criticality equations (114)–(118). These general results are obtained for the first time and are applicable to any other integrable models. In addition, we have studied the interaction-driven quantum critical behaviour, which provides a promising opportunity to study interaction-driven quantum phase transitions in ultracold atoms.

(4) We have introduced the lattice version of the contact and contact susceptibilities with respect to the external fields and temperature. In particular, we have investigated applications of contact susceptibilities that build up a general connection between interaction-driven quantum criticality and the phase transitions induced by external fields. These results, equations (175)–(177) together with equations (114)–(118), present general relations among arbitrary external- and internal-potential-driven quantum phase transitions, which allow us to address very general cases in phase transition. By virtue of the contact susceptibilities, we have discussed Mott transition, quantum refrigeration and interaction-induced quantum transitions, showing promising application in quantum cooling with ultracold atoms; see section 3.3.

In view of the rapid advances in trapping and controlling ultracold atoms in experiments, the results obtained here will provide direct guidance to experimentally explore various many-body phenomena in the 1D Hubbard model, such as quantum criticality, spin-coherent and incoherent Luttinger liquids, generalized hydrodynamics and transport properties. These relations reveal deep insights into the quantum criticality of the Hubbard model. Furthermore, applications of our method to quantum metrology and other quantum technologies are also highly desirable.

Data availability statement

All data that support the findings of this study are included within the article (and any supplementary files).

Acknowledgments

We thank the Integrable Theory Group at APM for their helpful discussions. X W G acknowledges the kind hospitalities of Rice University and Institute for Advanced Study, and Tsinghua University during his visits in 2018 and 2021, respectively.

J J L performed the analytical and numerical study of the model. X W G supervised J J L in the acquisition of the results reported in this paper. Both X W G and H P initiated this study.

J J L and X W G are supported by the NSFC key Grant No. 12134015, and the NSFC key Grant Nos. 92365202 and 12121004. X W G is also partially supported by the National Key R&D Program of China under Grant No. 2022YFA1404102 and is also partially supported by the Innovation Program for Quantum Science and Technology 2021ZD0302000. H P acknowledges support from the US NSF (PHY-2207283) and the Welch Foundation (Grant No. C-1669).

ORCID iDs

Jia-Jia Luo https://orcid.org/0000-0002-1087-7397
Han Pu https://orcid.org/0000-0002-0018-3076
Xi-Wen Guan https://orcid.org/0000-0001-6293-8529

References

[1] Pruschke T, Jarrell M and Freericks J K 1995 *Adv. Phys.* **44** 187–210
[2] Dagotto E 2005 *Science* **309** 257–62
[3] Yanase Y, Jujo T, Nomura T, Ikeda H, Hotta T and Yamada K 2003 *Phys. Rep.* **387** 1–149
[4] Miyake K 2007 *J. Phys.: Condens. Matter* **19** 125201
[5] Mott N F 1968 *Rev. Mod. Phys.* **40** 677
[6] Schulz H J 1990 *Phys. Rev. Lett.* **64** 2831
[7] Stafford C A and Millis A J 1993 *Phys. Rev.* B **48** 1409
[8] Jördens R, Strohmaier N, Günter K, Moritz H and Esslinger T 2008 *Nature* **455** 204–7
[9] Kokalj J and McKenzie R H 2013 *Phys. Rev. Lett.* **110** 206402
[10] Ramirez A P 1997 *J. Phys.: Condens. Matter* **9** 8171
[11] Hart R A, Duarte P M, Yang T-L, Liu X, Paiva T, Khatami E, Scalettar R T, Trivedi N, Huse D A and Hulet R G 2015 *Nature* **519** 211–4
[12] Chiu C S, Ji G, Mazurenko A, Greif D and Greiner M 2018 *Phys. Rev. Lett.* **120** 243201
[13] Giamarchi T 2017 *Nature* **545** 414–5
[14] Boll M, Hilker T A, Salomon G, Omran A, Nespolo J, Pollet L, Bloch I and Gross C 2016 *Science* **353** 1257–60
[15] Parsons M F, Mazurenko A, Chiu C S, Ji G, Greif D and Greiner M 2016 *Science* **353** 1253–6
[16] Cheuk L W, Nichols M A, Lawrence K R, Okan M, Zhang H, Khatami E, Trivedi N, Paiva T, Rigol M and Zwierlein M W 2016 *Science* **353** 1260–4
[17] Schneider U *et al* 2012 *Nat. Phys.* **8** 213–18
[18] Salomon G, Koepsell J, Vijayan J, Hilker T A, Nespolo J, Pollet L, Bloch I and Gross C 2019 *Nature* **565** 56–60

[19] Mitra D, Brown P T, Guardado-Sanchez E, Kondov S S, Devakul T, Huse D A, Schauß P and Bakr W S 2018 *Nat. Phys.* **14** 173–7
[20] Lieb E H and Wu F Y 1968 *Phys. Rev. Lett.* **20** 1445
[21] Takahashi M 1972 *Prog. Theor. Phys.* **47** 69–82
[22] Essler F H L, Frahm H, Göhmann F, Klümper A and Korepin V E 2005 *The One-Dimensional Hubbard Model* (Cambridge University Press)
[23] Koepsell J, Vijayan J, Sompet P, Grusdt F, Hilker T A, Demler E, Salomon G, Bloch I and Gross C 2019 *Nature* **572** 358–62
[24] Scherg S, Kohlert T, Sala P, Pollmann F, Madhusudhana B H, Bloch I and Aidelsburger M 2021 *Nat. Commun.* **12** 4490
[25] Gall M, Wurz N, Samland J, Chan C F and Köhl M 2021 *Nature* **589** 40–43
[26] Vijayan J, Sompet P, Salomon G, Koepsell J, Hirthe S, Bohrdt A, Grusdt F, Bloch I and Gross C 2020 *Science* **367** 186–9
[27] Hirsch J E 1985 *Phys. Rev.* B **31** 4403
[28] Jarrell M 1992 *Phys. Rev. Lett.* **69** 168
[29] Georges M and Kotliar G 1992 *Phys. Rev.* B **45** 6479
[30] Glocke S, Klümper A and Sirker J 2007 *Phys. Rev.* B **76** 155121
[31] De Leo L, Bernier J-S, Kollath C, Georges A and Scarola V W 2011 *Phys. Rev.* A **83** 023606
[32] Ibarra-García-Padilla E, Mukherjee R, Hulet R G, Hazzard K R A, Paiva T and Scalettar R T 2020 *Phys. Rev.* A **102** 033340
[33] Wietek A, Rossi R, Šimkovic I V F, Klett M, Hansmann P, Ferrero M, Stoudenmire E M Schäfer T and Georges A 2021 *Phys. Rev.* X **11** 041013
[34] Frahm H and Korepin V E 1990 *Phys. Rev.* B **42** 10553
[35] Frahm H and Korepin V E 1991 *Phys. Rev.* B **43** 5653
[36] Qin M, Schäfer T, Andergassen S, Corboz P and Gull E 2022 *Annu. Rev. Condens. Matter Phys.* **13** 275–302
[37] Kim A J Šimkovic I V F and Kozik E 2020 *Phys. Rev. Lett.* **124** 117602
[38] Ilievski E and De Nardis J 2017 *Phys. Rev.* B **96** 081118(R)
[39] Ilievski E, De Nardis J, Medenjak M and Prosen T 2018 *Phys. Rev. Lett.* **121** 230602
[40] Guardado-Sanchez E, Morningstar A, Spar B M, Brown P T, Huse D A and Bakr W S 2020 *Phys. Rev.* X **10** 011042
[41] Bertini B, Heidrich-Meisner F, Karrasch C, Prosen T, Steinigeweg R and Žnidarič M 2021 *Rev. Mod. Phys.* **93** 025003
[42] Moeckel M and Kehrein S 2008 *Phys. Rev. Lett.* **100** 175702
[43] Eckstein M, Kollar M and Werner P 2009 *Phys. Rev. Lett.* **103** 056403
[44] Schlünzen N, Joost J-P, Heidrich-Meisner F and Bonitz M 2017 *Phys. Rev.* B **95** 165139
[45] Landau L 1959 *Sov. Phys.-JETP* **8** 70
[46] Baym G and Pethick C 2008 *Landau Fermi-Liquid Theory: Concepts and Applications* (Wiley)
[47] Tomonaga S-I 1950 *Prog. Theor. Phys.* **5** 544–69
[48] Luttinger J M 1963 *J. Math. Phys.* **4** 1154–62
[49] Haldane F D M 1981 *J. Phys. C: Solid State Phys.* **14** 2585
[50] Scopa S, Calabrese P and Piroli L 2022 *Phys. Rev.* B **106** 134314
[51] Lorenz T, Hofmann M, Grüninger M, Freimuth A, Uhrig G S, Dumm M and Dressel M 2002 *Nature* **418** 614–7
[52] Demler E, Nayak C, Kee H-Y, Kim Y B and Senthil T 2002 *Phys. Rev.* B **65** 155103
[53] Kollath C, Schollwöck U and Zwerger W 2005 *Phys. Rev. Lett.* **95** 176401
[54] Jompol Y, Ford C J B, Griffiths J P, Farrer I, Jones G A C, Anderson D, Ritchie D A, Silk T W and Schofield A J 2009 *Science* **325** 597–601
[55] Schmidt T L, Imambekov A and Glazman L I 2010 *Phys. Rev.* B **82** 245104
[56] Ma Y *et al* 2017 *Nat. Commun.* **8** 14231
[57] He F, Jiang Y-Z, Lin H-Q, Hulet R G, Pu H and Guan X-W 2020 *Phys. Rev. Lett.* **125** 190401
[58] Senaratne R, Cavazos-Cavazos D, Wang S, He F, Chang Y-T, Kafle A, Pu H, Guan X-W and Hulet R G 2022 *Science* **376** 1305–8
[59] Recati A, Fedichev P O, Zwerger W and Zoller P 2003 *Phys. Rev. Lett.* **90** 020401
[60] Voit J 1993 *J. Phys.: Condens. Matter* **5** 8305
[61] Kim C, Matsuura A Y, Shen Z-X, Motoyama N, Eisaki H, Uchida S, Tohyama T and Maekawa S 1996 *Phys. Rev. Lett.* **77** 4054
[62] Auslaender O M, Steinberg H, Yacoby A, Tserkovnyak Y, Halperin B I, Baldwin K W, Pfeiffer L N and West K W 2005 *Science* **308** 88–92
[63] Kim B J *et al* 2006 *Nat. Phys.* **2** 397–401
[64] Veness T and Essler F H L 2016 *Phys. Rev.* B **93** 205101
[65] Cheianov V V and Zvonarev M B 2004 *Phys. Rev. Lett.* **92** 176401
[66] Fiete G A and Balents L 2004 *Phys. Rev. Lett.* **93** 226401
[67] Fiete G A 2007 *Rev. Mod. Phys.* **79** 801
[68] Fiete G A, Qian J, Tserkovnyak Y and Halperin B I 2005 *Phys. Rev.* B **72** 045315
[69] Fiete G A, Le Hur K and Balents L 2005 *Phys. Rev.* B **72** 125416
[70] Hew W K, Thomas K J, Pepper M, Farrer I, Anderson D, Jones G A C and Ritchie D A 2008 *Phys. Rev. Lett.* **101** 036801
[71] Meden V 1999 *Phys. Rev.* B **60** 4571
[72] Giamarchi T 2003 *Quantum Physics in One Dimension* (Oxford University Press)
[73] Miranda E 2003 *Braz. J. Phys.* **33** 3–35
[74] Cavazos-Cavazos D, Senaratne R, Kafle A and Hulet R G 2023 *Nat. Commun.* **14** 3154
[75] Giamarchi T 1991 *Phys. Rev.* B **44** 2905
[76] Hubbard J 1963 *Proc. R. Soc.* A **276** 238–57
[77] Brinkman W F and Rice T M 1970 *Phys. Rev.* B **2** 4302
[78] Han X J, Liu Y, Liu Z Y, Li X, Chen J, Liao H J, Xie Z Y, Normand B and Xiang T 2016 *New J. Phys.* **18** 103004
[79] Luther A and Emery V J 1974 *Phys. Rev. Lett.* **33** 589
[80] Voit J 1998 *Eur. Phys. J.* B **5** 505–19
[81] Orgad D 2001 *Phil. Mag.* B **81** 377–98
[82] Sciolla B, Tokuno A, Uchino S, Barmettler P, Giamarchi T and Kollath C 2013 *Phys. Rev.* A **88** 063629
[83] Paiva T, Scalettar R, Randeria M and Trivedi N 2010 *Phys. Rev. Lett.* **104** 066406
[84] Gorelik E V, Rost D, Paiva T, Scalettar R, Klümper A and Blümer N 2012 *Phys. Rev.* A **85** 061602(R)
[85] Werner F, Parcollet O, Georges A and Hassan S R 2005 *Phys. Rev. Lett.* **95** 056401
[86] Daré A-M, Raymond L, Albinet G and Tremblay A-M S 2007 *Phys. Rev.* B **76** 064402
[87] Deguchi T, Essler F H L, Göhmann F, Klümper A, Korepin V E and Kusakabe K 2000 *Phys. Rep.* **331** 197–281
[88] Yang C N and Yang C P 1969 *J. Math. Phys.* **10** 1115
[89] Klümper A and Bariev R Z 1996 *Nucl. Phys.* B **458** 623–39
[90] Batchelor M T, Guan X-W, Oelkers N and Tsuboi Z 2007 *Adv. Phys.* **56** 465–543
[91] Carmelo J, Horsch P, Bares P A and Ovchinnikov A A 1991 *Phys. Rev.* B **44** 9967
[92] Essler F H L and Korepin V E 1994 *Phys. Rev. Lett.* **72** 908
[93] Feiguin A E and Heidrich-Meisner F 2007 *Phys. Rev.* B **76** 220508(R)
Lüscher A, Noack R M and Läuchli A M 2008 *Phys. Rev.* A **78** 013637
Rizzi M, Polini M, Cazalilla M A, Bakhtiari M R, Tosi M P and Fazio R 2008 *Phys. Rev.* B **77** 245105

Tezuka M and Ueda M 2008 *Phys. Rev. Lett.* **100** 110403
Tezuka M and Ueda M 2010 *New J. Phys.* **12** 055029

[94] Penc K, Mila F and Shiba H 1995 *Phys. Rev. Lett.* **75** 894

[95] Krivnov V Y and Ovchinnikov A A 1977 *Zh. Eksp. Teor. Fiz* **73** 2364–73

[96] Woynarovich F 1983 *J. Phys. C: Solid State Phys.* **16** 6593

[97] Bogoliubov N M and Korepin V E 1988 *Mod. Phys. Lett.* B **1** 349
Bogoliubov N M and Korepin V E 1990 *Theor. Math. Phys.* **82** 231–43

[98] Woynarovich F and Penc K 1991 *Z. Phys.* B **85** 269–80

[99] Essler F H L and Korepin V E 1994 *Nucl. Phys.* B **426** 505–33

[100] Sacramento P D 1995 *J. Phys.: Condens. Matter* **7** 143

[101] Cheng S, Yu Y-C, Batchelor M T and Guan X-W 2018 *Phys. Rev.* B **97** 121111(R)

[102] Cheng S, Jiang Y-Z, Yu Y-C, Batchelor M T and Guan X-W 2018 *Nucl. Phys.* B **929** 353–76

[103] Cheng S, Yu Y-C, Batchelor M T and Guan X-W 2018 *Phys. Rev.* B **97** 125145

[104] White S R, Scalapino D J, Sugar R L, Loh E Y, Gubernatis J E and Scalettar R T 1989 *Phys. Rev.* B **40** 506

[105] Caffarel M and Krauth W 1994 *Phys. Rev. Lett.* **72** 1545

[106] Wang Y, Esterlis I, Shi T, Cirac J I and Demler E 2020 *Phys. Rev. Res.* **2** 043258

[107] Timrov I, Marzari N and Cococcioni M 2021 *Phys. Rev.* B **103** 045141

[108] Sénéchal D, Perez D and Pioro-Ladrière M 2000 *Phys. Rev. Lett.* **84** 522

[109] Luo J-J, Pu H and Guan X-W 2023 *Phys. Rev.* B **107** L201103

[110] Ovchinnikov A A 1969 *Sov. Phys. JETP* **29** 4

[111] Nocera A, Patel N D, Fernandez-Baca J, Dagotto E and Alvarez G 2016 *Phys. Rev.* B **94** 205145

[112] Shiba H 1972 *Phys. Rev.* B **6** 930

[113] Schadschneider A and Zittartz J 1991 *Z. Phys.* B **82** 387

[114] Kawakami N, Usuki T and Okiji A 1989 *Phys. Lett.* A **137** 287–90

[115] Usuki T, Kawakami N and Okiji A 1990 *J. Phys. Soc. Japan* **59** 1357–65

[116] Takahashi M 1974 *Prog. Theor. Phys.* **52** 103–14

[117] Wilson K G 1975 *Rev. Mod. Phys.* **47** 773

[118] Guan X-W, Yin X-G, Foerster A, Batchelor M T, Lee C-H and Lin H-Q 2013 *Phys. Rev. Lett.* **111** 130401

[119] Yu Y-C, Chen Y-Y, Lin H-Q, Römer R A and Guan X-W 2016 *Phys. Rev.* B **94** 195129
Grüneisen E 1908 *Ann. Phys., NY* **331** 211–6

[120] Yu Y-C, Zhang S and Guan X-W 2020 *Phys. Rev. Res.* **2** 043066

[121] Luo J-J, Pu H and Guan X-W 2024 in preparation

[122] Guan X-W, Batchelor M T and Lee C 2013 *Rev. Mod. Phys.* **85** 1633

[123] Sachdev S 2011 *Quantum Phase Transitions* (Cambridge University Press)

[124] Hazzard K R A and Mueller E J 2011 *Phys. Rev.* A **84** 013604

[125] Fukui T and Kawakami N 1995 *Phys. Rev.* B **51** 5239

[126] Vitoriano C and Coutinho-Filho M D 2009 *Phys. Rev. Lett.* **102** 146404

[127] Zhang X, Chen Y Y, Liu L, Deng Y andGuan X 2022 *Natl Sci. Rev.* **9** nwac027

[128] Continentino M A 1994 *Phys. Rep.* **239** 179–213

[129] Continentino M A, Japiassu G M and Troper A 1989 *Phys. Rev.* B **39** 9734

[130] Continentino M A 2005 *Braz. J. Phys.* **35** 197

[131] Mohankumar N 2007 *Comput. Phys. Commun.* **176** 665–9

[132] Campo J V L, Capelle K, Hooley C, Quintanilla J and Scarola V W 2012 *Phys. Rev.* A **85** 033644

[133] van Loon E G C P, Rösner M, Schönhoff G, Katsnelson M I and Wehling T O 2018 *npj Quantum Mater.* **3** 32

[134] Tan S 2008 *Ann. Phys., NY* **323** 2952–70
Tan S 2008 *Ann. Phys., NY* **323** 2987–90
Tan S 2008 *Ann. Phys., NY* **323** 2971–86

[135] Zhang S and Leggett A J 2009 *Phys. Rev.* A **79** 023601

[136] Braaten E and Platter L 2009 *Laser Phys.* **19** 550–3

[137] Stewart J T, Gaebler J P, Drake T E and Jin D S 2010 *Phys. Rev. Lett.* **104** 235301

[138] Yu Z, Thywissen J H and Zhang S 2015 *Phys. Rev. Lett.* **115** 135304

[139] Yoshida S M and Ueda M 2015 *Phys. Rev. Lett.* **115** 135303

[140] Cui X 2016 *Phys. Rev.* A **94** 043636

[141] Chen Y-Y, Jiang Y-Z, Guan X-W and Zhou Q 2014 *Nat. Commun.* **5** 5140

[142] Giamarchi T 1997 *Physica* B **230** 975–80